

THE EFFECTS OF SALT DIAPYRS ON THE THERMAL MATURITY  
OF SURROUNDING SEDIMENTS IN THE  
WESTERN PYRENEES, SPAIN

by

Nicholas Martin Downs

Bachelor of Science  
Duke University  
2009

A thesis submitted in partial fulfillment of  
The requirements for the

**Master of Science in Geoscience  
Department of Geoscience  
College of Science**

**Graduate College  
University of Nevada, Las Vegas  
May 2012**



## ABSTRACT

### **The Effects of Salt Diapirs on the Thermal Maturity of Surrounding Sediments in the Western Pyrenees, Spain**

by

Nicholas Martin Downs

Salt diapirs have been modeled as having a large effect on the thermal maturity of surrounding sediments as a result of the high thermal conductivity contrast between halite and other lithologies. The goal of this study was to confirm these and other theoretical predictions through sampling of three salt structures in the western Pyrenees, Spain. Stratigraphic units around these three diapirs were targeted based on their lithologies and positions relative to the diapirs. Samples were analyzed for vitrinite reflectance and quartz cementation to determine their levels of thermal maturity. Remote sensing instruments were used to attempt to measure present day heat flow above the diapirs, and available well logs and seismic data were analyzed to determine the subsurface extent and orientation of the diapirs. Vitrinite reflectance revealed that sediments closest to the Ribera Alta and Orduna diapirs were undermature compared to regional values. The extent of the thermal anomalies around the Ribera Alta and Orduna diapirs extended to approximately 1.5 times the radii of the diapirs. Samples located above the Gernika salt weld were generally more mature than samples located below the weld, and samples closest to the root of the weld were less mature than samples further from the root. Remote sensing proved ineffective in this locality due to the high moisture content in surface vegetation.

Determining the effects of salt on the thermal maturity of surrounding sediments is important because it allows a more comprehensive understanding of source rock maturity and reservoir porosity preservation within the context of petroleum systems in basins that contain salt.

## ACKNOWLEDGEMENTS

I would like to thank Dr. Andrew Hanson for his support, guidance, and encouragement over the past two years. Additionally, I am indebted to my friends in the department, particularly LaOde Ahdyar, Yuki Agulia, Leon Taufani, Inessa Yurchenko, and Mike Giallorenzo. Finally, I'd like to credit Brittany Myers and my family for their unwavering support and love.

## TABLE OF CONTENTS

ABSTRACT.....	iii
ACKNOWLEDGEMENTS.....	v
LIST OF TABLES.....	vii
LIST OF FIGURES.....	viii
CHAPTER 1 INTRODUCTION.....	1
CHAPTER 2 HYPOTHESES AND OBJECTIVES.....	3
CHAPTER 3 GEOLOGICAL FRAMEWORK	
REGIONAL GEOLOGY.....	4
METHODOLOGICAL BACKGROUND.....	6
PREVIOUS STUDIES.....	8
CHAPTER 4 METHODOLOGY	
VITRINITE REFLECTANCE.....	14
QUARTZ CEMENTATION.....	14
SEISMIC SECTIONS AND WELL LOGS.....	15
REMOTE SENSING.....	15
CHAPTER 5 SIGNIFICANCE.....	17
CHAPTER 6 RESULTS	
DIAPIR HISTORY RECONSTRUCTION.....	18
VITRINITE REFLECTANCE.....	18
QUARTZ CEMENTATION.....	20
SEISMIC SECTIONS AND WELL LOGS.....	21
REMOTE SENSING.....	24
CHAPTER 7 DISCUSSION.....	25
CHAPTER 8 CONCLUSIONS.....	33
CURRICULUM VITAE.....	45

## LIST OF TABLES

<b>Table 1</b>	<b>Vitrinite Reflectance Data for Ribera Alta Diapir.....</b>	<b>39</b>
<b>Table 2</b>	<b>Vitrinite Reflectance Data for Orduna Diapir.....</b>	<b>41</b>
<b>Table 3</b>	<b>Vitrinite Reflectance Data for Gernika Weld.....</b>	<b>43</b>

## LIST OF FIGURES

FIGURE 1	Common thermal conductivities.....	46
FIGURE 2	Thermal conductivity and temperature.....	47
FIGURE 3	Hypotheses and locations.....	48
FIGURE 4	Field area map.....	49
FIGURE 5	Ribera Alta map.....	50
FIGURE 6	Orduna map.....	51
FIGURE 7	Gernika map.....	52
FIGURE 8	EOS Terra satellite.....	53
FIGURE 9	Modeling by Selig and Wallick (1966).....	54
FIGURE 10	Primrose salt dome, Nova Scotia.....	55
FIGURE 11	Hydrocarbon occurrence, Primrose salt dome.....	56
FIGURE 12	Modeling by O'Brien and Lerche (1984).....	57
FIGURE 13	West Bay salt dome, Louisiana.....	58
FIGURE 14	Modeling by Mello et al. (1995).....	59
FIGURE 15	Modeling of monopolar vs. dipolar anomalies.....	60
FIGURE 16	Methodology details.....	61
FIGURE 17	Remote sensing locations.....	62
FIGURE 18	Ribera Alta reconstruction.....	63
FIGURE 19	Ribera Alta reconstruction.....	64
FIGURE 20	Ribera Alta reconstruction.....	65
FIGURE 21	Ribera Alta reconstruction.....	66
FIGURE 22	Ribera Alta reconstruction.....	67
FIGURE 23	Ribera Alta reconstruction.....	68
FIGURE 24	Ribera Alta reconstruction.....	69
FIGURE 25	Ribera Alta reconstruction.....	70
FIGURE 26	Orduna reconstruction.....	71
FIGURE 27	Orduna reconstruction.....	72
FIGURE 28	Orduna reconstruction.....	73
FIGURE 29	Orduna reconstruction.....	74
FIGURE 30	Orduna reconstruction.....	75
FIGURE 31	Orduna reconstruction.....	76
FIGURE 32	Orduna reconstruction.....	77
FIGURE 33	Orduna reconstruction.....	78
FIGURE 34	Gernika reconstruction.....	79
FIGURE 35	Gernika reconstruction.....	80
FIGURE 36	Gernika reconstruction.....	81
FIGURE 37	Gernika reconstruction.....	82
FIGURE 38	Gernika reconstruction.....	83
FIGURE 39	Gernika reconstruction.....	84
FIGURE 40	Gernika reconstruction.....	85
FIGURE 41	Stratigraphy of Basque-Cantabrian basin.....	86
FIGURE 42	Vitrinite reflectance plates.....	87
FIGURE 43	Vitrinite reflectance plates.....	88
FIGURE 44	Vitrinite reflectance plates.....	89



<b>FIGURE 45</b>	<b>Vitrinite reflectance plates.....</b>	<b>90</b>
<b>FIGURE 46</b>	<b>Vitrinite reflectance plates.....</b>	<b>91</b>
<b>FIGURE 47</b>	<b>Vitrinite reflectance plates.....</b>	<b>92</b>
<b>FIGURE 48</b>	<b>Vitrinite reflectance plates.....</b>	<b>93</b>
<b>FIGURE 49</b>	<b>Vitrinite reflectance plates.....</b>	<b>94</b>
<b>FIGURE 50</b>	<b>Vitrinite reflectance plates.....</b>	<b>95</b>
<b>FIGURE 51</b>	<b>Vitrinite reflectance plates.....</b>	<b>96</b>
<b>FIGURE 52</b>	<b>Ribera Alta thin sections.....</b>	<b>97</b>
<b>FIGURE 53</b>	<b>Ribera Alta thin sections.....</b>	<b>98</b>
<b>FIGURE 54</b>	<b>Ribera Alta thin sections.....</b>	<b>99</b>
<b>FIGURE 55</b>	<b>Ribera Alta thin sections.....</b>	<b>100</b>
<b>FIGURE 56</b>	<b>Ribera Alta thin sections.....</b>	<b>101</b>
<b>FIGURE 57</b>	<b>Ribera Alta thin sections.....</b>	<b>102</b>
<b>FIGURE 58</b>	<b>Ribera Alta thin sections.....</b>	<b>103</b>
<b>FIGURE 59</b>	<b>Ribera Alta thin sections.....</b>	<b>104</b>
<b>FIGURE 60</b>	<b>Aulesti-1 geothermal gradient.....</b>	<b>105</b>
<b>FIGURE 61</b>	<b>Seismic block overview.....</b>	<b>106</b>
<b>FIGURE 62</b>	<b>Seismic line ZU1.....</b>	<b>107</b>
<b>FIGURE 63</b>	<b>Seismic line ZU2.....</b>	<b>108</b>
<b>FIGURE 64</b>	<b>Seismic line ZU4.....</b>	<b>109</b>
<b>FIGURE 65</b>	<b>Seismic line ZU5.....</b>	<b>110</b>
<b>FIGURE 66</b>	<b>Ribera Alta remote sensing data.....</b>	<b>111</b>
<b>FIGURE 67</b>	<b>Orduna vitrinite reflectance data.....</b>	<b>112</b>
<b>FIGURE 68</b>	<b>Orduna vitrinite reflectance data.....</b>	<b>113</b>
<b>FIGURE 69</b>	<b>Ribera Alta vitrinite reflectance data.....</b>	<b>114</b>
<b>FIGURE 70</b>	<b>Ribera Alta vitrinite reflectance data.....</b>	<b>115</b>
<b>FIGURE 71</b>	<b>Orduna maturity vs. distance.....</b>	<b>116</b>
<b>FIGURE 72</b>	<b>Ribera Alta maturity vs. distance.....</b>	<b>117</b>
<b>FIGURE 73</b>	<b>Monopolar thermal anomaly model.....</b>	<b>118</b>
<b>FIGURE 74</b>	<b>Dipolar thermal anomaly model.....</b>	<b>119</b>
<b>FIGURE 75</b>	<b>Monopolar vs. dipolar models.....</b>	<b>120</b>
<b>FIGURE 76</b>	<b>Orduna thermal anomaly extent.....</b>	<b>121</b>
<b>FIGURE 77</b>	<b>Ribera Alta thermal anomaly extent.....</b>	<b>122</b>
<b>FIGURE 78</b>	<b>Gernika vitrinite reflectance data.....</b>	<b>123</b>
<b>FIGURE 79</b>	<b>Gernika cross section data.....</b>	<b>124</b>
<b>FIGURE 80</b>	<b>Gernika maturity vs. distance.....</b>	<b>125</b>
<b>FIGURE 81</b>	<b>Gernika subsalt/suprasalt contours.....</b>	<b>126</b>
<b>FIGURE 82</b>	<b>Remote sensing diapir/nondiapir data.....</b>	<b>127</b>
<b>FIGURE 83</b>	<b>El Gordo remote sensing locations.....</b>	<b>128</b>
<b>FIGURE 84</b>	<b>El Gordo diapir/nondiapir data.....</b>	<b>129</b>
<b>FIGURE 85</b>	<b>Summary of hypotheses and conclusions.....</b>	<b>130</b>

# CHAPTER 1

## Introduction

Spanish salt has a long, colorful history. Plinius (23-79BC) described the Montana de Sal in Spain, and prehistoric tools suggest that mining operations near salt exposures have existed for tens of thousands of years (Rios, 1968). Pure, white halite slabs have been used as a form of currency in some parts of the world and are still in use in sub-Saharan Africa (Benanav, 2006).

Salt diapirs began attracting serious scientific attention in the early part of the 20th century, mainly as a result of their relevance to the petroleum industry. It has been well known for the better part of a century that thermal anomalies are present above, around, and below salt diapirs (Selig and Wallick, 1966). Multiple researchers have presented models that predicted changes in isotherms around these structures, with general agreement between the varying models. Generally, elevated heat flux was modeled above and along the upper flanks of buried diapirs, and depressed heat flux was modeled along the lower flanks and below both buried and exposed diapirs. An accurate understanding of these changes is of primary importance for oil and gas exploration, specifically with regards to how altered geothermal gradients may advance or suppress the maturation of petroleum source rocks. Given the fact that the maturation of organic matter is governed by chemical reactions, even a relatively small change of 10°C will double or halve the rate of source rock maturation (Waples, 1980).

There are two primary factors that impact the configuration and magnitude of these thermal anomalies: (1) specific characteristics of the diapir, including shape, composition, volume, and depth; and (2) the thermal conductivity contrast between salt and surrounding sediments (Mello et al., 1995; Jensen, 1983). As documented by Robertson (1988), the thermal conductivity of most clastic sediments ranges between 1.0 and 4.0 W/m°C and is dependent upon porosity and lithology (Figs. 1, 2). As a result of this porosity dependence, the thermal conductivity of clastic rocks changes with depth beneath the surface. The thermal conductivity of halite ranges between 5.0 and 8.0 W/m°C, and increases with increasing pressure but decreases with increasing temperature.

As a result of the contrast in the thermal conductivity of halite and clastic rocks, isotherms above, around, and below salt diapirs can be highly anomalous with respect to regional trends (Corrigan and Sweat, 1995). In contrast to the multiple models that have been published, there has been limited field-based investigation into this topic. The majority of models have relied on data produced from a single diapir or on a limited number of down-bore temperature measurements from wells near diapirs.

## CHAPTER 2

### Hypotheses and Objectives

The goal of this study was to test multiple hypotheses related to thermal anomalies around salt diapirs (Fig. 3):

(1) That the thermal maturity of sediments will increase as lateral distance from a diapir decreases.

(2) That thermal anomalies of small diameter diapirs will be more localized than those associated with larger diameter diapirs.

(3) That sediments above an inclined diapir or weld (suprasalt) will be more mature than sediments below an inclined diapir or weld (subsalt).

(4) That remote sensing instruments can be used to measure the present-day heat flow differences between a diapir and surrounding sediments.

(5) That quartz cementation will increase as lateral distance from a diapir decreases.

## CHAPTER 3

### Geological Framework

#### Regional Geology

The study area is located in the Basque Cantabrian region, northern Spain (Fig. 4). The Keuper evaporites that form diapirs in this region were deposited in the late Triassic (210Ma) as a result of rifting between Iberia and Europe (Canerot et al., 2005). In Spain the Keuper evaporites consist of saline and gypsiferous variegated marls, as well as ophitic rocks, bipyramidal quartz, and aragonite prisms. Gypsum mixed with marl is the most commonly found surface outcrop of Keuper evaporites; halite is rarely encountered. Keuper evaporite outcrops are highly disordered, with deformation commonly obscuring the original thickness of beds. In many of the Alpine ranges of Spain, Keuper evaporites played an important role, with Mesozoic-Cenozoic blocks gliding over the evaporites and being intensely folded (Rios, 1968).

For much of the Mesozoic (250-65Ma), the Pyrenean orogen was a transform plate boundary, with transtensional and transpressional regimes alternating with minor changes in plate vectors (Canerot et al., 2005). During the latest Jurassic to early Cretaceous (150-120Ma), reactivated basement faults created the Neocimmerian event, which resulted in the creation of WNW-ESE trending salt-cored anticlines. Although the Neocimmerian event has traditionally been considered an extensional event (with the opening of the North Atlantic), Canerot et al. (2005) proposed it to be a compressional event. They cite

widespread uplift, physical modeling, and the lack of reactive diapirism in salt cored anticlines as evidence for compression.

During the Aptian-Albian (125-100Ma), transtension resulted in the reactivation of ENE-WSW basement faults. Where these faults intersected with the preexisting Neocimmerian anticlines, reactive diapirism occurred, with most diapirs having pierced the surface by the end of the Aptian. This transtensional period was interrupted by brief episodes of compression, which resulted in uplift, rotation, and erosion of sediments surrounding the diapirs. Little salt movement occurred in the late Cretaceous (70Ma), with many diapirs exhausting their supply of salt, leading to the welding out of diapir stocks and burial of diapirs.

The Paleogene Pyrenean orogen resulted in strong deformation of diapirs, with differing styles of deformation dependent on the diapirs' location in the orogen. Diapirs located near the axial zone acted as decollement surfaces for thrust faults, but diapirs further away, such as those within the Basque-Cantabrian basin, were better preserved. During the late Oligocene (35 Ma), a combination of uplift, crestal stretching, and erosion led to erosional diapirism of the Orduna diapir and Gernika salt weld (Arostegui et al., 2006) and is responsible for the exposure of these salt structures at the surface today. From the Oligocene (35 Ma) to the Pliocene (4.4 Ma) the Ribera Alta diapir was the site of clastic sediment deposition within the Miranda-Trevino syncline. Subsequent post-Pliocene erosion has led to the current configuration of the Ribera Alta diapir (Canerot et al., 2005, Gibbons and Moreno, 2002).

The Ribera Alta diapir is elongate in shape, measuring 5.5km east to west by 3km north to south (Fig. 5) and is surrounded by Miocene age sediments. The Orduna diapir is more circular than Ribera Alta, measuring 5.2km north to south and 3.9km east to west (Fig. 6) and is surrounded by Cretaceous sediments. In cross section both of these diapirs are interpreted as being vertical to subvertical. The Gernika salt weld does not have a single large surface expression, but rather several small outcrops connected by salt or by salt welds to an inclined, buried salt stock (Fig. 7). The Gernika weld is surrounded primarily by Cretaceous age sediments. The Ribera Alta diapir has been estimated to have a height of more than 7,000m (Rios, 1968). The Orduna and Gernika diapirs probably have deeper roots, due to the significantly thicker Lower Cretaceous sections in those areas.

Today's climate is Mediterranean, with an average annual precipitation of 650mm and an average annual temperature of 11.5°C. Precipitation is torrential but infrequent, especially in the autumn (Gonzalez et al., 2007).

### **Methodological Background**

Vitrinite can be loosely defined as “woody plant material,” and vitrinite reflectance analysis is a commonly used method to derive maximum paleotemperatures of certain lithologies. The degree of reflectance of the vitrinite is an indicator of its maximum paleotemperature, with more mature vitrinite reflecting a greater amount of light. Samples collected for vitrinite reflectance analysis should be fine grained, organic rich, and were deposited in a setting that

included abundant input of terrestrial plant material. Additionally, because vitrinite is derived from land plant organic matter, this technique may only be used with post-Ordovician (<443.7Ma) lithologies.

Quartz cementation is one of the primary causes of porosity loss in sandstone reservoirs and is strongly temperature dependent, with little cementation occurring below temperatures of 75°-80°C (Walderhaug, 1994). Significant for petroleum geologists, this falls within the oil and gas generation windows (75°-120°C) (Tissot et al., 1987). The presence of quartz overgrowths depends on the availability of quartz-saturated water moving through the sandstone at temperatures sufficiently high to precipitate quartz.

Schneider and Johnson (1970) described the criteria necessary to use seismic data to differentiate between salt diapirs, differential compaction, igneous stocks, sediment diapirs, water circulation within sediments, buried hills/reefs, gas coning, and salt dissolution collapse features. Lohmann (1979) utilized these guidelines to identify salt diapirs off the Niger delta, in the Canary basin, and in the Oriente basin, Ecuador, and many other workers have followed suit in basis around the world, including in the western Pyrenees.

Additional tools to potentially measure heat flow around salt diapirs exposed at the surface are remote sensing instruments, which can have relative surface temperature accuracies of better than one degree. The Moderate Resolution Imaging Spectroradiometer (MODIS), onboard NASA's EOS Terra and Aqua satellites, has an absolute accuracy of 1K and a spatial resolution of



~1km/pixel (Fig. 8) (Wan et al., 2004). Effective remote sensing analysis depends upon vegetation, slope, surface albedo, lithology, weather, and human infrastructure, all of which can greatly distort surface temperature data and the effectiveness of space-borne remote sensing instruments. High water content in vegetation, in particular, can mask surface thermal anomalies.

### **Previous Studies**

In the past there has been some interest in the effects that salt diapirs could have on the maturity of surrounding sediments. However, the vast majority of that interest has manifested itself in the form of computer modeling, with few field-based investigations having been done.

Selig and Wallick (1966) used “high speed electrical computers” to mathematically model the temperature distribution differences between connected and disconnected cylindrical diapirs, as well as between diapirs that are stationary and those that are currently migrating. They estimated that above connected, buried diapirs the geothermal gradient is twice as large as over plain sedimentary overburden (Fig. 9). Additionally, their model suggests that the upper half of a diapir is warmer than surrounding sediments, but that the lower half is cooler, with a horizontal isogeotherm present through the center of the diapir. Furthermore, they speculated that heat generated by the friction of a moving diapir would significantly contribute to overall heat flow above a diapir. They also predicted that this frictional heat would also result in temperature

maxima occurring at the interface between salt and surrounding sediments at certain depths.

Rashid and McAlary (1977) utilized organic geochemistry to analyze organic matter present in wet gas, condensate, and 31 degree API oil present in three wells drilled above a salt diapir offshore Nova Scotia (Fig. 10). They compared bottom hole temperatures, corrected for mud circulation issues, and found consistently high heat flow directly above the Primrose salt diapir. They conducted carbon isotopic studies that linked hydrocarbons trapped above the Primrose diapir to source rocks within the area of thermal influence of the diapir. Carbon isotopes allowed them to eliminate the deeply buried Naskapi shale as potential source rock, reinforcing the evidence that the encountered hydrocarbons were locally produced as a result of anomalously elevated temperatures at these shallow depths (Fig. 11).

Jensen (1983) utilized the finite element method to model the temperature field around the Vejrum salt diapir in Denmark and suggested that heat flow near the top of the structure was twice the regional value with a maximum positive anomaly of  $\sim 10^{\circ}\text{C}$ . Jensen (1983) took local stratigraphy and the specific orientation and shape of the Vejrum diapir into consideration and estimated a  $20^{\circ}\text{C}$  negative temperature anomaly around the base of the diapir. Finally, Jensen (1983) compared various models with data from three wells near the diapir and found them to generally agree, though complications due to surface layer conductivity and the presence of groundwater were not accounted for in the model.

O'Brien and Lerche (1984) generated a model of a cylindrical salt dome of uniform thermal conductivity and constant vertical heat flux and compared the results to data from six wells on the flanks of a West Bay, Louisiana, salt dome. Their models predicted that surface heat flux above a shallowly buried diapir will have an intense, localized increase in surface heat flow, whereas a deeply buried diapir will have a less intense, broader increase in surface heat flow. Additionally, their models predict that the height of a diapir impacts the magnitude of the thermal anomaly but not its lateral extent. Therefore, the shape of the surface heat flux anomaly reflects the depth of burial and the radius of the diapir, while the magnitude of the anomaly is dependent upon the height of the diapir and the thermal conductivity contrast between the salt and surrounding sediments (Fig. 12).

O'Brien and Lerche (1984) note that the high heat flow above salt domes shallows the hydrocarbon window, and the low heat flow below salt domes deepens the hydrocarbon window. This serves to expand the overall hydrocarbon window and make salt domes attractive for exploration outside of their abilities to trap hydrocarbons. They found strong agreement between their models and well data, but note that their analysis does not provide a unique solution to the observed heat flow; changing geothermal gradients requires a change in the height of the dome in order for their model to work. By assuming a regionally reasonable geothermal gradient of 22-26°C/km, they calculated a salt dome height of 9,000 to 15,000m, with sediment thickness overlying the basal salt of 13,200-19,200m. Finally, they concluded that the lateral extent of thermal

anomalies around salt domes is confined to a distance of one dome radius from the flank of the dome.

In a companion paper to O'Brien and Lerche (1984), Vizgirda et al. (1985) modeled downhole temperatures from six wells at varying distances from the same West Bay salt dome in the Mississippi River birdfoot delta area, offshore Louisiana (Fig. 13). They assumed that the thermal anomaly is confined to within one radius of the salt diapir, and all six wells that provided data for this study are within that area. They utilized finite difference analysis to explain the observed thermal anomalies completely in terms of conductive heat transfer between the salt and surrounding sediments, without reference to other heat transfer mechanisms such as convective fluid flow. Additionally, by contrasting the predicted thermal anomalies of salt domes with semicircular, flat, and cone shaped top salt geometries, they determined that a cone shaped top salt diapir of 15,200m depth best reflects the observed data. They note that this is not a unique solution, but state that cross sections of the structure confirm a cone-top shape.

Mello et al. (1995) utilized the finite element method to model the temperature distribution of various salt diapir shapes in a hypothetical sedimentary basin. Their work suggested the presence of an asymmetrical dipolar temperature anomaly above and below a diapir that was still connected to "mother salt" but did not reach the surface (Fig. 14). This configuration resulted in higher heat flow above the diapir and along the upper half of the flanks of the diapir, but lower heat flow below the diapir and along the lower half of the flanks.

Contrastingly, their model of a diapir still connected to “mother salt” but that breaches the surface of a basin produced a monopolar temperature anomaly, with no positive heat flow above the dome or along its flanks (Fig. 15). They estimate that the maximum negative temperature anomaly (up to 85°C and extending vertically more than three times the diameter of the dome) is reduced by 10-15°C for every 250m of overburden above the top of the diapir. They then modeled vitrinite reflectance values for sediments (shale) around a salt diapir and sediments in a basin lacking salt. This analysis suggested that the basin with salt will have substantially delayed maturation (except directly over the salt dome) when compared to a similar basin that lacks salt.

Corrigan and Sweat (1995) used 2D modeling to compare the effectiveness of using sea floor heat flow measurements and gravity anomalies to constrain the geometry of salt diapirs. They note that depth to the top of the salt body is the single most important factor in recording high amplitude sea floor heat flow and gravity response anomalies. Additionally, the gravity response depends strongly upon the relation of the diapir to the density crossover depth (DCD), the point at which the salt becomes buoyant relative to surrounding sediments. They conclude that gravity data provide an order of magnitude better resolution of subsurface salt than sea floor heat flow measurements, provided that the area of focus is not at the density crossover depth.

Nagihara (2003) utilized 3D inverse heat flow modeling, based upon seafloor heat flow measurements and 2D seismic imaging, to determine the shape of the base of a salt tongue. Although the 3D inversion method provides

statistical information on the quality and uncertainty of various models, it still suffers from the problem of nonuniqueness. Nagihara's method allowed an evaluation of 56,000 models of diapir size, configuration, thermal conductivity, sea floor topography, and base salt geometry, and could be a more cost effective tool than 3D seismic in imaging salt diapirs.

## **CHAPTER 4**

### **Methodology**

The methodology of this project involved using multiple tools to determine the thermal maturity of sediments surrounding three salt structures in the western Pyrenees, Spain (Fig. 16). Vitrinite reflectance was chosen as the primary thermal maturity tool, and quartz cementation was used as a second potential paleotemperature indicator. Additionally, seismic and remote sensing data were utilized to attempt to determine the subsurface orientation and modern day heat flow of those salt structures.

#### **Vitrinite Reflectance**

Samples are ground and mounted in resin, and normal incident white light is reflected off the surfaces of grains of vitrinite. Forty five samples were sent for analysis to Egsploration Company, with analysis done by Lorraine Eglington. Samples were ground, cold set into an epoxy resin block, and polished to enhance particle relief and reflection. Glass and mineral samples of known reflection were used for calibration. However, a potential downfall of using vitrinite as a maturity indicator in this study is the subjective nature of measuring the reflectance of vitrinite grains.

#### **Quartz Cementation**

Eight samples surrounding the Ribera Alta diapir were cut into blocks and sent to be ground to thin sections at Quality Thin Sections in Tucson, Arizona.

They were impregnated with blue epoxy and analyzed for quartz overgrowths under both plane and cross polarized light.

### **Seismic Section and Well Logs**

To better constrain the subsurface geology of the Ribera Alta, Orduna, and Gernika salt structures, I requested sections from two regional seismic surveys from the Spanish Ministry of Industry. All seismic lines were digital scans of paper documents and included previous interpretations of horizons and faults. Additionally, we requested five well logs, which could provide information on the regional geothermal gradient. Any wells drilled through the Ribera Alta, Orduna, or Gernika diapirs would also provide information about the thickness, composition, and, potentially, orientation of the salt. Additionally, lithology descriptions within the well logs could provide information about the presence, or lack, of quartz cementing fluids, or provide evidence for past cementation of surrounding sediments.

### **Remote Sensing**

MODIS observes the entire earth's surface every 1-2 days, but this study utilized 8-Day Level 3 Land Surface Temperature/Emissivity V005 data. I collected data that covered the study area for every 8 days over a 5 year period. Remote sensing work was conducted for the Ribera Alta diapir, which is the southernmost locality, because it had the least dense vegetation.

The Ribera Alta diapir and its surrounding areas are dominated by farmland, mixed deciduous/conifer forest, and small villages, with a notable lack



of outcrops. In an effort to measure areas with the lowest water content possible, four pixels were chosen centered on cultivated fields. Pixels D1 and D2 are located within the diapir, and pixels ND1 and ND2 are 4.5km and 8.5km east of the diapir, respectively (Fig. 17).

## **CHAPTER 5**

### **Significance**

The significance of this project lies in testing the real world accuracy of the previously published models, most of which have been based on a relatively small amount of actual data from a limited number of diapirs. This is important because of the direct effect it may have on petroleum exploration around salt diapirs, which have historically been a focus of exploration as a result of their ability to trap petroleum. Additionally, basin modeling is highly dependent on an accurate understanding of the heat flow through a basin, especially in basins containing salt.

## **CHAPTER 6**

### **Results**

#### **Diapir History Reconstruction**

Schematic reconstructions of the Ribera Alta, Orduna, and Gernika salt structures were drawn, taking care to accurately depict diapir configuration at the time of sample deposition (Figs. 18-25 for Ribera Alta, Figs. 26-33 for Orduna, Figs. 34-40 for Gernika). Styles of deposition, deformation, and faulting of surrounding sediments at different stages of diapirism were drawn according to the general schematic put forth by Vendeville and Jackson (1992). Periods of reactive, active, and passive diapirism followed the regional timeline presented by Canerot et al. (2005), with notable revisions.

#### **Vitrinite Reflectance**

##### **Ribera Alta**

Twelve mudstone, siltstone, and sandstone samples from Miocene units surrounding the Ribera Alta diapir were sent for vitrinite reflectance analysis (Table 1, Figs. 41, 42, 43). The majority of samples contained low to very low organic matter and poor quality vitrinite, with some samples being virtually barren of organic matter. The average vitrinite reflectance value was 0.63, with samples ranging from 0.34 to 0.9. Pyrite is abundant in some of the samples, and glauconite is commonly present. One poor quality sample, 10RA14, was

recommended to be treated with caution, and so was omitted from further consideration.

### **Orduna**

Fourteen samples from Cretaceous units surrounding the Orduna diapir were analyzed for vitrinite reflectance (Table 2, Figs. 41, 44, 45, 46). In general, mudstones and marls had low to moderate organic matter content. Recycled vitrinite was much more common than primary vitrinite, with much of the primary vitrinite consisting of small, fair quality lenses. Differentiation between primary and recycled vitrinite was reportedly difficult, and intertinite was fairly common. Spore and algal fluorescence typically indicated a lower thermal maturity than the corresponding vitrinite reflectance values. The average vitrinite reflectance value was 0.82, with values ranging from 0.57 to 1.35. Sample 10OR22 had a reported vitrinite reflectance value of 0.35 but was omitted from further consideration due to uncertainties of the accuracy of its single grain of vitrinite.

### **Gernika**

Nineteen mudstone and marl samples from units surrounding the Gernika salt structure were analyzed for vitrinite reflectance (Table 3, Figs. 41, 47-51). In general they had low to moderate organic matter content, with the majority of the organic matter being terrestrially derived. Vitrinite was commonly present as

recycled particles, but primary vitrinite was commonly present as lenses, with occasional good quality stringers of more mature vitrinite in some samples. The average vitrinite value was 1.21, with values ranging from 0.83 to 1.86. Due to the low quality vitrinite in sample 10GE52, it was given a “treat with caution” note, and so has been omitted from further study.

### **Quartz Cementation**

Eight samples (10RA1-10RA8) from units surrounding the Ribera Alta diapir were cut into blocks and ground to thin sections. They were impregnated with blue epoxy and analyzed for quartz overgrowths under both plain and cross polarized light. Upon examination, all of the samples were heavily micritic, with grains ranging in size from less than 0.01mm to 0.2mm (Figs. 52-59), and multiple samples had forams present. None of the samples had any evidence of intergranular porosity or quartz cementation, likely due to early carbonate cementation. These samples contained very few detrital quartz grains. Samples around Ribera Alta, Orduna, and Gernika were primarily collected for vitrinite reflectance, which resulted in a focus on black shales and mudstones. These lithologies are not conducive for quartz cement, which would most likely be found in high porosity, high permeability, coarse grained sandstones.

## **Seismic Section and Well Log Interpretations**

### **Aulesti Well Log**

The Aulesti well is located 2km north east of the Gernika field area. The well was spudded on February 14, 1993 and reached a total depth of 3416.5m on July 8, 1993. The well targeted a sandstone member of the Gaviota Formation in a NW-SE trending anticline. The nearest existing well was Vizcaya C-2, at a distance of 13km. Drilling primarily through Cretaceous, Jurassic, and Triassic limestones, marls, and shales, the Triassic Keuper evaporite was encountered at a depth of 2827m, consisting of translucent, crystalline anhydrite and massive milky white to translucent halite.

From a depth of 0-1560m, the geothermal gradient was 23.6°C/km. From 1560-2802m the geothermal gradient was 20.7°C/km. From 2802-3416m the geothermal gradient was 16.6°C/km. The geothermal gradient at the total depth of 3416m was 21.3°C/km (Fig. 60).

Tmax values were measured on samples taken every several hundred meters. From 660-2680m, Tmax values ranged from 342°C to 389°C. After the Keuper evaporite was penetrated, Tmax values abruptly rose to around 440°C.

### **San Antonio Well Log**

The San Antonio well is located about 5km north of the Ribera Alta diapir. It was spudded on February 5, 1982 and reached a total depth of 5292.3m on

January 26, 1984. The primary objective was a presalt anticline in the Bunt Formation, identified on seismic. After drilling through 4455m of upper Cretaceous limestones, marls, and clayey shales, the Keuper evaporite was encountered as massive halite with areas of white anhydrite. At a depth of 5292.3m the well was suspended without reaching the final objective. No Tmax data were reported for the San Antonio well.

### **1\_71T 2D Seismic Grid**

This seismic grid is centered north of the Ribera Alta diapir (Fig. 61). The data packet consists of four preinterpreted seismic sections, isochrons for three horizons, a drill schedule, map, logistical summary, and a copy of the Seismic Completion Report. The data for this seismic block were acquired in June, July, and October, 1971, by Empresa Nacional De Petroleos De Aragon (ENPASA). Three horizons were consistently traceable throughout the seismic lines (marked as red lines), though no names for these horizons were given beyond "Line 2," "Line A," and "Line 6." Additionally, small non-laterally traceable horizons were marked in yellow.

#### **Line ZU1**

Seismic line ZU1 (Figs. 61, 62) runs roughly north-south, covering the northern flank of the Ribera Alta diapir. North of the diapir horizons "2" and "A" dip gently southward, while the deepest horizon (horizon "6") dips towards the north. As the line approaches the diapir, horizon "2" and horizon "A" dip deeper and are no longer traceable. Horizon "6" is interpreted as remaining horizontal

below the diapir, but this interpretation has a high degree of uncertainty. The outline of the diapir is not explicitly marked, but its subvertical orientation is suggested by the lack of consistent reflectors above horizon “6” on the southern end of the seismic line. Line ZU1 extends to approximately the center of the Ribera Alta diapir, providing only half of a cross section through the diapir.

#### Line ZU2

Line ZU2 runs north-south, roughly parallel to ZU1, and is located east of the diapir (Figs. 61, 63). Horizons “2” and “A” are interpreted as generally dipping to the south and are offset by a reverse fault (“F5”) with minor throw. Horizon “6” dips to the north and is intercepted by a reverse fault (“F4”) of moderate offset that also intercepts horizons “2” and “A”. Horizons “2” and “A” are not interpreted south of fault F4. Seismic line ZU2 is located too far east to include the Ribera Alta diapir.

#### Line ZU4

Seismic line ZU4 runs parallel to lines ZU1 and ZU2 and is located west of the diapir (Figs. 61, 64). It is a single line but data are absent in the middle of the line. The southern section is interpreted as having horizons 2, A, and 6 all dipping to the south. Inconsistent horizons above, below, and between these three notable horizons follow a similar trend. Seismic line ZU4 is located too far west to include the Ribera Alta diapir.

#### Line ZU5



Seismic line ZU5 runs roughly east-west and is located north of the Ribera Alta diapir (Figs. 61, 65). It intercepts lines ZU4, ZU1, and ZU2. In its easternmost and westernmost sections, horizons “2,” “A,” and “6” are all interpreted as being horizontal. Near the center of the line, however, the horizons are domed and offset by reverse faults. Fault 1 (“F1”) intercepts all three horizons and shows increasing offset with increasing depth. Fault 2 (“F2”) intercepts horizons “2” and “A” with moderate offset, and does not extend to horizon “6,” the deepest horizon. Fault 3 (“F3”) is similar to F1 in that it intercepts all horizons, but it does not have increasing offset with depth. Instead, the greatest offset is interpreted to occur in horizon “A,” the middle horizon, with horizons “2” and “6” having smaller offsets. Line ZU5 does not intercept the Ribera Alta diapir, but it does intersect what I interpret to be radially extending normal faults.

### **Remote Sensing**

MODIS Level 3 Land Surface Temperature/Emissivity V005 data were collected every 8 days from 2005 to 2009 for four pixels within and around the Ribera Alta diapir. Pixels D1 and D2 are located within the Ribera Alta diapir, ND1 is 4.5km to the east, and ND2 is 8.5km to the east (Fig. 15). Temperatures for pixels D1 and D2 are plotted in Figure 66.

## CHAPTER 7

### Discussion

Samples collected from around the Ribera Alta diapir are mid Miocene (~13Ma) in age and are significantly younger than samples collected from around the Orduna diapir, which are Cretaceous (Turonian, Coniacian) in age (~90Ma). Samples collected from around the Gernika salt weld are Cretaceous in age (primarily Albian and Campanian) (105, 75Ma). The average vitrinite value for Ribera Alta is 0.63, and the average value for Orduna is 0.82. Gernika samples have an average vitrinite value of 1.21.

In addition to uncertainties inherent to the use of vitrinite reflectance as a maturity indicator, maturity values for the three salt structures are dependent upon the stratigraphic level at which samples were collected. Ideally, samples would have been collected at the same stratigraphic level at each salt structure. However, access to suitable outcrops greatly limited where samples were collected, and as a result of this samples were collected from different stratigraphic levels. This is clearly shown at the Orduna diapir, where some samples were derived from units ~500m deeper than other samples (Figs. 6, 67). This added a notable source of uncertainty into these data.

#### **Ribera Alta and Orduna**

Vitrinite reflectance values around the Ribera Alta and Orduna diapirs show lower values closer to the diapirs, with sediment maturity increasing as distance from a diapir increases. I infer that the diapirs caused lower heat flux in

surrounding sediments, leaving them less mature compared to regional values. Regional values for Orduna are around 1.05, but samples close to the diapir are around 0.7 and dip as low as 0.57 (Fig. 67, 68). Regional values for Ribera Alta are around 0.75, but samples near the diapir are as low as 0.34 (Fig. 69, 70). In a plot of maturity vs. distance, Orduna samples show a robust confirmation that samples near the diapir are cooler than samples further from the diapir (Fig. 71). A similar plot for Ribera Alta is less clear, but still suggests that the diapir acts to suppress temperatures in surrounding sediments (Fig. 72).

I placed vitrinite reflectance values from the Ribera Alta and Orduna diapirs in the context of previously published numerical modeling studies. Mello et al. (1995) modeled that diapirs that breach the surface have monopolar temperature anomalies around the diapir. In this model, all surrounding and underlying sediments will be undermature with respect to regional values (Fig. 73). Subsurface heat is drawn up the diapir and is vented to the atmosphere or sediment/water interface, and no positive temperature anomaly in sediments is created. This is in contrast to the model of a diapir that has not breached the surface. According to Mello et al.'s model, when a diapir is buried a dipolar thermal anomaly is created. Instead of heat flow being vented to the atmosphere, it is channeled to overlying sediments (Fig. 74). In this scenario, sediments below the midpoint of the diapir are undermature and sediments above the midpoint are overmature.

At face value, data from the Ribera Alta and Orduna diapirs fit into either a monopolar or a dipolar thermal anomaly model. In one scenario, the diapirs were

buried, resulting in a dipolar thermal anomaly in surrounding sediments, with sediments above the midpoint of the diapir being overmatured and sediments below the midpoint of the diapir being undermatured. Subsequently, the diapirs and surrounding sediments were eroded deep enough so that the overmature sediments were erased from the rock record, leaving the undermature surrounding sediments exposed at the surface today (Fig. 75). However, it is also possible that the thermal maturity patterns around the Ribera Alta and Orduna diapirs are reflective of a monopolar thermal anomaly. This would require the diapirs to have been exposed at the surface for a long enough period of time to establish the observed maturity patterns (Fig. 75).

Canerot et al. (2005) suggested that during the late Cenomanian (93Ma) many Pyrenean diapirs exhausted their supply of salt, leading to diapir collapse and burial. Canerot et al. (2005) note, however, that the age of diapir burial is loosely constrained and could have occurred later in the Basque-Cantabrian basin. Samples collected around the Orduna diapir are late Turonian (90Ma) in age. If Canerot et al. (2005) are correct that the diapir was buried by the late Cenomanian (93Ma), then our samples were deposited while the diapir was buried. This would have resulted in a dipolar thermal anomaly in surrounding sediments, with our samples being located above the diapir and receiving elevated heat flow. This is in contrast to the observed maturity of sediments surrounding Orduna, which are less mature than regional values. I propose that sediments around the Orduna diapir had their maturities suppressed due to the presence of a monopolar thermal anomaly. This monopolar thermal anomaly was

due to the exposure of the Orduna diapir at the surface during the time that our samples were deposited. Therefore, I propose that the Orduna diapir was not buried during the late Cenomanian, as was previously thought, but was buried after the late Turonian. After diapir burial a dipolar thermal anomaly was formed, increasing the maturity of overlying sediments and preserving the maturity of underlying sediments. In order to preserve the established maturity patterns of our samples, they must have been buried deeply enough to not have been affected by the dipolar thermal anomaly. Subsequent uplift and erosion from the Paleocene to the present resulted in the removal of any evidence of a dipolar thermal anomaly and led to the exposure of the samples at the surface (Figs. 26-33).

Similar to the Orduna diapir, the Ribera Alta diapir was buried at some time during the late Cretaceous and was uplifted and eroded starting in the Paleocene. However, Arostegui et al. (2006) state that erosion and deposition were highly localized from the Oligocene to the Pliocene. They propose that the Miranda-Trevino syncline, in which the Ribera Alta diapir is located, was the site of deposition of molasses sediments from the Oligocene (35Ma) to the Pliocene (4.4Ma). I propose that thick sedimentation during this period served to renew passive downbuilding of sediments around the Ribera Alta diapir. Our Miocene age Ribera Alta samples were deposited in this setting, with a monopolar thermal anomaly surrounding the exposed diapir (Figs. 18-25). As a result of this, sediments that I sampled had their maturities suppressed compared to regional values.

Vizgirda et al. (1985) and other workers have suggested that diapir thermal anomalies are confined to within one radius from the diapir edge. They took measurements from six wells around a West Bay, Louisiana salt dome, but did not include wells further than one radius from the dome. Samples around Ribera Alta extend to a distance of 3x the radius of ~2km, and samples around Orduna extend to a distance of 4x the radius of ~2km. The average vitrinite reflectance for Orduna is 0.82, with samples closest to the diapir ranging from 0.81 to 0.57. Orduna samples furthest from the diapir measure 1.05 and 1.09, and it is likely that these samples represent regional maturity values (Fig. 76). The average vitrinite reflectance for Ribera Alta is 0.63, but samples along the diapir edge range from 0.34 to 0.90, presenting less clear data than at Orduna (Fig. 77). Nevertheless, vitrinite reflectance patterns around the Orduna and Ribera Alta diapirs suggest that thermal anomalies are confined to within approximately one and a half radii (3km) of the diapir edge. The Orduna diapir is slightly larger than the Ribera Alta diapir. However, our samples have insufficient resolution to confidently state that the thermal anomaly around Orduna is greater than that around Ribera Alta.

### **Gernika**

Subsalt and suprasalt samples, separated by a weld, were collected at Gernika. In accordance with the modeled heat flow of an inclined diapir not connected to the surface, subsalt samples should be regionally undermature and suprasalt samples should be regionally overmature.

At first glance, vitrinite reflectance values for sediments surrounding the Gernika salt weld offer no clear correlation between maturity and distance (Fig. 78). Unlike the Ribera Alta and Orduna diapirs, the Gernika salt weld does not have a clear circular/elliptical surface exposure (Fig. 7). Additionally, the subsurface configurations of Ribera Alta and Orduna are vertical to subvertical, based on available map cross sections and seismic data. However, the subsurface configuration of the Gernika weld, based on the interpreted cross sections, reveals the diapir root to be located 1km north of the nearest surface diapir exposure and 4km north of the center of our sample collection area. Surface exposures of the Gernika salt weld are not located directly over the root of the diapir, as is the case for Orduna and Ribera Alta.

A plot of vitrinite reflectance vs distance, as measured from a diapir outcrop (“Outcrop 1”) near many of the samples, does not suggest any type of a correlation between maturity and distance (Fig. 79). However, maturity contour lines for subsalt and suprasalt areas (as separated by the salt weld) reveal that suprasalt samples are generally more mature than subsalt samples (Fig. 80, 81). Additionally, there is a general decrease in maturity for samples closer to the root of the weld, similar to the results around the Ribera Alta and Orduna diapirs (Fig. 80).

### **Remote Sensing**

Temperatures for diapir pixels D1 and D2 closely track each other over the 5 years for which data was gathered. Nondiapir pixels ND1 and ND2 are also

very similar over the 5 years. In comparing diapir and nondiapir pixels, there is no consistent discernible difference between them (Fig. 82).

Remote sensing results show that satellites can be a useful tool in detecting present day heat flow above exposed salt diapirs. However, this tool is only effective in locations where vegetation is sparse or nonexistent. My studies of La Popa basin, Mexico showed that MODIS data can be used to map the thermal anomalies associated with salt diapirs. In La Popa basin during the winter, temperatures over El Gordo diapir were up to 7°C warmer than temperatures over a nondiapir site located 50km to the west at similar altitude (Figs. 83, 84). During the hot summer months, the diapir and nondiapir locations showed no discernible difference in temperatures. I believe the absence of an observable temperature anomaly during the summer is due to the hot summer conditions in La Popa basin masking the subtle temperature difference between diapir and nondiapir sediments. The winter temperature anomaly is due to subsurface heat flow through the diapir and to residual solar heating carried over from the summer into the winter. In this respect, diapirs act analogously to lakes, with lakes retaining their summer heat into the winter and retaining their low winter temperatures into the spring. Similarly, the high thermal conductivity of salt diapirs allow seasonal variations in temperature to penetrate significantly deeper into the diapir than into surrounding clastic sediments.

La Popa basin is set in a desert environment, with little vegetation present. This is in contrast to the Ribera Alta diapir, which has extensive cultivated and forested cover. The high moisture content in vegetation acts to mask any thermal



signature that can be detected by remote sensing instruments. These results suggest that MODIS data may be useful in detecting thermal anomalies associated with salt diapirs only in climates with sparse vegetative cover.

## CHAPTER 8

### Conclusions

Data from this study confirm that salt diapirs can have a significant impact on the thermal maturity of surrounding sediments. The magnitude and nature of that impact depends on many factors, including the size and orientation of the diapir and the regional geological history. Vitrinite reflectance is a useful tool in determining the maximum paleotemperatures experienced by sediments and can be used to reconstruct the history of a diapir and its surrounding sediments. The Ribera Alta and Orduna diapirs are examples of how salt diapirs can suppress the maturity of surrounding sediments. Data around the Gernika salt weld support the hypothesis that sediments above an inclined weld will be more mature than sediments below an inclined weld. My results show that thermal anomalies around diapirs are confined to within approximately 1.5x the radius of a diapir, in contrast to the previous modeled extent of 1x the radius. Finally, remote sensing can be a useful tool in measuring present day heat flow over exposed diapirs, provided that they are located in a region with low vegetative cover (Fig. 85).

The significance in understanding how diapirs affect the thermal maturity of surrounding sediments is primarily related to petroleum source rock maturity and reservoir preservation. For a diapir that has been exposed at the surface and buried multiple times, there could be highly variable maturities along the flanks of that diapir. This could have a direct impact on when, and at what stratigraphic

level, source rocks surrounding the diapir entered the oil window and produced hydrocarbons. Additionally, the presence or absence of quartz cementation in reservoir rocks surrounding a diapir could have a significant impact on hydrocarbon migration, reservoir preservation, and general prospectivity. Diapir-related thermal anomalies could serve to suppress the maturities of deeply buried source and reservoir rocks, such as what has been seen in recent “sub-salt” petroleum plays around the world.

The lateral extent and magnitude of thermal anomalies around diapirs will control the degree to which diapirs affect the petroleum system within a basin. Data from this study suggest that the thermal anomalies around diapirs extend to 1.5x the radius of the diapir, which is in contrast to the modeled extent of 1.0x the radius. This suggests that diapirs could have a notably larger impact on surrounding sediments than had previously been thought.

There is still significant work that should be done to better constrain the results of this research. Because outcrop data represent a single two dimensional plane of maturity values around a diapir, an area of future work could be attempting to constrain maturities around a diapir in three dimensions, perhaps through the use of well log data. Data from salt mines may also be used to measure present day heat flow in three dimensions within a diapir. The use of remote sensing instruments to analyze modern heat flow around a diapir is also an area that would benefit from future investigation. Diapirs in arid climates such as in the Paradox Basin, Utah, the Great Kavir, Iran, or the Ghaba Salt Basin, Oman could all be remotely analyzed to measure heat flow differences between

diapirs and surrounding sediments. High resolution satellite imagery, such as from the Advanced Spaceborne Thermal Emission and Reflection Radiometer (ASTER) could be used in conjunction with MODIS data to study diapir-related heat flow in much greater detail.

## References

- Arostegui, J., Sanguesa, F. J., Nieto, F., and Uriarte, J. A., 2006, Thermal models and clay diagenesis in the Tertiary-Cretaceous sediments of the Alava block (Basque-Cantabrian basin, Spain): *Clay Minerals*, v. 41, p. 791-809.
- Benanav, M., 2006, *Men of Salt*: Guilford, Connecticut, the Lyons Press, 256 p.
- Canerot, J., Hudec, M., and Rockenbauch, K., 2005, Mesozoic diapirism in the Pyrenean orogen: Salt tectonics on a transform plate boundary: *American Association of Petroleum Geologists Bulletin*, v. 89, no. 2, p. 211-229.
- Corrigan, J. and Sweat, M., 1995, Heat flow and gravity responses over salt bodies: a comparative model analysis: *Geophysics*, v. 60, p. 1029-1037.
- Gibbons, W., and Moreno, T., editors, 2002, *The Geology of Spain*: London, Geological Society, 649 p.
- Gonzalez, C., Valverde, I., and Lafuente, A. L., 2007, Mineralogical and geochemical characterization of a diapiric formation in the North of Spain: *Catena*, v. 70, p. 375-387.
- Jensen, P. K., 1983, Calculations on the thermal conditions around a salt diapir: *Geophysical Prospecting*, v. 31, p. 481-489.
- Lohmann, H., 1979, Seismic Recognition of Salt Diapirs: *American Association of Petroleum Geologists Bulletin*, v. 63, no. 11, p. 2097-2102
- Mello, U. T., Karner, G. D., and Anderson, R. N., 1995, Role of salt in restraining the maturation of subsalt source rocks: *Marine and Petroleum Geology*, v. 12, p. 697-716.

- Nagihara, S., 2003, Three-dimensional inverse modeling of the refractive heat-flow anomaly associated with salt diapirism: *American Association of Petroleum Geologists Bulletin*, v. 87, no. 7, p. 1207-1222.
- O'Brien, J. J., and Lerche, I., 1984, The influence of salt domes on paleotemperature distributions: *Geophysics*, v. 49, p. 2032-2043.
- Rashid, M. A., and McAlary, J. D., 1977, Early maturation of organic matter and genesis of hydrocarbons as a result of heat from a shallow piercement salt dome: *Journal of Geochemical Exploration*, v. 8, p. 549-569.
- Rios, J. M., 1968, Saline Deposits of Spain, *in Saline Deposits, A Symposium based on Papers from the International Conference on Saline Deposits, Houston, Texas, 1962*, p. 59-74.
- Robertson, E. C., 1988, Thermal properties of rocks: U.S. Geological Survey, Open-File Report 88-441, 106 p.
- Ruiz, A. G., and Jimenez, L. M., 1991, Basque Country geological map: Ente Vasco de la Energia, scale 1:25,000, 10 sheets.
- Schneider, E. D., and Johnson, G. L., 1970, Deep-Ocean Diapir Occurrences: *American Association of Petroleum Geologists Bulletin*, v. 54, no. 11, p. 2151-2169.
- Selig, F., and Wallick, G. C., 1966, Temperature distribution in salt domes and surrounding sediments: *Geophysics*, v. 31, p. 346-361.
- Tissot, B. P., Pelet, R., and Ungerer, P.H., 1987, Thermal history of sedimentary basins, maturation indices, and kinetics of oil and gas generation: *American Association of Petroleum Geologists Bulletin*, v. 71, p. 1445-1466.

- Vendeville, B. C., and Jackson, M. P. A., 1992, The rise of diapirs during thin skinned extension: *Marine and Petroleum Geology*, v. 9, p. 331-353.
- Vizgirda, J., O'Brien, J. J., and Lerche, I., 1985, Thermal anomalies on the flanks of a salt dome: *Geothermics*, v. 14, no. 4, p. 553-565.
- Walderhaug, O., 1994, Temperatures of quartz cementation in Jurassic sandstones from the Norwegian continental shelf-evidence from fluid inclusions: *Journal of Sedimentary Research*, v. A64, no. 2, p. 311-323.
- Wan, Z., Zhang, Y., and Zhang, Q., 2004, Quality assessment and validation of the MODIS global land surface temperature: *International Journal of Remote Sensing*, v. 25, no. 1, p. 261-274.
- Waples, D. W., 1980, Time and Temperature in Petroleum Formation Application of Lopatin's Method to Petroleum Exploration: *American Association of Petroleum Geologists Bulletin*, v. 64, no. 6, p. 916-926.

**Table 1 (Ribera Alta):**

Sample	Vitrinite Reflectance (Ro)	Count	Standard Deviation	Confidence (95%)	Notes	Distance from Diapir edge (km)
10RA1	0.34	3	0.02	0.06	Marl virtually barren. Difficult to distinguish primary/recycled vitrinite. Glauconite and occasional hematite spots present.	0.66
10RA4	0.42	3	0.04	0.09	Very low organic matter. A few poor quality particles of vitrinite, very minor inertinite. Pyrite abundant, glauconite present, occasional hematite spots.	1.34
10RA7	0.76	2	0.02	0.21	Very low organic matter. Small, poor quality vitrinite, very minor inertinite. Fluorescence is mineral derived and devoid of liptinite except for one bright yellow-orange algal cyst.	6.17
10RA9	0.73	4	0.05	0.08	Very low organic matter. Poor to fair quality vitrinite, minor inertinite. Liptinite content very low, one yellow fluorescing algal cyst. Other fluorescence is mineral derived.	10.79
10RA10	0.54	1	NA	NA	Very low organic matter. One small, poor quality particle of vitrinite. Pyrite abundant, glauconite present. Liptinite content is trace and one light orange fluorescent spore. Other fluorescence mineral derived.	1.78
10RA11	0.76	3	0.02	0.05	Very low organic matter. One or two tiny particles of vitrinite, equally minor inertinite. Glauconite present. One tentatively identified algal cyst fluoresces yellow, otherwise fluorescence mineral derived.	1.94
10RA13	0.79	8	0.02	0.02	Low to moderately abundant organic matter. Lenses of vitrinite and minor recycled vitrinite. Glauconite present. Tentatively identified spores and algal matter fluoresce light orange and yellow, respectively.	3.06
10RA14	0.81	1	NA	NA	Barren marl. One particle of probable vitrinite, one dark orange spore. <b>Treat data with caution.</b>	2.34
10RA16	0.9	3	0.01	0.03	Trace organic matter. Only three particles of vitrinite, possibly recycled. No liptinite content.	0.81
10RA17	0.72	4	0.04	0.06	Low organic matter. Lenses of vitrinite and recycled vitrinite. Glauconite present, pyrite abundant. Tentatively identified algal matter fluoresces yellow to yellow orange.	0.4
10RA19	0.66	3	0.02	0.05	Virtually barren of organic matter. Three particles of possibly primary vitrinite. Glauconite is present. Algal cysts fluoresce yellow orange and one spore fluoresces light orange to mid orange.	1.27



10RA20	0.69	3	0.01	0.02	Mudstone and marl have low organic matter and are diatomaceous. Fair to poor quality vitrinite. Pyrite abundant, fluorescence mineral derived except for one yellow algal cyst and one mid-orange spore.	3.18
--------	------	---	------	------	--	------

**Table 2 (Orduna):**

Sample	Vitrinite Reflectance (Ro)	Count	Standard Deviation	Confidence (95%)	Notes	Distance from Diapir (km)
10OR21	0.68	3	0.05	0.11	Low organic matter. Vitrinite minor, recycled vitrinite/inertinite more common. Liptinite characterized by trace contribution from green algal cysts.	0.15
10OR22	0.35	1	NA	NA	Very low organic matter. One particle of vitrinite. Glauconite present, pyrite abundant. Minor algal matter fluoresces yellow, one tenuispore fluoresces yellow-orange.	0.1
10OR24	0.57	3	0.04	0.09	Low to moderate organic matter content. Vitrinite lenses are of fair quality. Abundant pyrite. Tentatively identified algal matter fluoresces yellow, one spore fluoresces yellow-orange.	0
10OR25	0.78	7	0.04	0.04	Low to moderately abundant organic matter. Some recycled vitrinite with very minor inertinite. Abundant pyrite. Abundant mineral fluorescence and trace green-yellow algal matter fluorescence.	0
10OR27	0.8	6	0.06	0.06	Low to moderate organic matter. Two distinct populations. Low population is primary vitrinite, more mature population is recycled. Abundant pyrite, spores fluoresce yellow to yellow-orange, algal matter fluoresces green.	0.2
10OR28	0.81	9	0.06	0.05	Moderately abundant to rich organic matter. Vitrinite mostly recycled, some of which are poor quality. Algal cysts fluoresce green, spores fluoresce mid-orange.	0
10OR30	0.72	10	0.05	0.04	Low to moderate organic matter, abundant foraminifera tests. Some vitrinite degraded, with some recycled vitrinite and minor inertinite. Abundant pyrite. Algal matter fluoresces green-yellow, two spores fluoresce light orange and mid orange.	1.25
10OR31	0.76	6	0.06	0.06	Low organic matter. Foraminifera tests. Minor vitrinite with more plentiful recycled vitrinite and minor inertinite. Abundant pyrite. One spore fluoresces light orange, dinoflagellate cysts fluoresce green.	1.85
10OR33	0.81	6	0.03	0.04	Low to moderate organic matter, abundant foraminifera tests. Mainly small lenses of vitrinite of varying quality and occasional stringers. Recycled vitrinite and inertinite particles present. Abundant pyrite. Spores fluoresce mid-orange to dark orange, algal matter fluoresces yellow-orange.	2.9
10OR34	0.92	7	0.07	0.07	Moderately abundant organic matter. Lenses of varying quality vitrinite and recycled vitrinite with minor inertinite. Abundant pyrite. Algal matter	1.2

					fluoresces mid-orange to dark orange.	
10OR36	1.35	1	NA	NA	Low organic matter, abundant foraminifera tests. Dominated by recycled vitrinite and inertinite, trace primary vitrinite. Fluorescence mineral derived.	1.74
10OR37	0.84	3	0.11	0.28	Low organic matter content. A few lenses of vitrinite and minor inertinite. Abundant pyrite, fluorescence appears to be mineral derived. Possible trace green algal cysts.	2.27
10OR39	1.05	6	0.05	0.06	Low to moderately abundant organic matter. Lenses of vitrinite and recycled vitrinite with minor inertinite. Abundant pyrite, majority of fluorescence is mineral derived. One dinoflagellate cyst that fluoresces green-yellow. One spore fluoresces weak light orange.	5.76
10OR40	1.09	5	0.03	0.04	Moderately abundant organic matter. Equal contributions of vitrinite, recycled vitrinite, and inertinite. Abundant pyrite, some algal matter fluoresces light orange and mid-orange.	8.46

**Table 3 (Gernika):**

Sample	Vitrinite Reflectance (Ro)	Count	Standard Deviation	Confidence (95%)	Notes	Distance from Diapir Root (km)	Distance from Diapir Outcrop 1 (km)
10GE42	1.42	5	0.06	0.08	Low organic matter. Equal parts vitrinite, recycled vitrinite, inertinite. Abundant pyrite, no organic matter fluorescence.	3.71	0.79
10GE43	1.2	7	0.05	0.05	Abundant organic matter. Mainly high maturity vitrinite, some recycled vitrinite and inertinite. Abundant pyrite. Fluorescence is mineral derived.	4.16	0.31
10GE44	1.12	13	0.06	0.04	Abundant organic matter. Dominated by inertinite and recycled vitrinite, with almost equally abundant primary vitrinite as stringers and large lenses. Fluorescence mineral derived.	3.35	1.12
10GE45	1	12	0.06	0.04	High organic matter. Abundant good quality vitrinite as stringers and lenses. Moderate recycled vitrinite. No organic matter fluorescence.	2.68	1.9
10GE45 b	1	14	0.05	0.03	Abundant organic matter. Dominated by vitrinite, with inertinite and recycled vitrinite following. Abundant pyrite. No organic matter fluorescence.	3.08	1.42
10GE46	0.83	8	0.04	0.03	Low organic matter. Small fair quality vitrinite lenses, followed by minor recycled vitrinite and inertinite. Abundant pyrite. Some algal cysts fluoresce yellow and yellow orange.	2.53	3.05
10GE47	0.88	8	0.04	0.03	Abundant organic matter, dominated by inertinite as large coal-like fragments. Also recycled vitrinite and high reflecting minor primary vitrinite. Abundant pyrite. Trace dark orange spore fluorescence.	4.04	2.35
10GE48	1.04	10	0.05	0.04	Abundant organic matter dominated by inertinite and recycled vitrinite. Some vitrinite. Abundant pyrite. Fluorescence mineral derived.	3.91	2.37
10GE49	0.88	8	0.05	0.04	Abundant organic matter. Dominated by fair quality vitrinite and recycled vitrinite. Abundant non-fluorescing liptinite, moderate bitumen stain. Algal matter fluoresces yellow orange.	5.15	3.27
10GE50	1.78	5	0.05	0.06	Low to moderate organic matter. High reflecting vitrinite. Abundant pyrite, some mineral derived fluorescence	7.76	5.1

					(dolomite).		
10GE51	1.83	12	0.05	0.03	Moderate organic matter. Dominated by high reflecting vitrinite and recycled vitrinite. One or two large coaly fragments. Abundant pyrite, abundant mineral derived fluorescence.	7.8	4.83
10GE52	0.84	1	0	0	Very little organic matter. One small fragment of vitrinite. Fluorescence mineral derived. <b>Treat data with caution.</b>	7.99	5.55
10GE53	0.87	10	0.06	0.04	Moderate organic matter. A few good quality bits of vitrinite, more abundant lenses/stringers of recycled vitrinite and inertinite. Fluorescence mineral derived.	7.67	5.92
10GE54	0.97	14	0.05	0.03	Moderate organic matter. Mainly small lenses of primary vitrinite, followed by recycled vitrinite and inertinite. Fluorescence mineral derived.	7.27	3.88
10GE55	1.1	7	0.04	0.04	Moderate organic matter. Mainly small lenses of high reflecting vitrinite and recycled vitrinite. One algal cyst fluoresces yellow orange, otherwise fluorescence mineral derived.	6.88	3.43
10GE56	1.25	4	0.05	0.08	Moderate organic matter. Mainly high reflecting lenses/stringers of primary vitrinite, followed by recycled vitrinite. Abundant pyrite. One algal cyst that fluoresces yellow orange.	6.6	2.95
10GE57	1.54	8	0.04	0.04	Moderate organic matter. High reflecting lenses of primary vitrinite and recycled vitrinite. Fluorescence mineral derived.	5.94	1.76
10GE58	1.86	11	0.03	0.02	Moderate to rich organic matter. Mainly lenses of high reflecting vitrinite and recycled vitrinite. Fluorescence mineral derived.	5.75	1.37
10GE59	1.59	12	0.07	0.05	Abundant organic matter. Mostly poor quality, degraded, high reflecting vitrinite. Also abundant recycled vitrinite and inertinite. Fluorescence mineral derived.	4.95	0.55

## Nicholas Downs

### EDUCATION:

#### **University of Nevada, Las Vegas**

M.S. Geology  
GPA: 3.73  
Anticipated Graduation Date: 5/2012

#### **Duke University**

B.S. Earth and Ocean Sciences  
Major GPA: 3.425  
Cumulative GPA: 3.155

#### **American School of Doha**

Doha, Qatar  
Achievements include:  
Graduation Commencement Speaker  
National Honor Society Vice President  
Founding Scout and Senior Patrol Leader, Troop 970

### WORK EXPERIENCE:

#### **English Language School**

Doha Qatar  
5/10/2005—7/10/2007  
Senior English teacher with >800 hours classroom experience

### RESEARCH EXPERIENCE:

Dates: January, 2009—May, 2009  
Adviser: Lincoln Pratson, Duke University  
Subject: Investigating suspected turbidity current inflow into Lake Powell during a drought.

Dates: January, 2010—August, 2010  
Adviser: Andrew Hanson, University of Nevada, Las Vegas  
Subject: Evaluating potential petroleum source rocks in Nye County, Nevada.

Dates: August, 2010—Present  
Adviser: Andrew Hanson, University of Nevada, Las Vegas  
Subject: Investigating the effects of salt diapirs on the thermal maturity of surrounding sediments in the western Pyrenees, Spain.

### AWARDS:

3<sup>rd</sup> Place 2011 AAPG Imperial Barrel Award (Rocky Mountain Region)

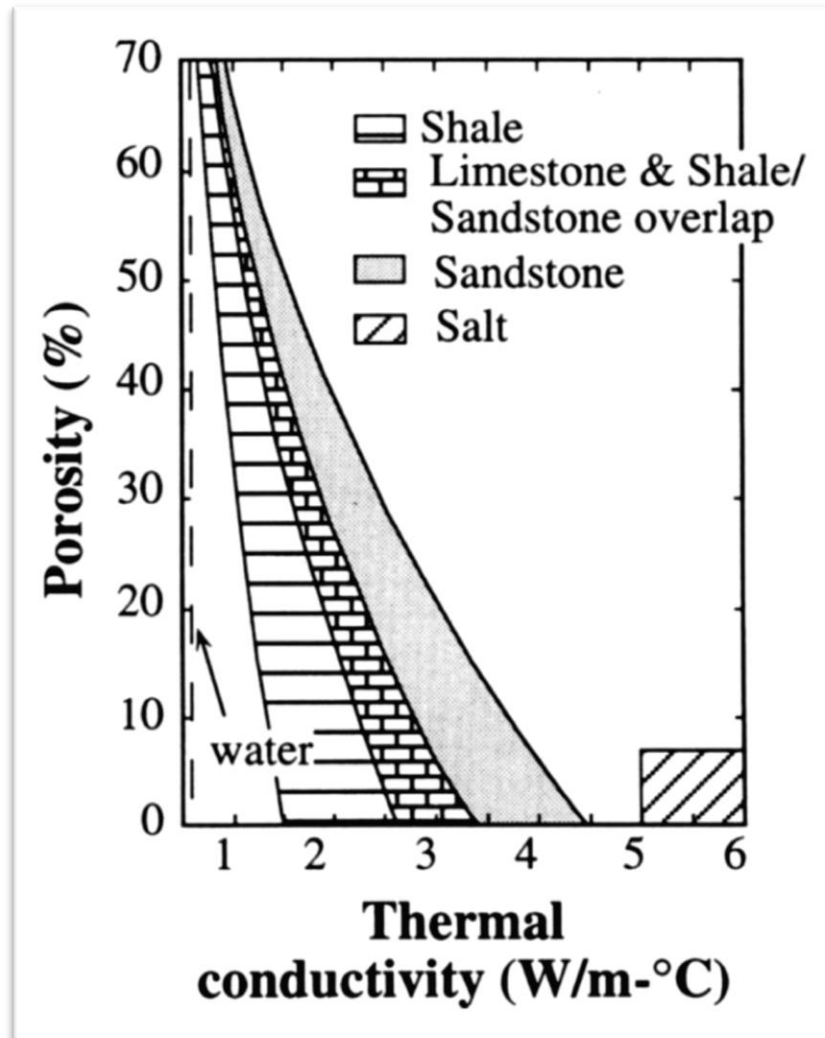
### OTHER SKILLS, ACTIVITIES, AND INTERESTS:

Proficient in seismic interpretation using Petrel

UNLV AAPG Student Chapter President

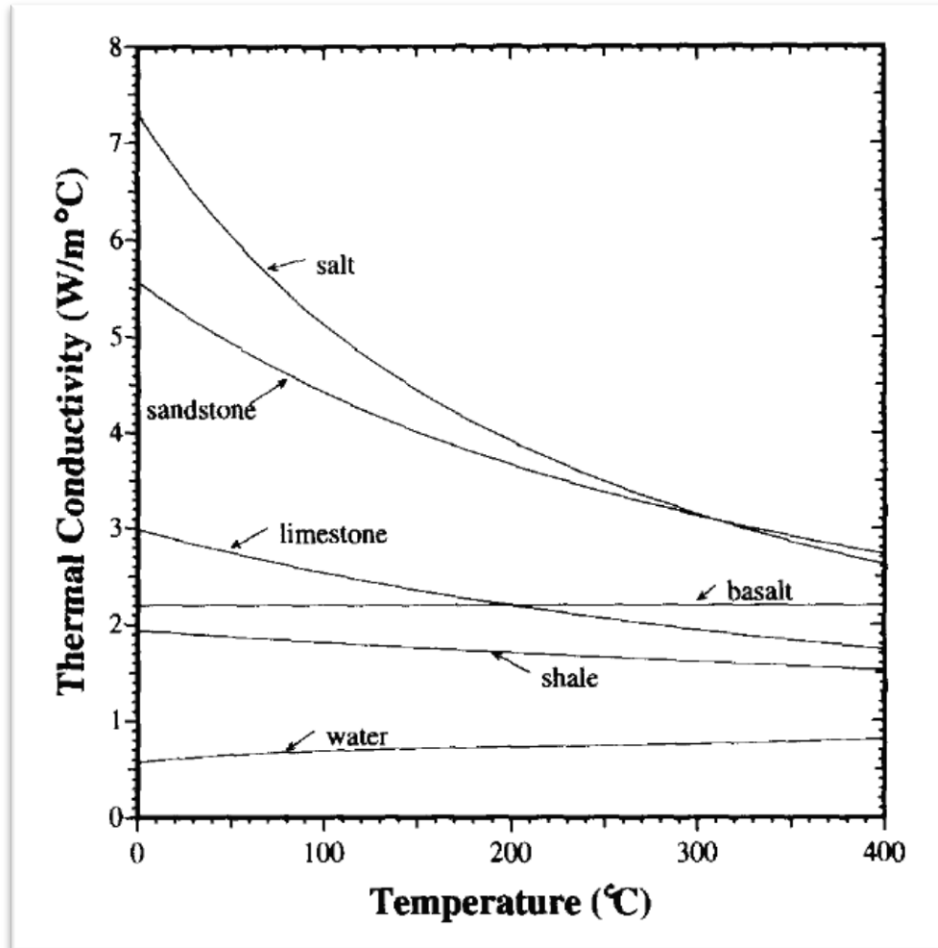
Activist for the release of John Downs from prison ([www.johnwdowns.com](http://www.johnwdowns.com))

FIGURE 1



As porosity decreases, thermal conductivity increases in shales, limestones, and sandstones but salt is unaffected (Corrigan and Sweat, 1995).

FIGURE 2



As temperature increases, the thermal conductivity of sandstone, limestone, shale, and salt decrease (Robertson, 1988).

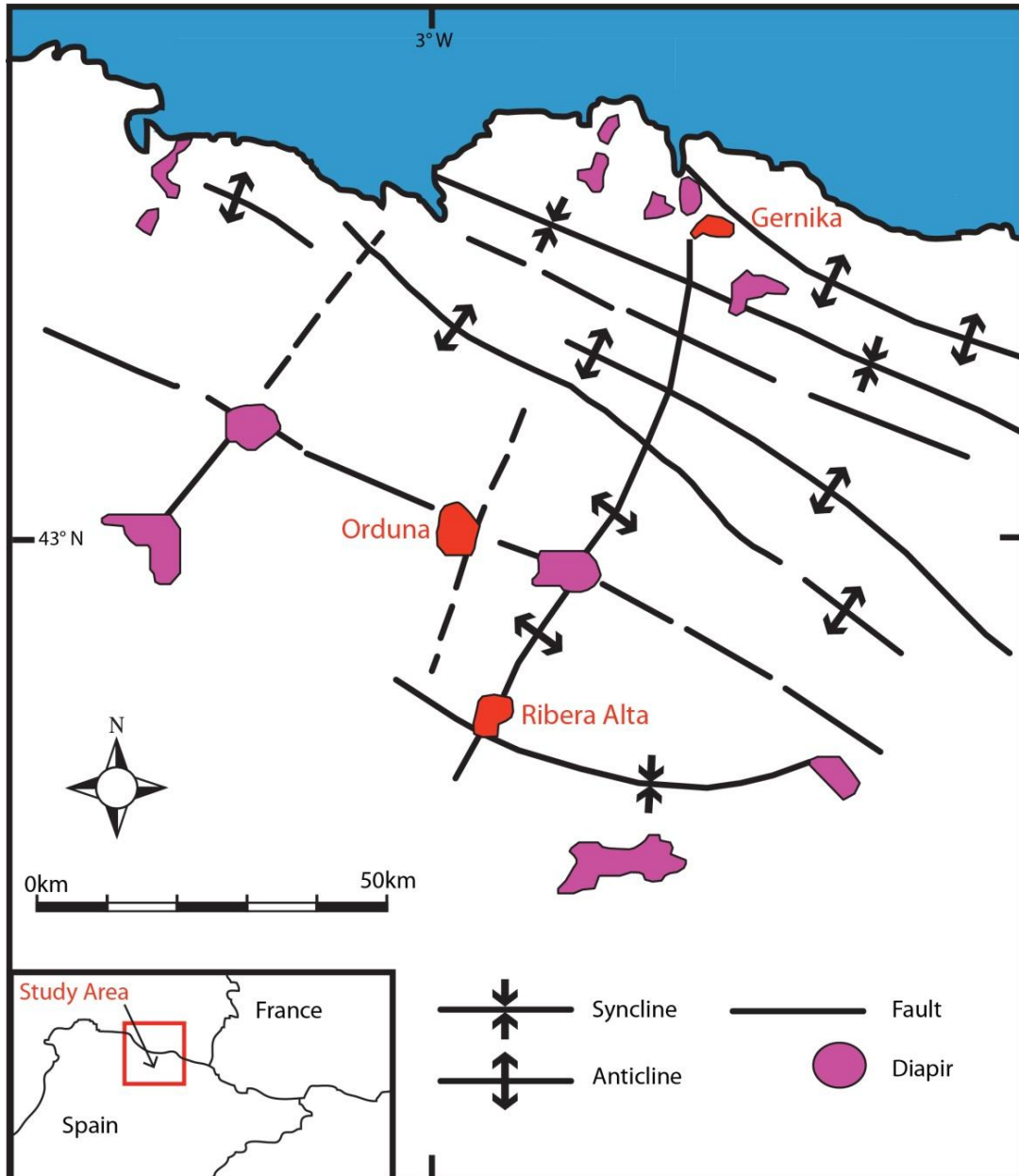


**FIGURE 3**

<b>Hypothesis</b>	<b>Location</b>
Maturity Increases as Distance Decreases	Ribera Alta Diapir & Orduna Diapir
Quartz Cementation Increases as Distance Decreases	Ribera Alta Diapir
Dimensions of Thermal Anomalies are Scale Dependent	Ribera Alta Diapir & Orduna Diapir
Sediments Above an Inclined Weld ( <u>Suprasalt</u> ) are More Mature Than Sediments Below an Inclined Weld ( <u>Subsalt</u> )	<u>Gernika</u> Salt Weld
Remote Sensing Instruments Can Measure Diapir-Related Thermal Anomalies	Ribera Alta Diapir & El Gordo Diapir (Mexico)

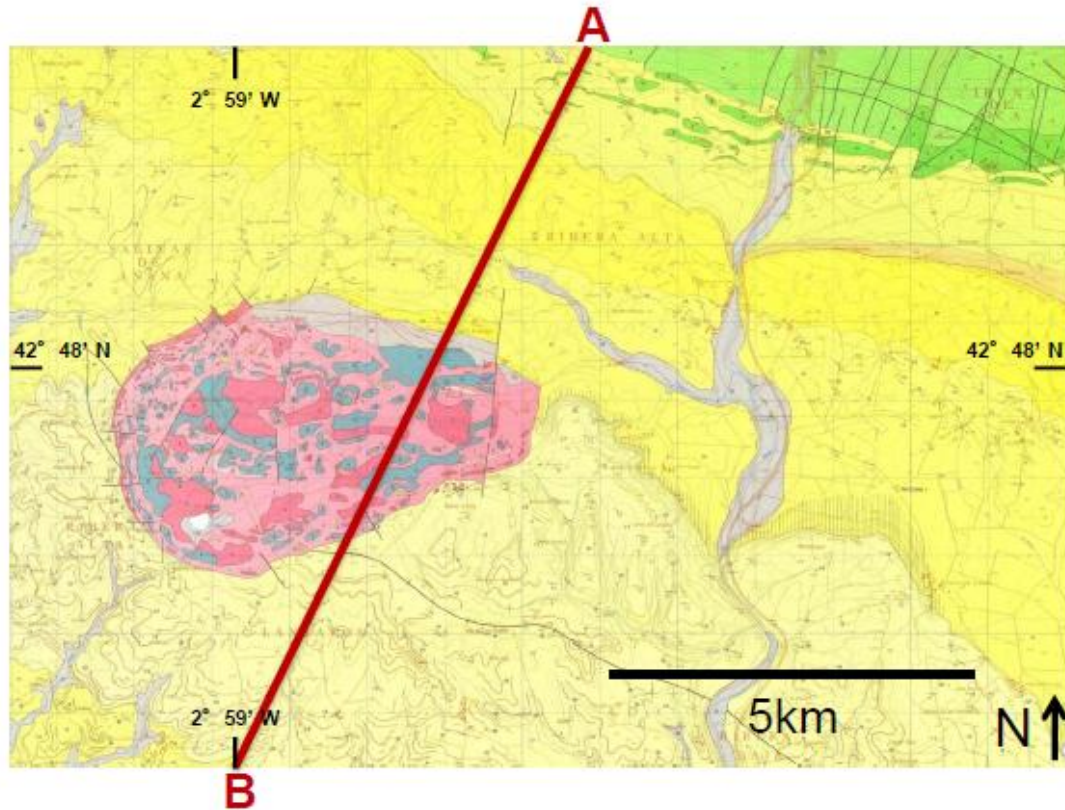
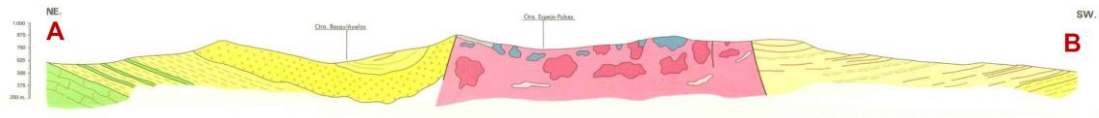
**Five hypotheses were tested at the Ribera Alta diapir, Orduna diapir, Gernika weld, and El Gordo diapir.**

FIGURE 4



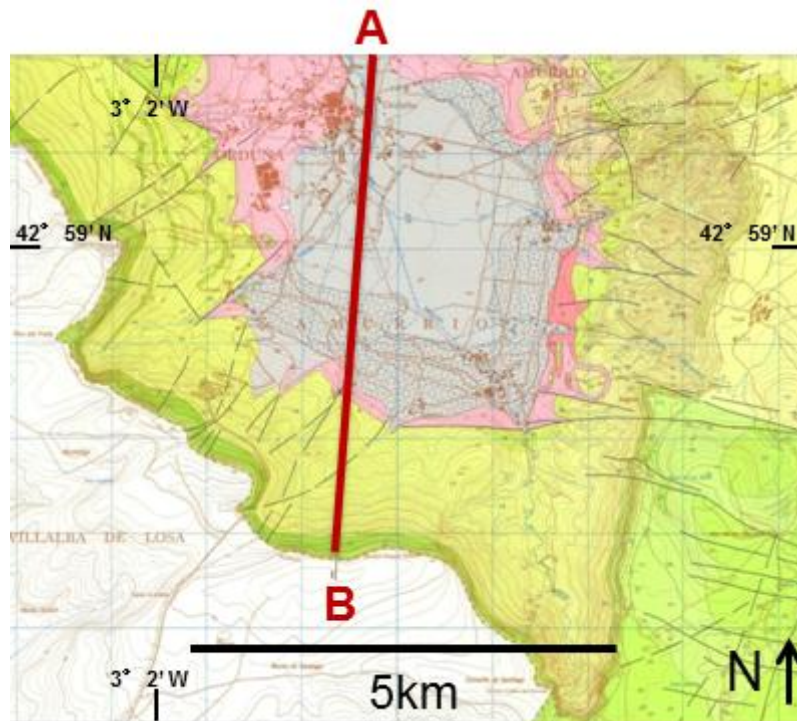
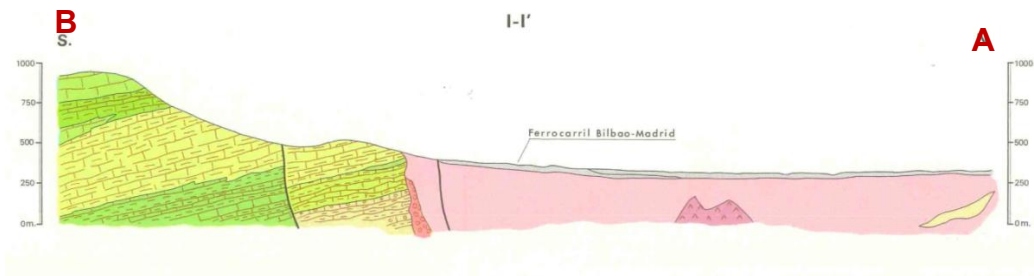
Overview of the three targeted salt structures: Ribera Alta, Orduna, and Gernika (derived from Canerot et al. (2005)).

FIGURE 5



Geological cross section of the Ribera Alta diapir (Ruiz and Jimenez, 1991).

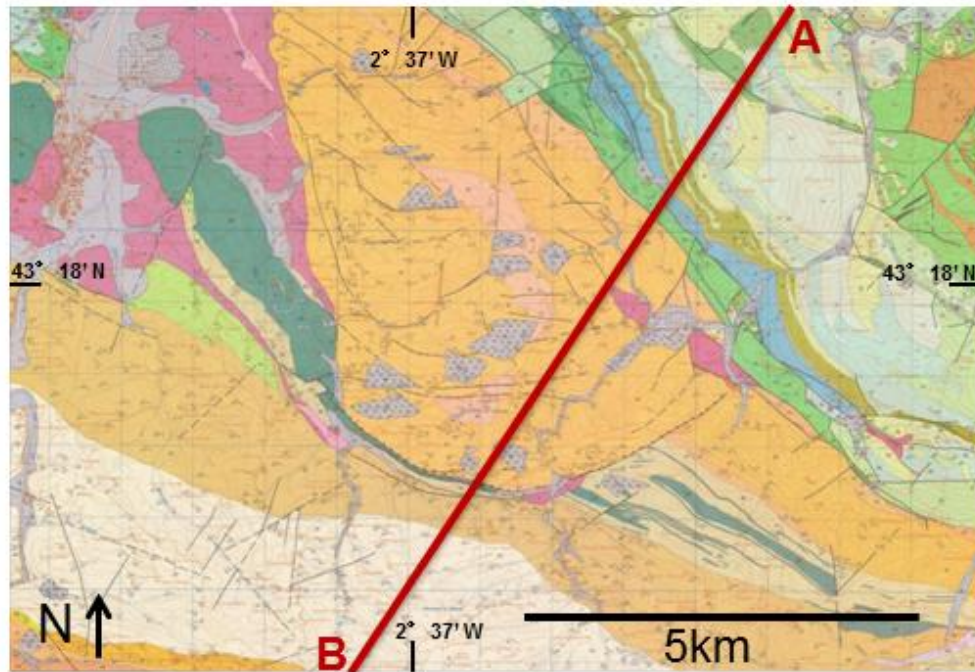
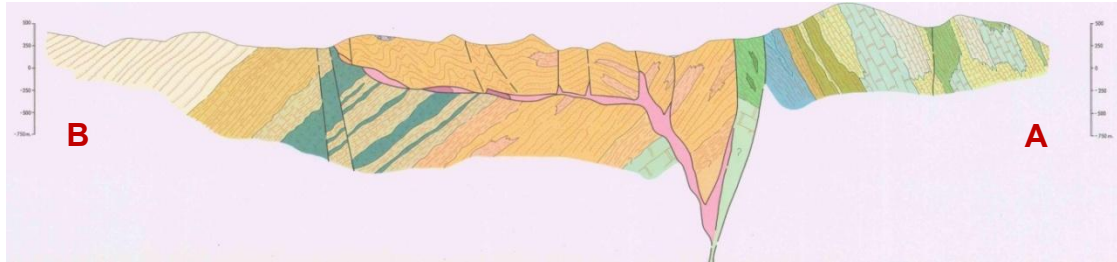
**FIGURE 6**



**Geological cross section of the Orduna diapir (Ruiz and Jimenez, 1991).**



**FIGURE 7**



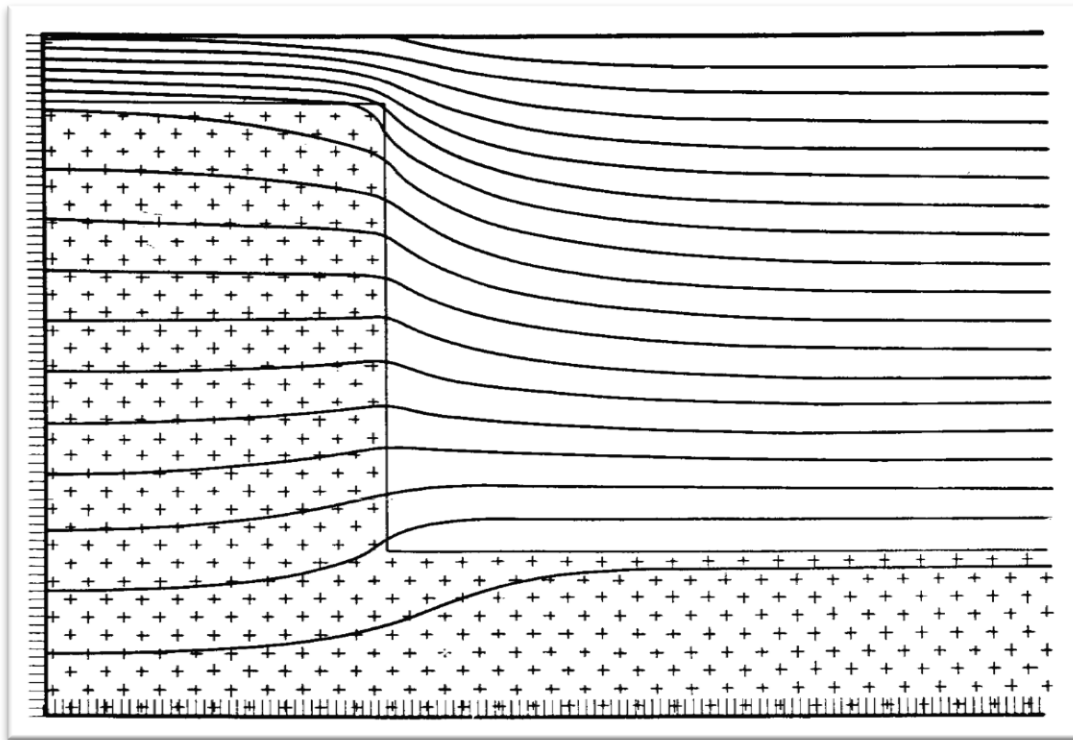
**Geological cross section of the Gernika salt weld (Ruiz and Jimenez, 1991).**

**FIGURE 8**



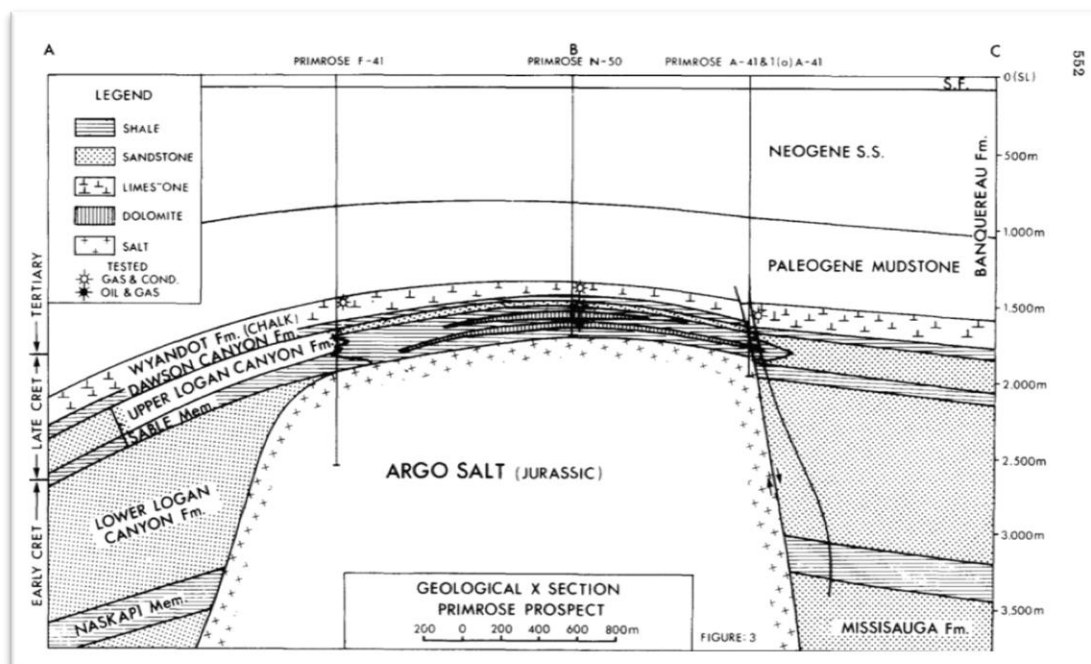
**NASA's EOS Terra satellite has a spatial resolution of ~1km/pixel and an absolute accuracy of 1K (<http://terra.nasa.gov/About/>).**

**FIGURE 9**



**Selig and Wallick (1966) modeled that the geothermal gradient above a connected dome is approximately twice as large as over normal sediments. Friction caused by the migrating diapir results in temperature maxima occurring at the salt-sediment interface at certain depths.**

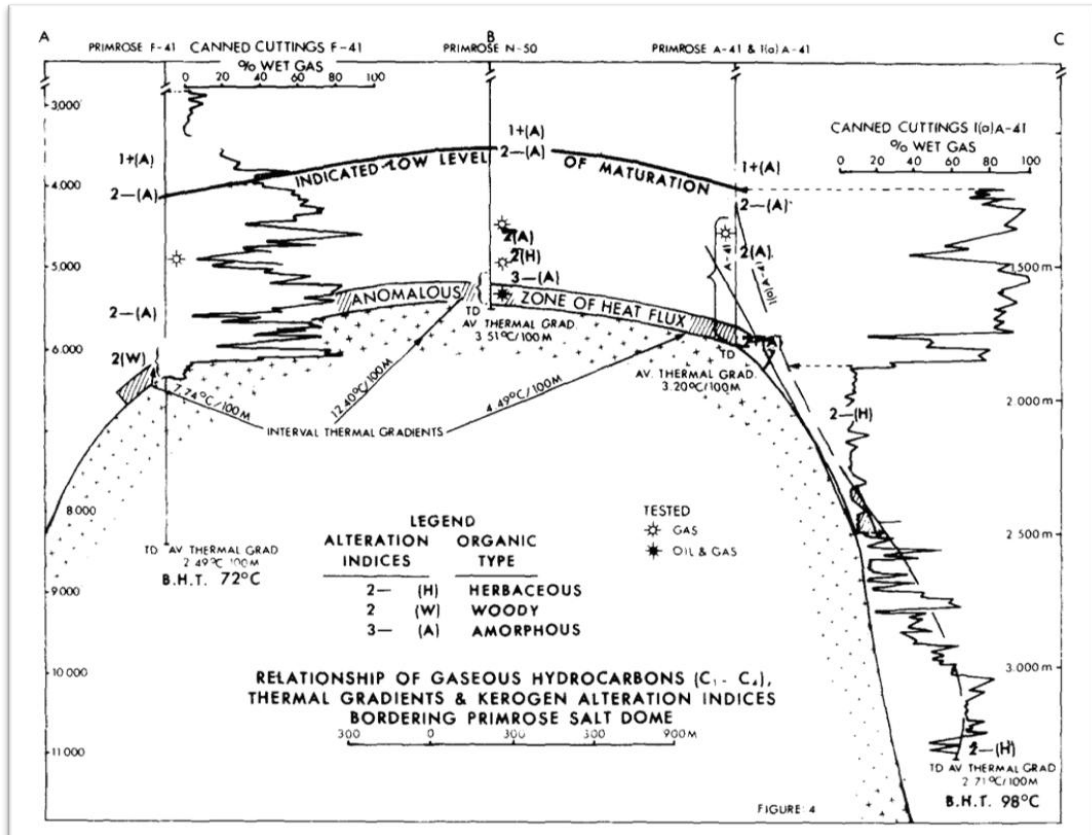
**FIGURE 10**



**Geological cross section of the Primrose salt dome, Nova Scotia. Bottom hole temperatures were recorded in the three wells shown and carbon isotopes were measured on oil and gas recovered from these wells (Rashid and McAlary, 1977).**

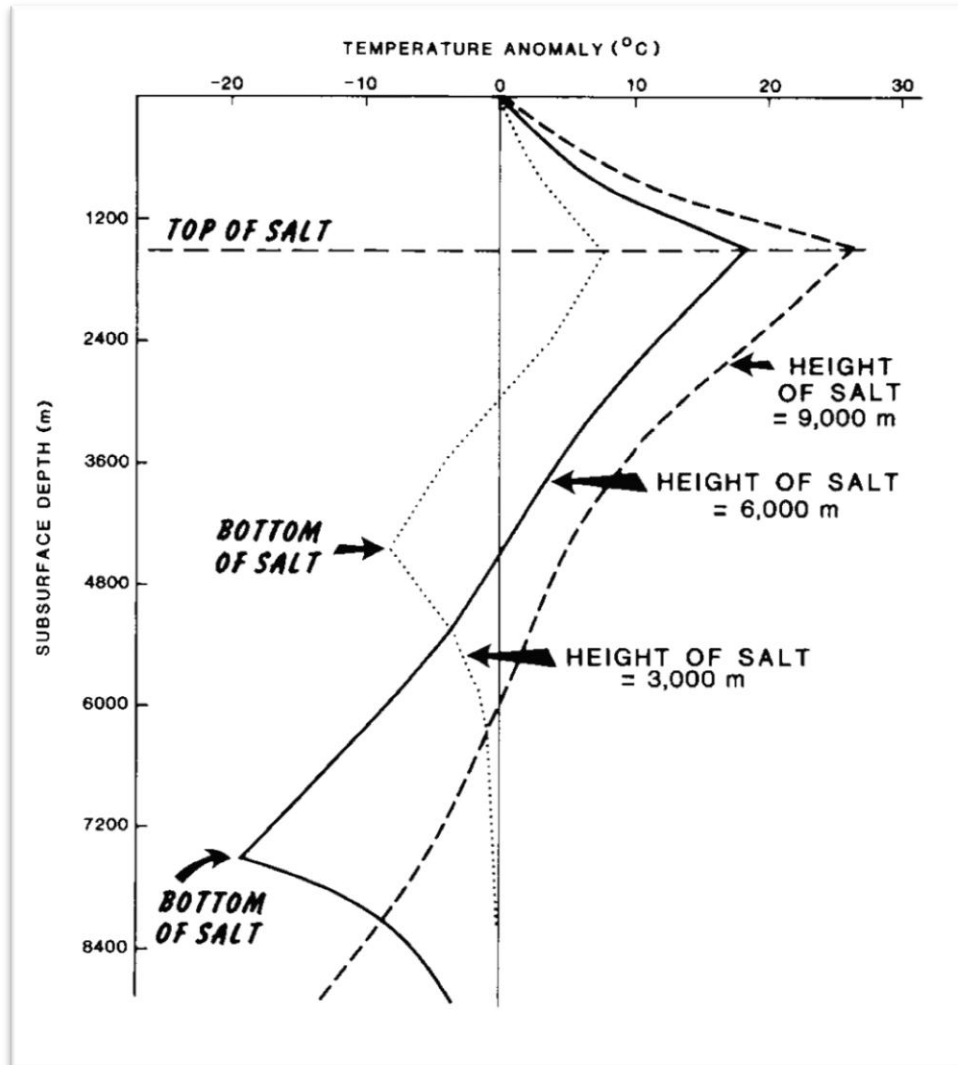


FIGURE 11



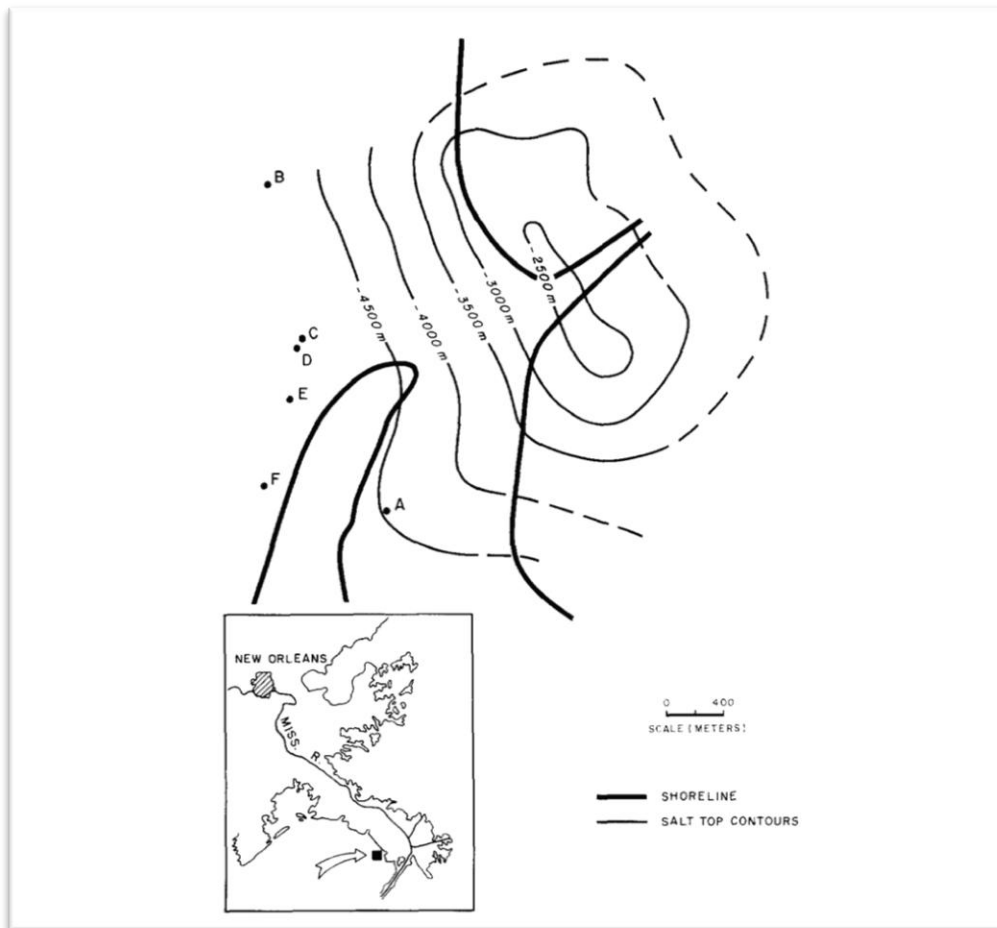
Thermal gradients, kerogen alteration indices, and occurrence of gaseous hydrocarbons for three wells on the Primrose salt dome, offshore Nova Scotia (Rashid and McAlary, 1977)

FIGURE 12



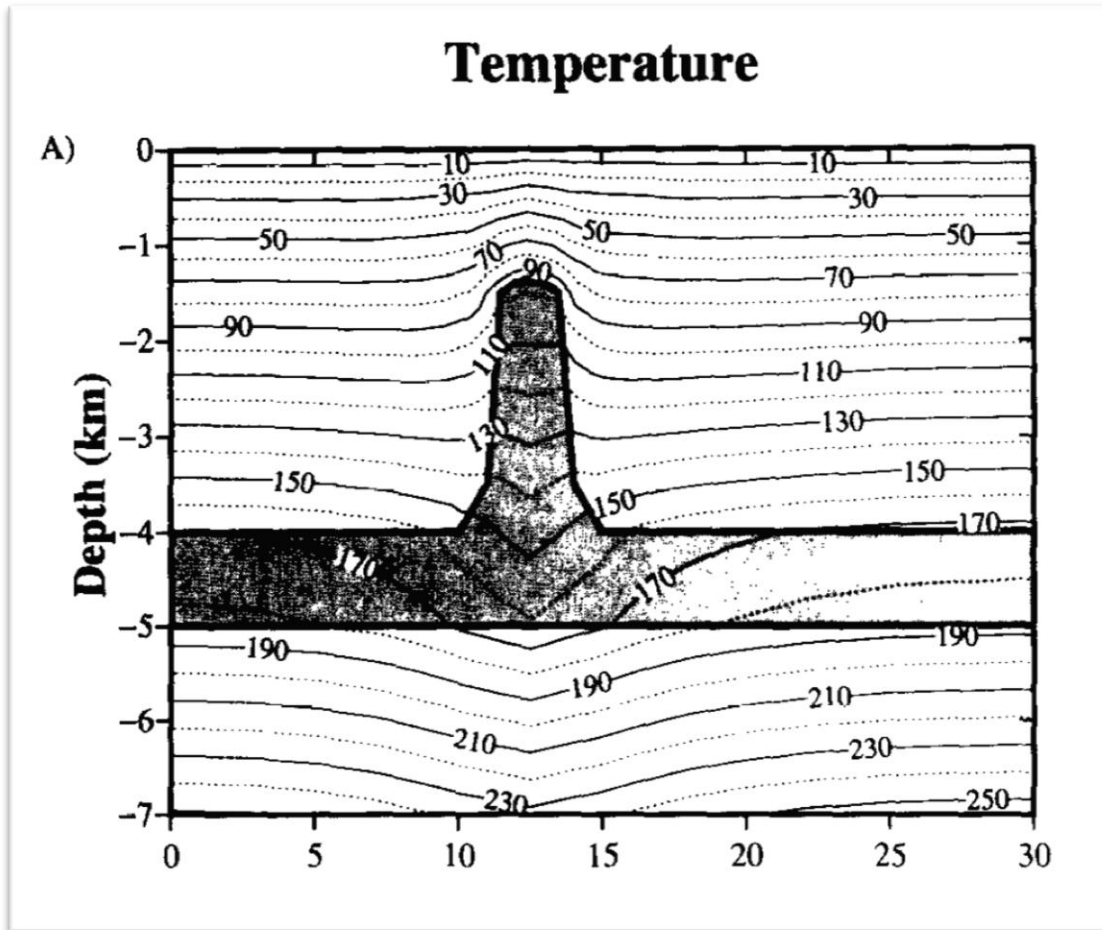
Modeled dependence of the size of the thermal anomaly on the height of a salt dome (O'Brien and Lerche, 1984).

**FIGURE 13**



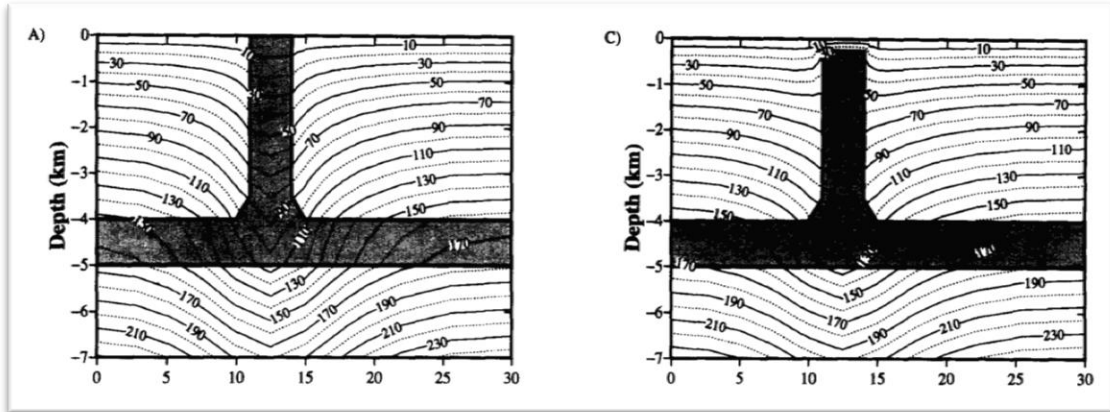
**Location of 6 wells along the flank of a West Bay salt dome, Louisiana. All wells are within one radius of the salt diapir. (Vizgirda et al., 1985)**

FIGURE 14



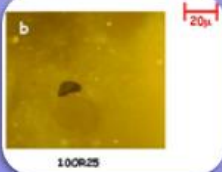
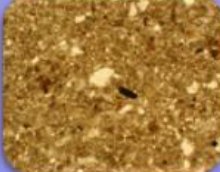
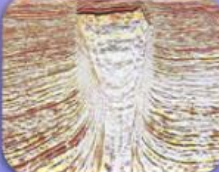
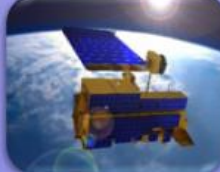
As modeled by Mello et al. (1995), there is a positive thermal anomaly above a salt dome, and a weaker, broader negative thermal anomaly below the salt dome.

**FIGURE 15**



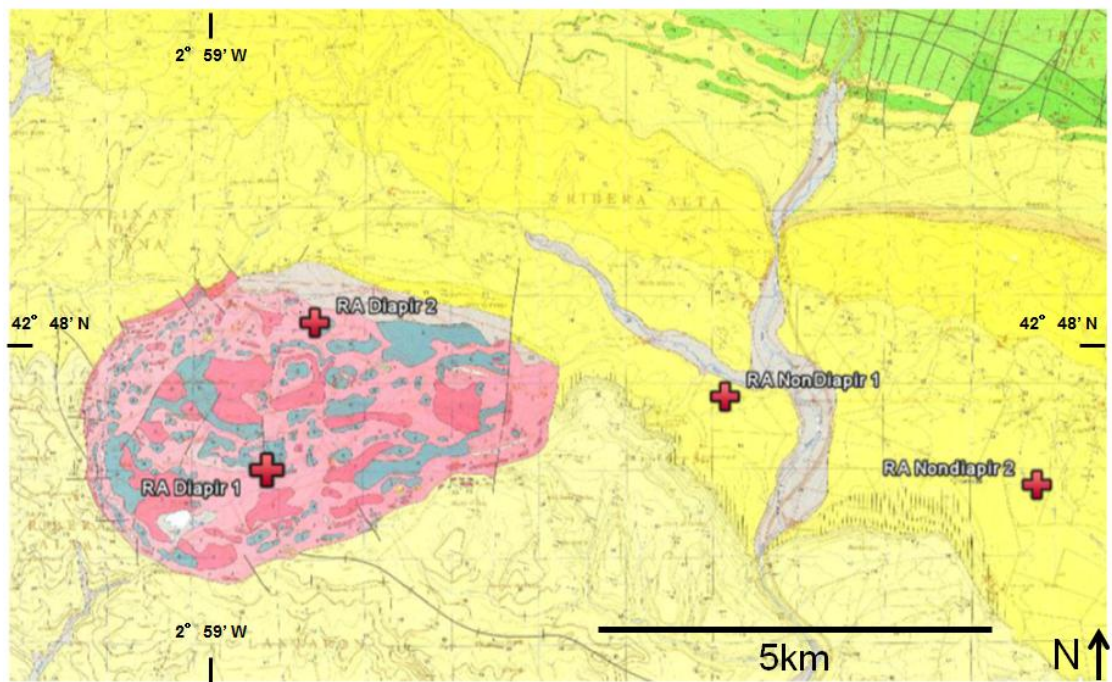
As modeled by Mello et al., 1995, a diapir that is exposed at the surface has a monopolar temperature anomaly, but a buried diapir has a dipolar temperature anomaly.

**FIGURE 16**

Vitrinite Reflectance	Quartz Cementation	Seismic Interpretation	Remote Sensing
			
<ul style="list-style-type: none"> <li>• Woody Plant Material</li> </ul>	<ul style="list-style-type: none"> <li>• <u>Intergranular SiO<sub>2</sub> Cement</u></li> </ul>	<ul style="list-style-type: none"> <li>• 2D Seismic Survey</li> </ul>	<ul style="list-style-type: none"> <li>• EOS Terra Satellite</li> <li>• MODIS Instrument</li> </ul>
<ul style="list-style-type: none"> <li>• 45 Samples Analyzed by <u>Egsploration Co.</u></li> </ul>	<ul style="list-style-type: none"> <li>• 8 Samples Cut to Thin Section and Analyzed</li> </ul>	<ul style="list-style-type: none"> <li>• 1 Survey &amp; 2 Well Logs</li> </ul>	<ul style="list-style-type: none"> <li>• 1 km/pixel</li> <li>• 5 Years of 8-Day Data Collected</li> </ul>
<ul style="list-style-type: none"> <li>• Primary Maturity Indicator</li> </ul>	<ul style="list-style-type: none"> <li>• Secondary Maturity Indicator</li> </ul>	<ul style="list-style-type: none"> <li>• Subsurface Orientation</li> </ul>	<ul style="list-style-type: none"> <li>• Modern Heat Flow</li> </ul>

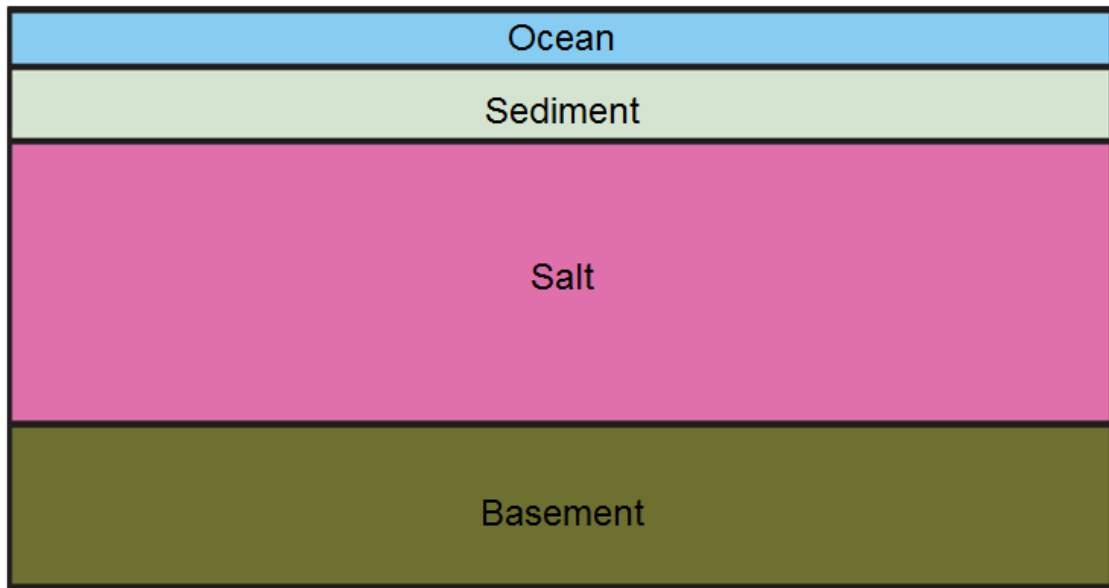
**Methodologies used to measure maturities and modern day heat flow.**

**FIGURE 17**



**Ribera Alta diapir remote sensing locations plotted on a geological map from Ruiz and Jimenez (1991).**

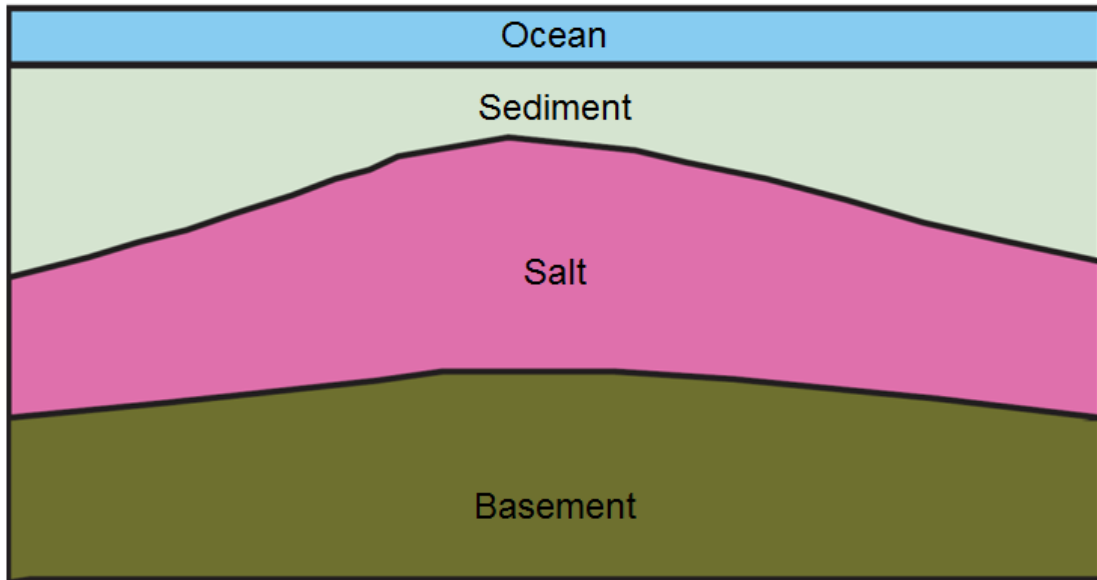
**FIGURE 18**



**Keuper evaporites were deposited in the late Triassic (200 Ma).**

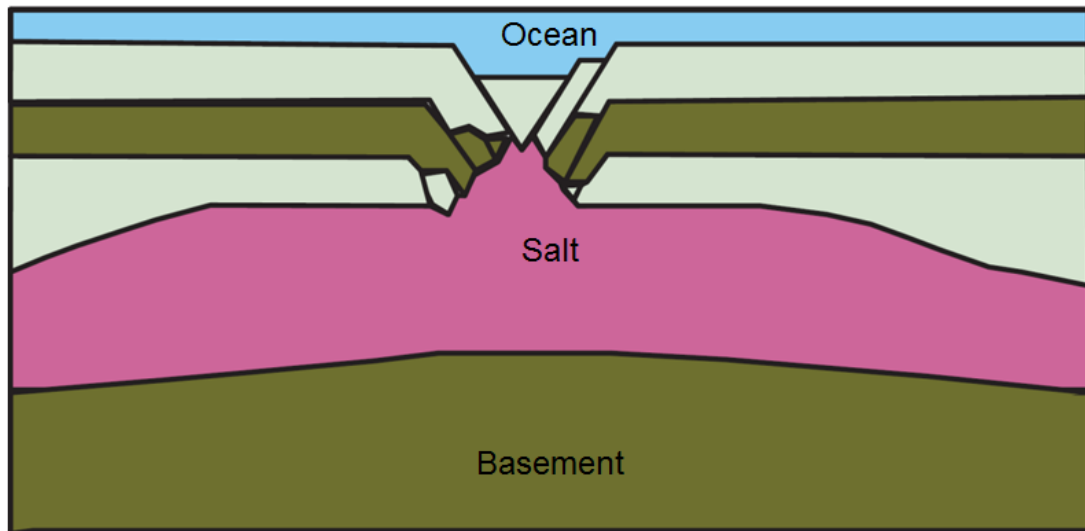


**FIGURE 19**



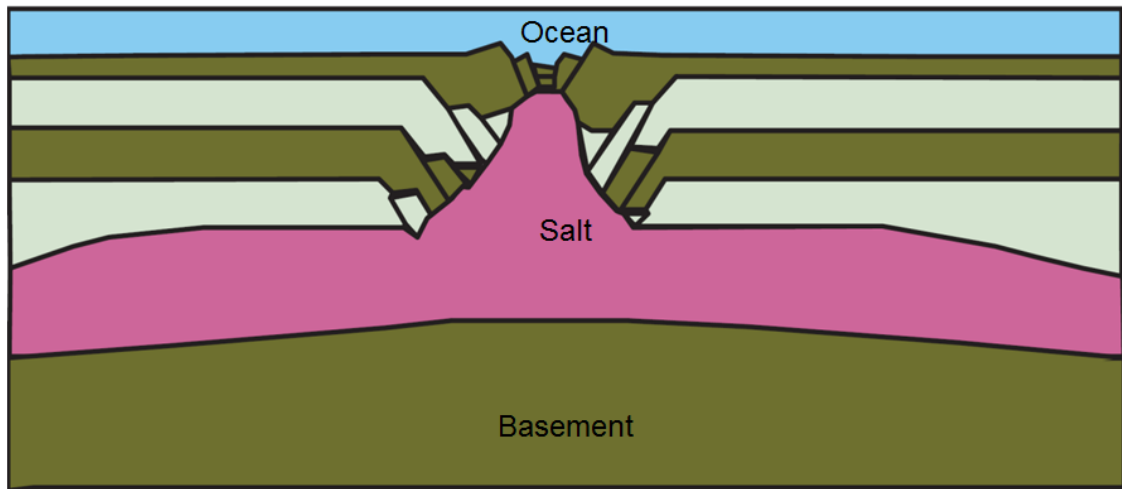
**Salt anticlines formed in the late Jurassic (150Ma).**

**FIGURE 20**



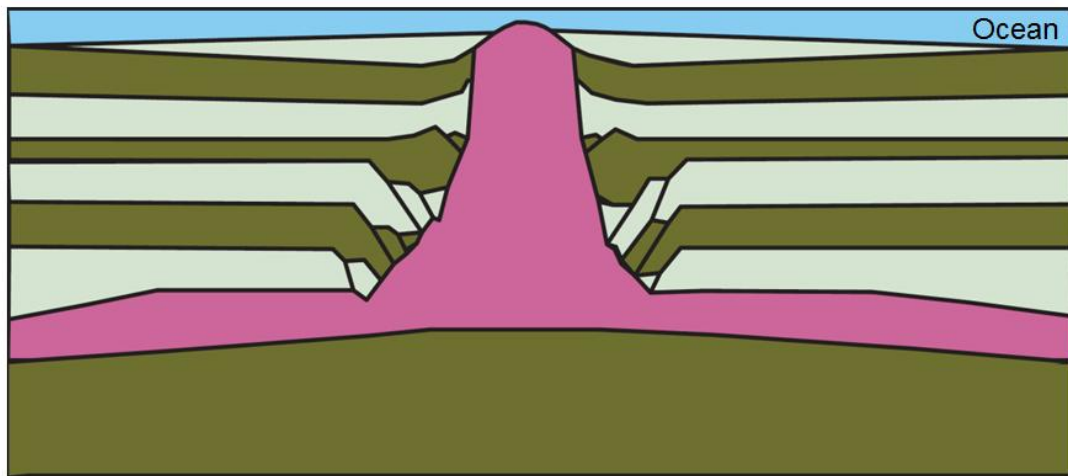
**Reactive diapirism began in the early Aptian (125Ma).**

**FIGURE 21**



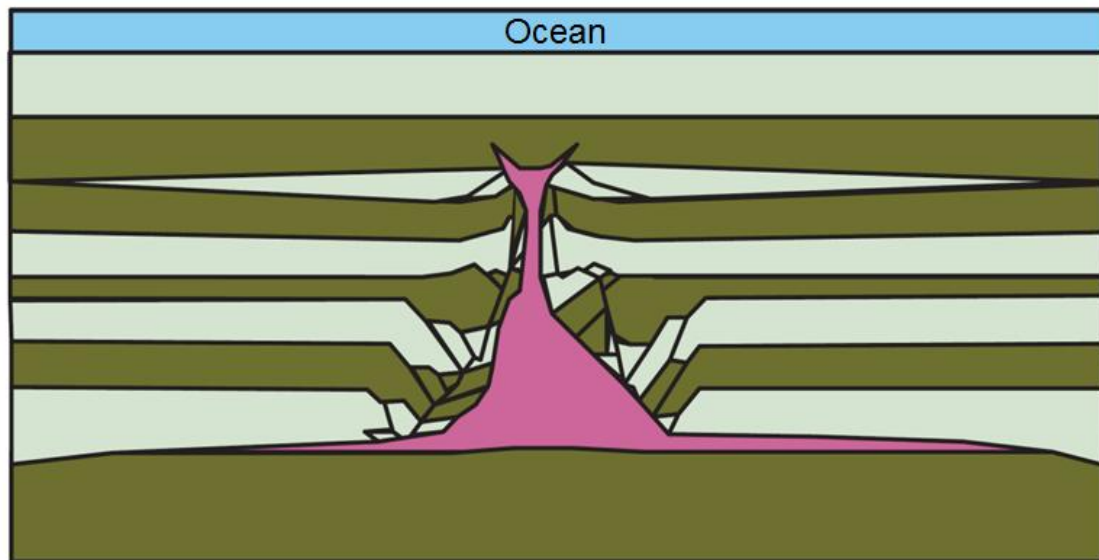
**Active diapirism began in the late Aptian (115 Ma).**

**FIGURE 22**



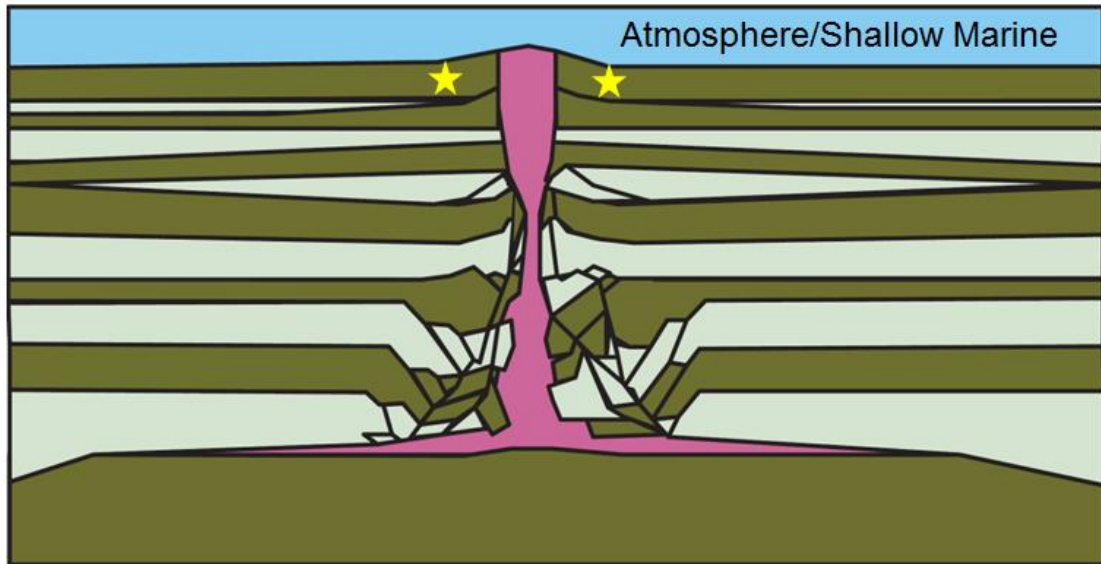
**Passive diapirism continued from the late Aptian (115Ma) to the late Cenomanian (80 Ma).**

**FIGURE 23**



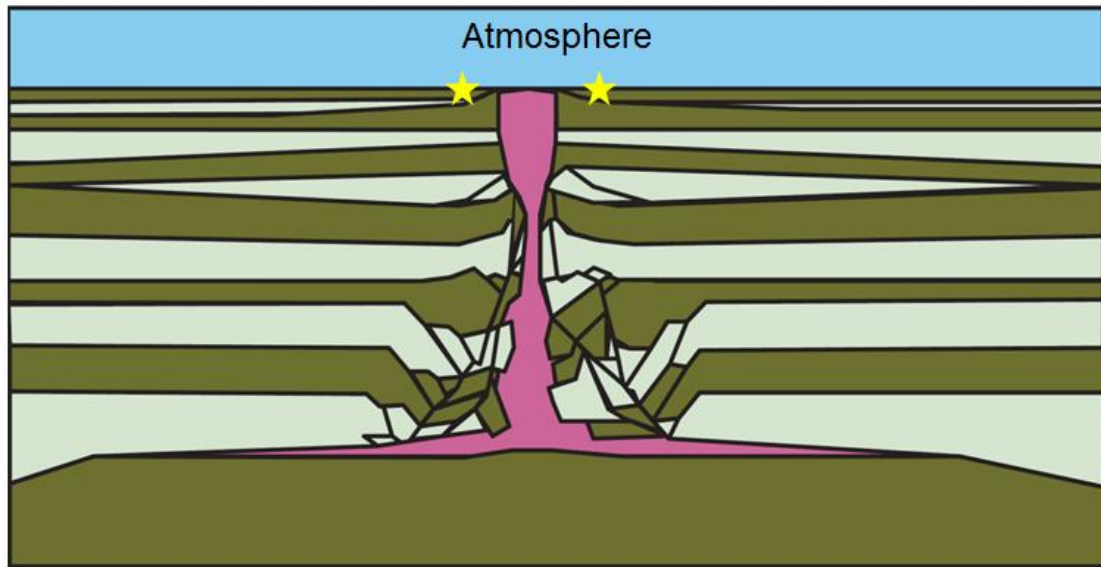
**Diapirs exhausted the majority of their salt supply and were buried from the late Campanian (80Ma) to the late Oligocene (35 Ma)**

**FIGURE 24**



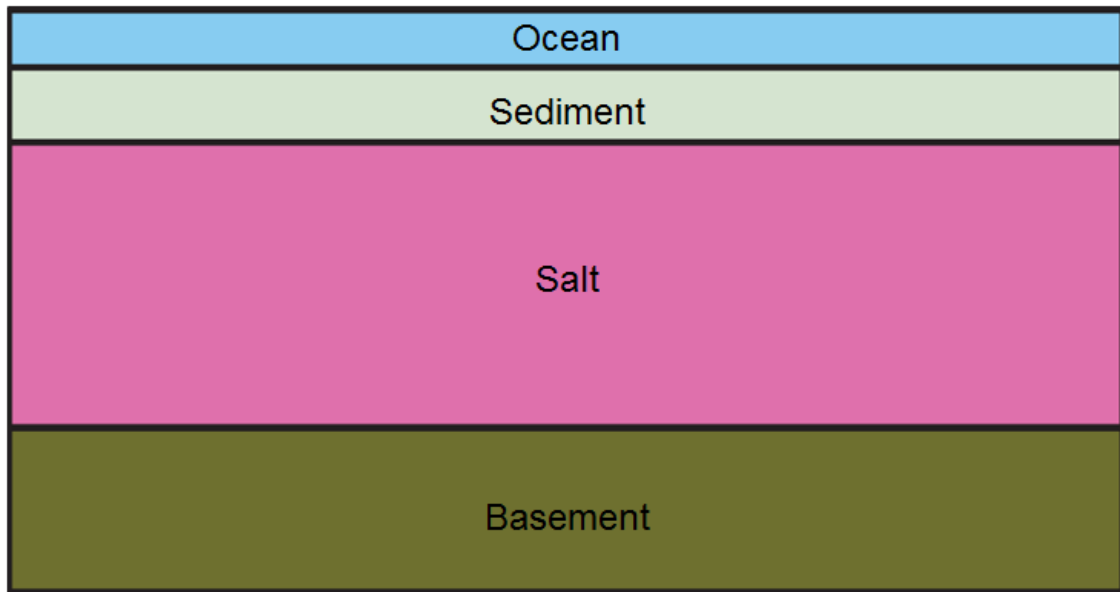
**From the late Oligocene (35 Ma) to the Pliocene (4.4 Ma) the Ribera Alta diapir was the site of deposition within the Miranda-Trevino syncline (samples represented by yellow stars).**

**FIGURE 25**



**From the Pliocene (4.4 Ma) to the present the Ribera Alta diapir has experienced erosional diapirism.**

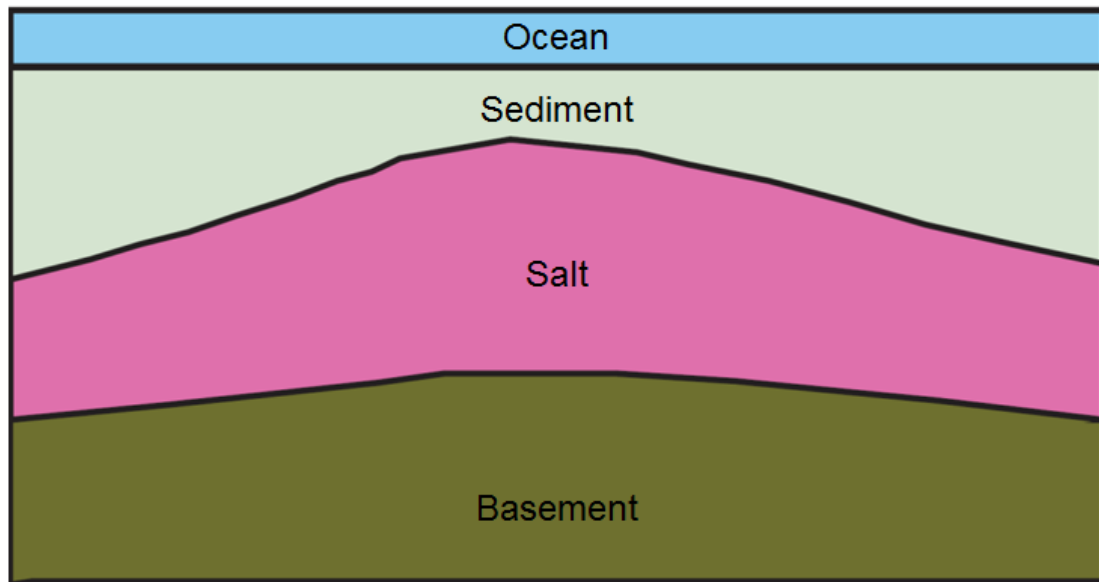
**FIGURE 26**



**Keuper evaporites were deposited in the late Triassic (200 Ma).**

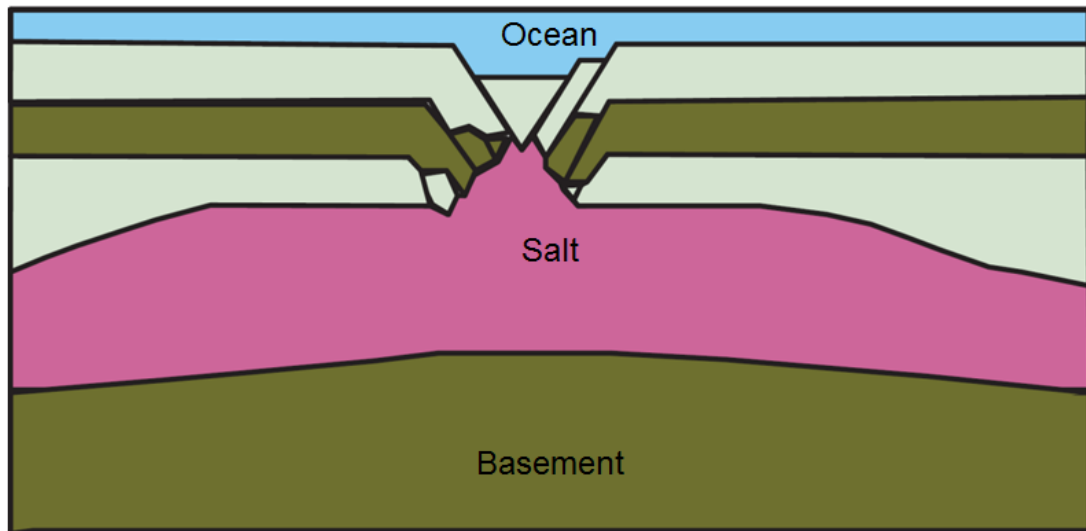


**FIGURE 27**



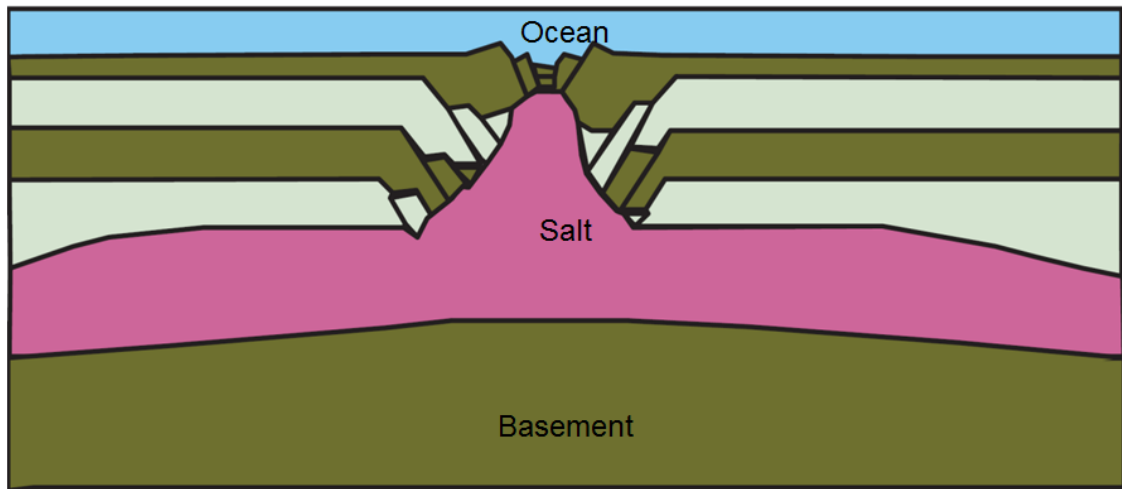
**Salt anticlines formed in the late Jurassic (150Ma).**

**FIGURE 28**



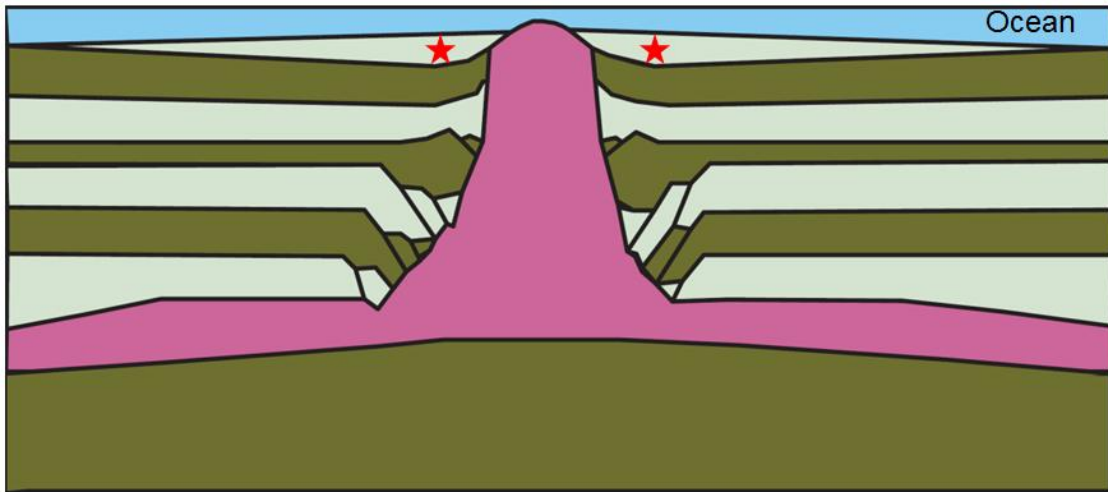
**Reactive diapirism began in the early Aptian (125Ma).**

**FIGURE 29**



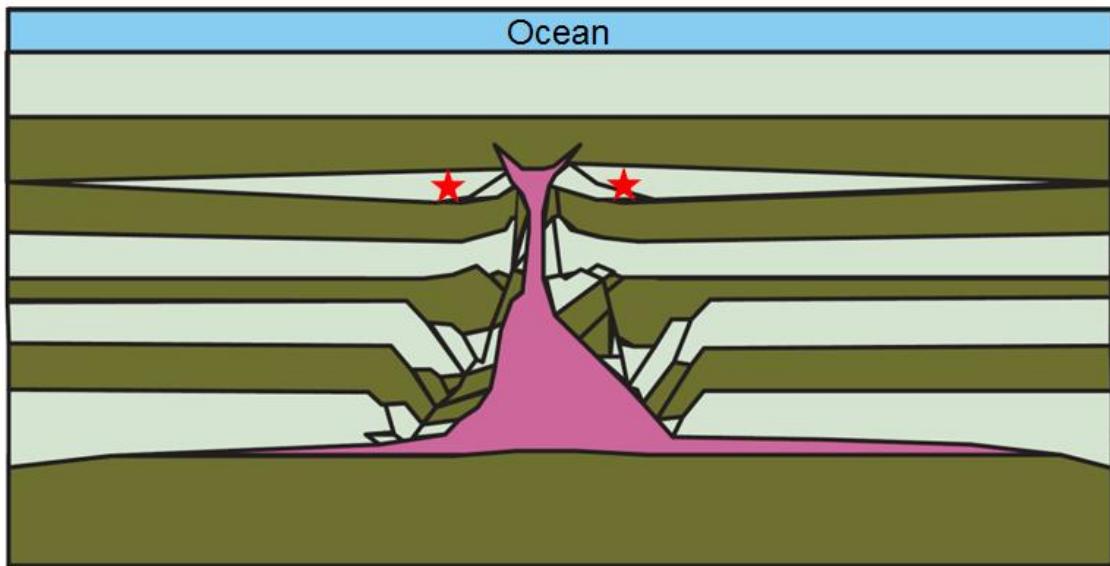
**Active diapirism began in the late Aptian (115 Ma).**

**FIGURE 30**



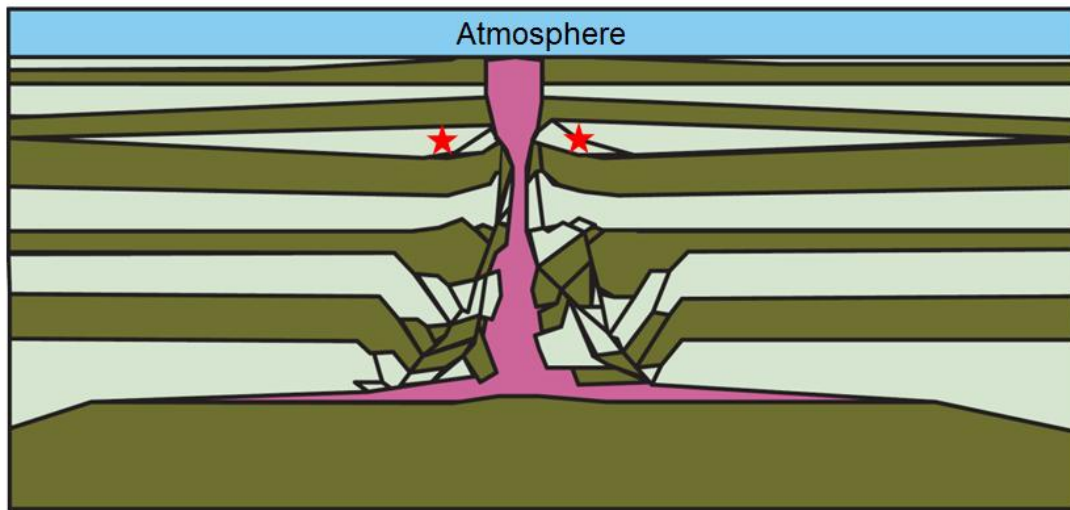
**Passive diapirism continued from the late Aptian (115Ma) to the late Campanian (80 Ma), with samples (red stars) being deposited around the Orduna diapir in the Turonian (90 Ma).**

**FIGURE 31**



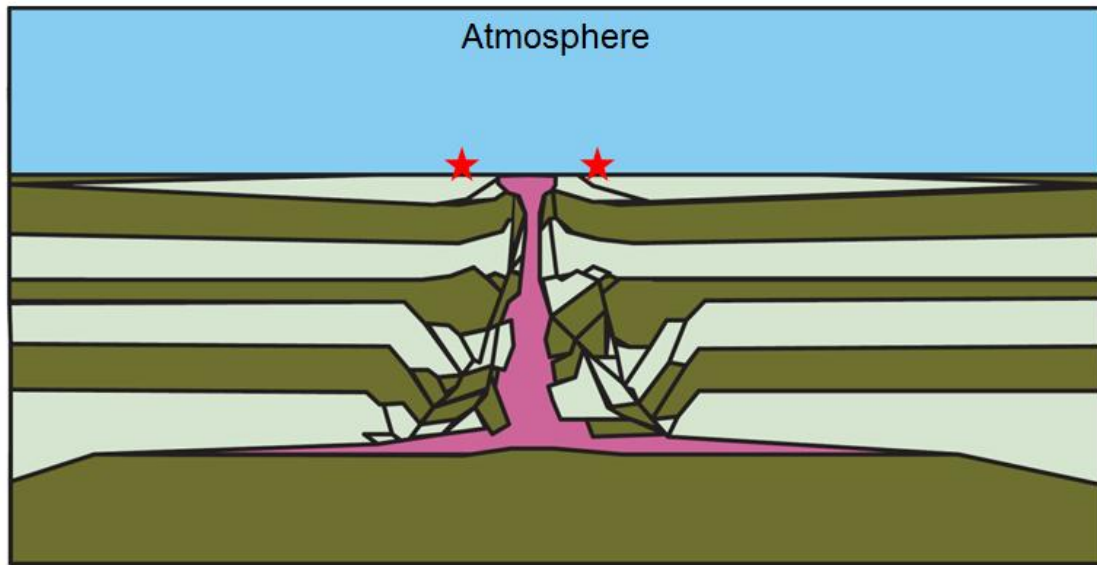
**Diapirs exhausted the majority of their salt supply and were buried from the late Campanian (80Ma) to the late Oligocene (35 Ma)**

**FIGURE 32**



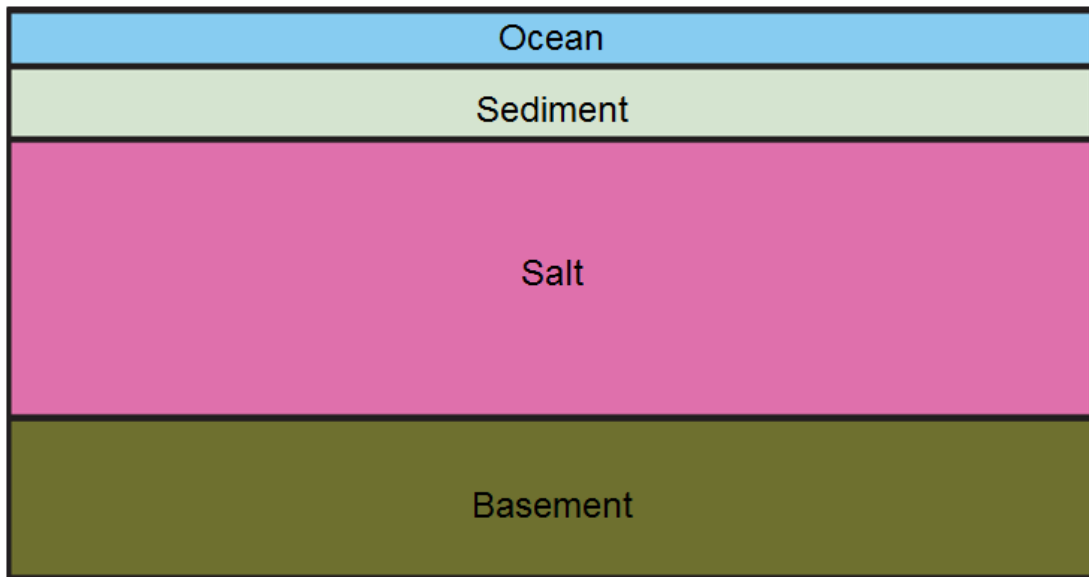
**Erosional diapirism continued from the late Oligocene (35 Ma) to the present for the Orduna diapir.**

**FIGURE 33**



**The Orduna diapir has been eroded far enough to expose surrounding Cretaceous sediments (samples represented by red stars).**

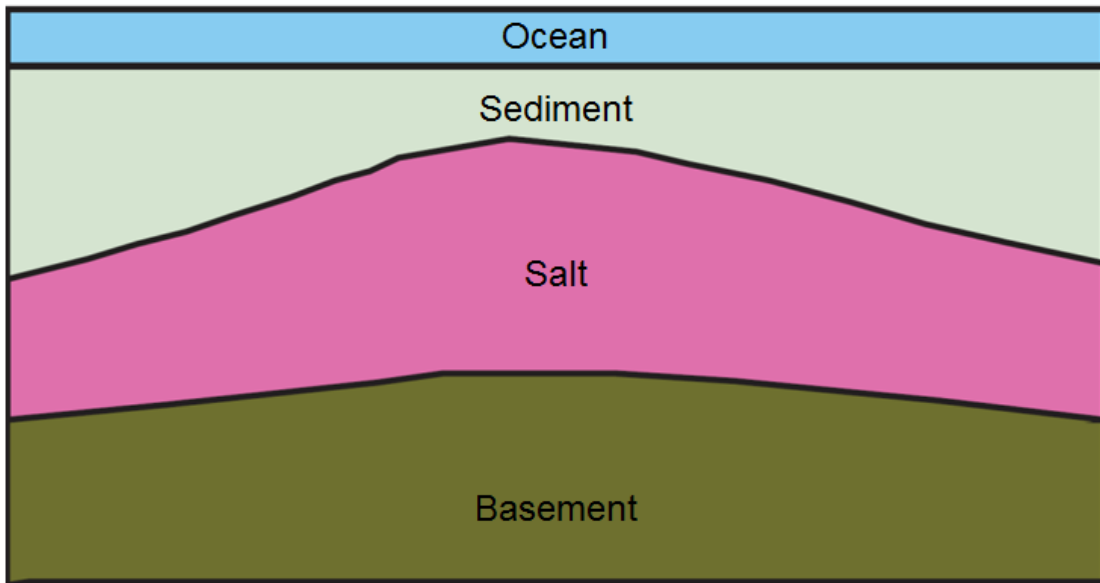
**FIGURE 34**



**Keuper evaporites were deposited in the late Triassic (200 Ma).**

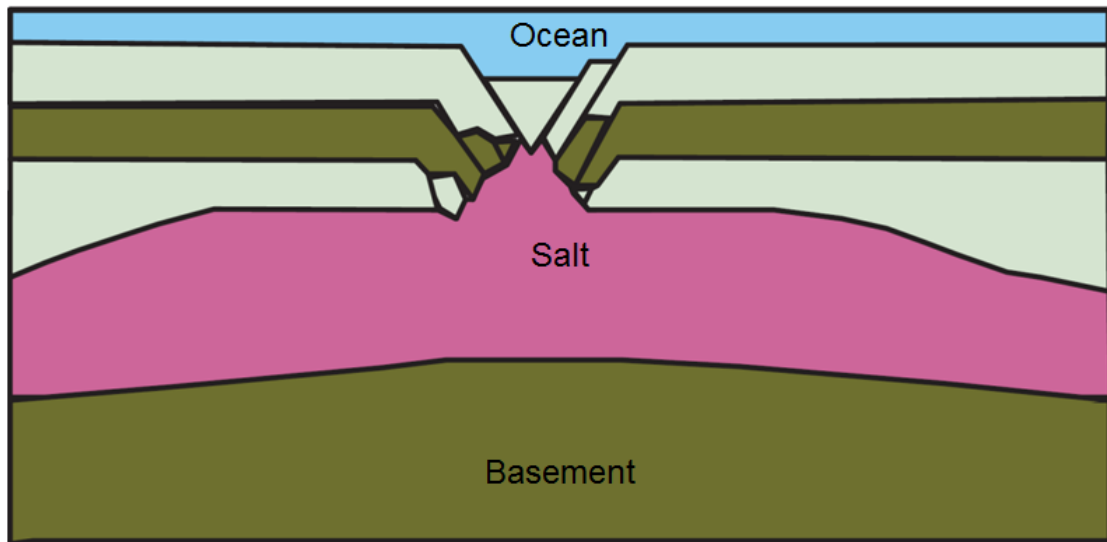


**FIGURE 35**



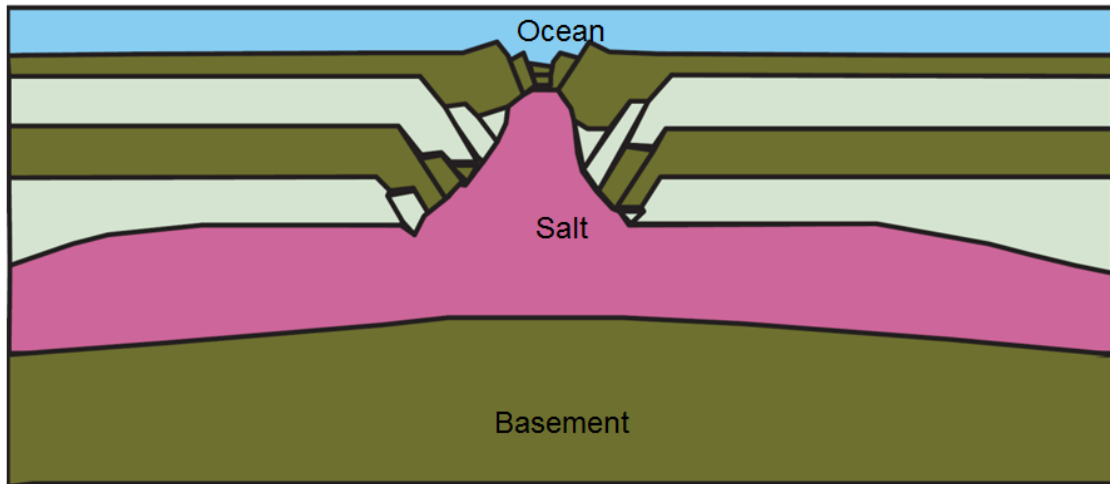
**Salt anticlines formed in the late Jurassic (150Ma).**

**FIGURE 36**



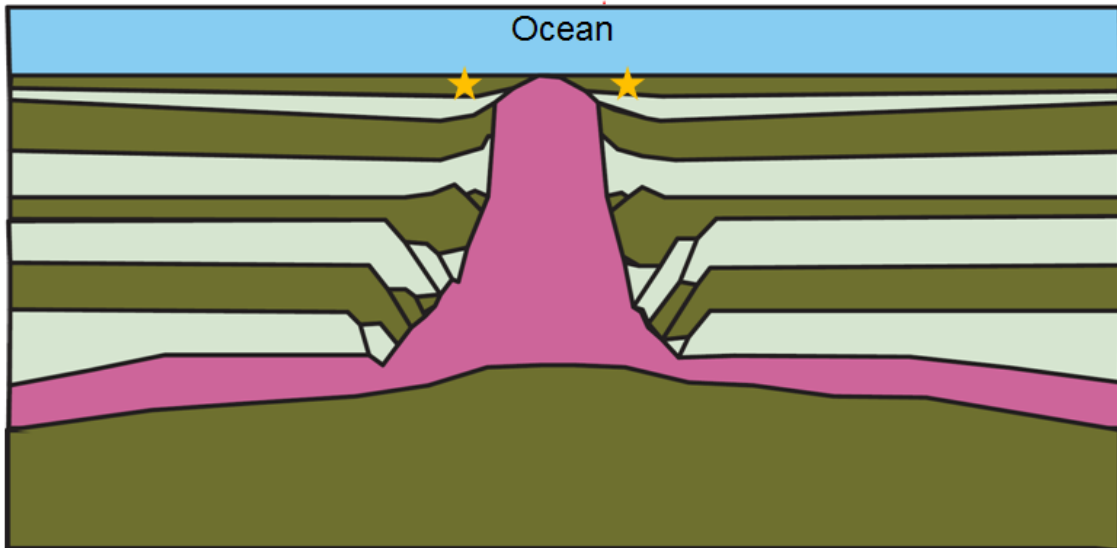
**Reactive diapirism began in the early Aptian (125Ma).**

**FIGURE 37**



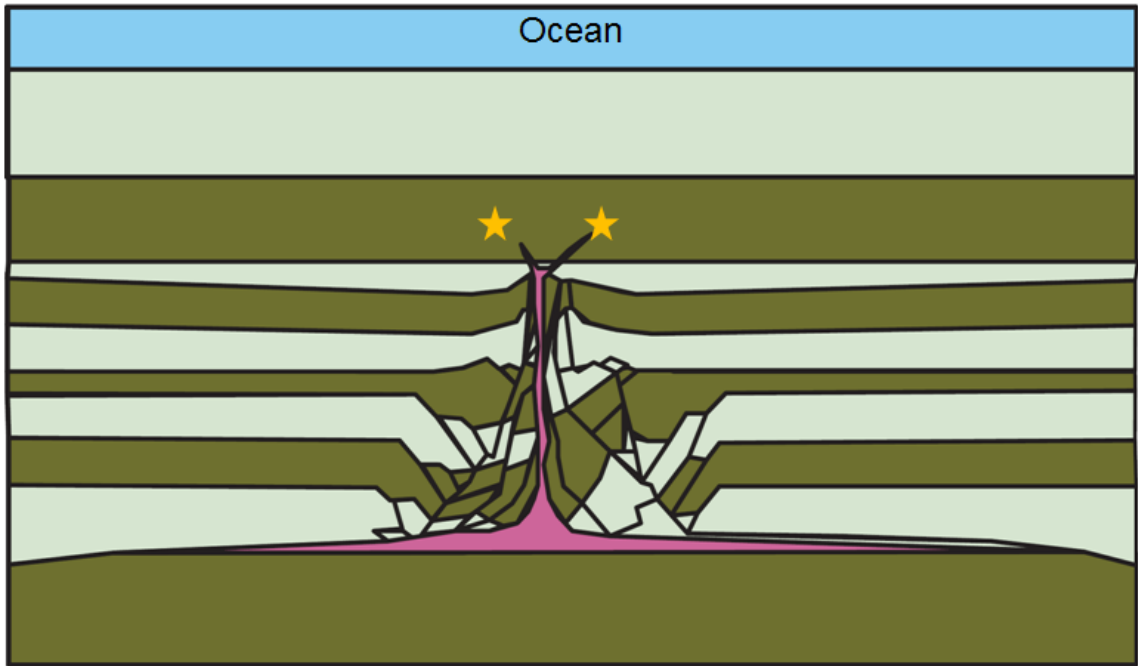
**Active diapirism began in the late Aptian (115 Ma).**

**FIGURE 38**



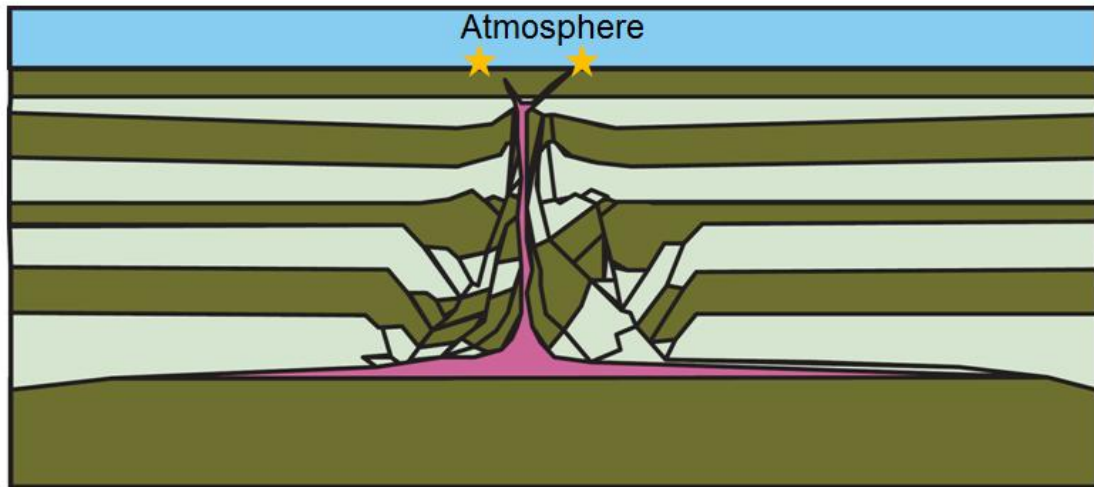
**Passive diapirism continued from the late Aptian (115Ma) to the late Campanian (80 Ma), with samples (orange stars) being deposited around the Gernika salt structure in the Albian (100 Ma).**

**FIGURE 39**



**The Gernika diapir exhausted its supply of salt, became a salt weld, and was buried from the late Campanian (80Ma) to the late Oligocene (35 Ma)**

**FIGURE 40**



**Erosional diapirism continued from the late Oligocene (35 Ma) to the present for the Gernika salt weld.**

**FIGURE 41**

			<i>Alava Block Domains</i>	
<i>Proposed intervals / Age</i>			<i>SOUTHERN</i>	<i>NORTHERN</i>
T	Oligocene		CONTINENTAL TERTIARY	
	Maast.		Puerto de Olazagutía Fm.	
UC4	Campanian		Quintanaloma Fm. Moradillo de Sedano Fm. Tubilla del Agua Fm.	Vitoria Fm.
	Santonian		San Pantaleón Member	El Atalaya Member
UC3	Coniacian		Las Losas Fm. Ribera Alta Fm.	El Zadorra Fm.
	Turonian		Valle de Mena Fm.	
UC2	Upper Cenomanian		Artzeniega Fm.	
LC2	Lower Cenomanian	SUPRA-URGONIAN COMPLEX	Utrillas Fm.	Valmaseda Fm.
	Albian		?	
LC1	Aptian	URGONIAN COMPLEX	Nograro/ Escucha Fm.	Gordexola Fm. Bilbao Fm. Galdames Fm. Areza Fm.
	Barremian-Hauterivian		Montoria Fm.	Villaro Fm.
	WEALDEN COMPLEX		?	

**Stratigraphy of the Basque-Cantabrian basin according to Arostegui et al. (2006). LC=Lower Cretaceous, UC=Upper Cretaceous, T=Tertiary**

**FIGURE 42**

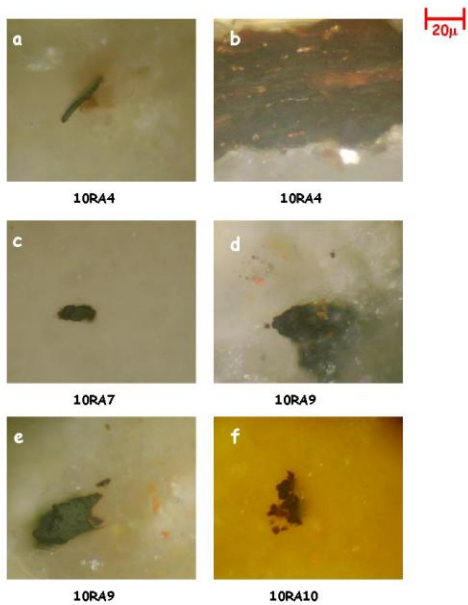


Plate 10

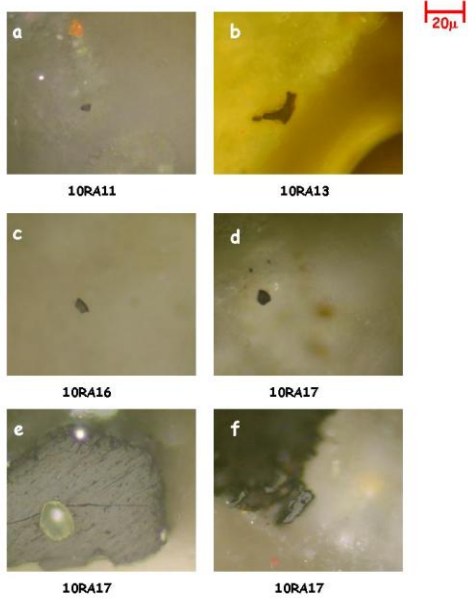
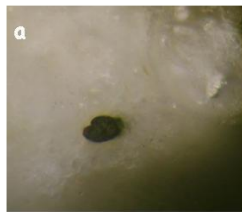


Plate 11

**Vitrinite reflectance plates for samples 10RA4-10RA17.**



**FIGURE 43**



20 $\mu$

10RA20

**Vitrinite reflectance plate for sample 10RA20.**

**FIGURE 44**

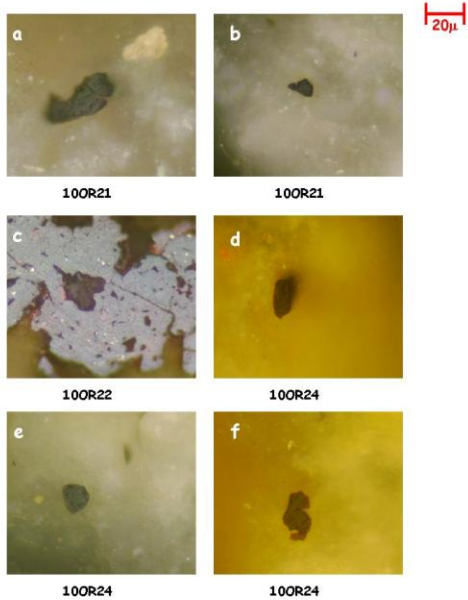


Plate 13

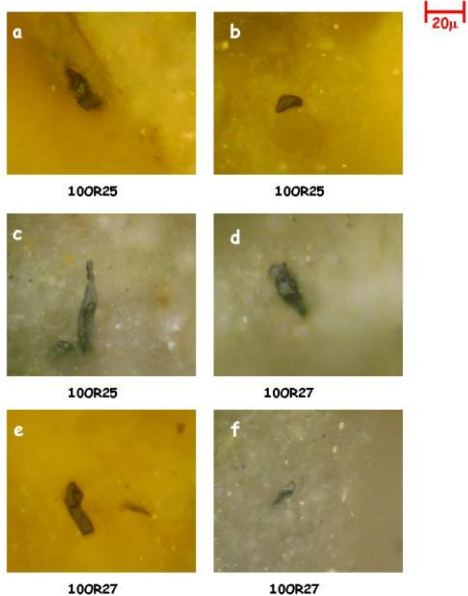


Plate 14

**Vitrinite reflectance plates for samples 100R21-100R27.**

**FIGURE 45**

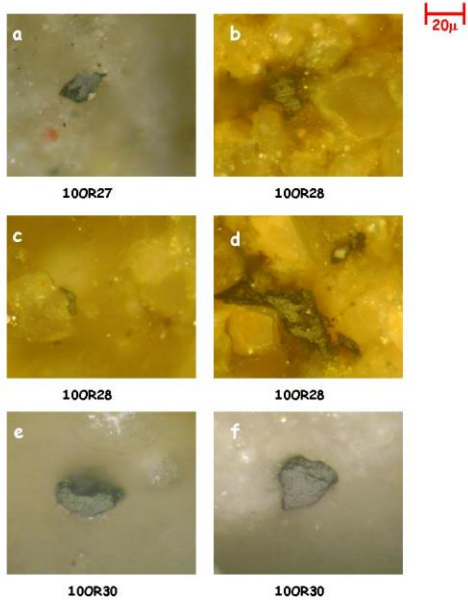


Plate 15

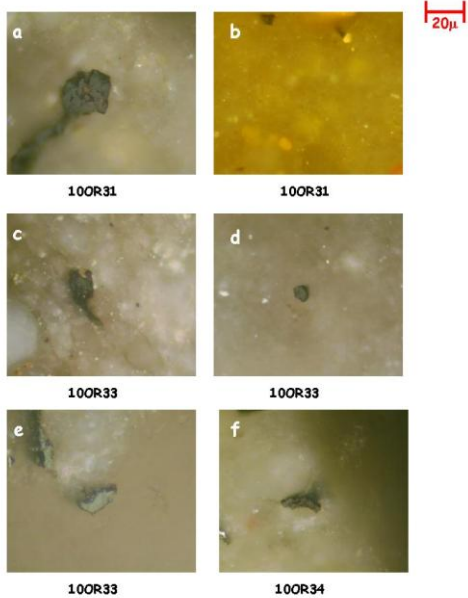
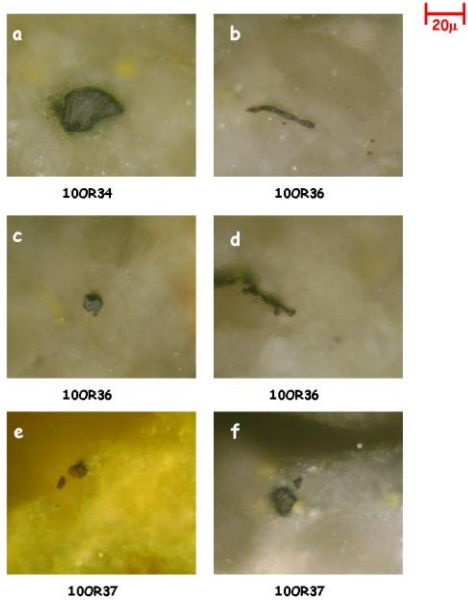


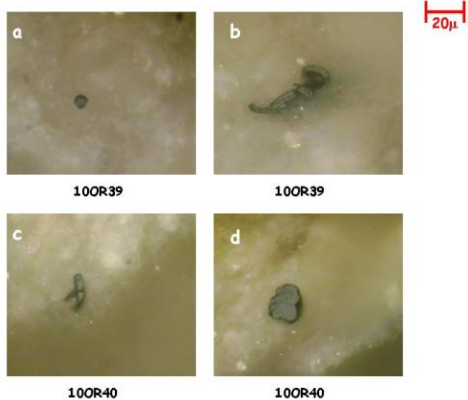
Plate 16

**Vitrinite reflectance plates for samples 100R27-100R34.**

**FIGURE 46**



**Plate 17**



**Vitrinite reflectance plates for samples 10OR34-10OR40.**

**FIGURE 47**

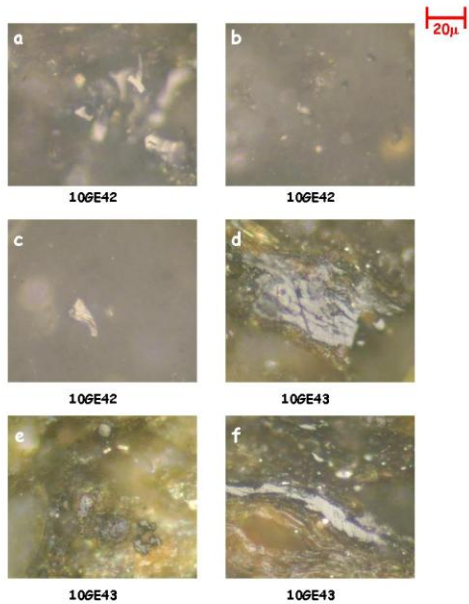


Plate 1

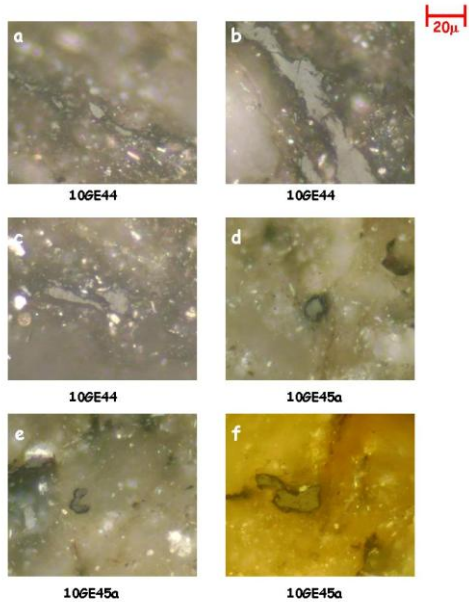


Plate 2

**Vitrinite reflectance plates for samples 10GE42-10GE45a.**

**FIGURE 48**

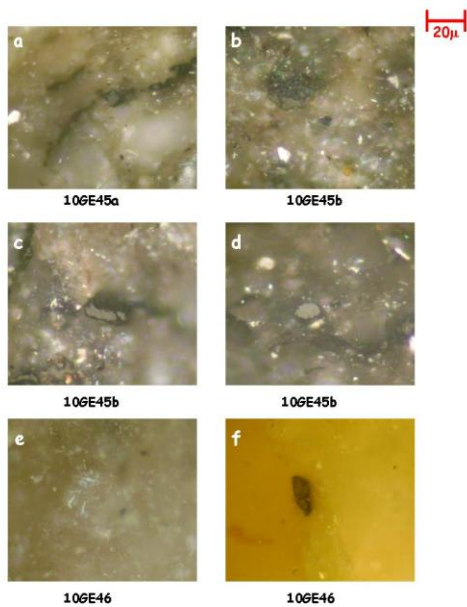


Plate 3

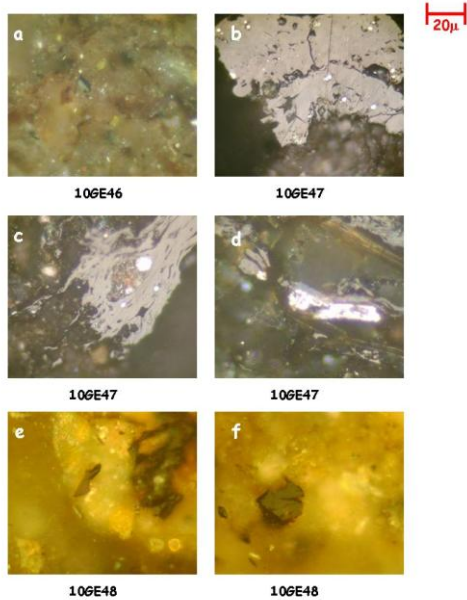
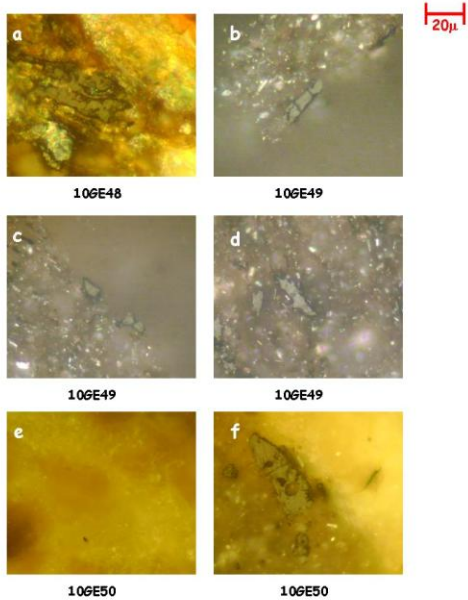


Plate 4

**Vitrinite reflectance plates for samples 10GE45a-10GE48.**

**FIGURE 49**



**Plate 5**

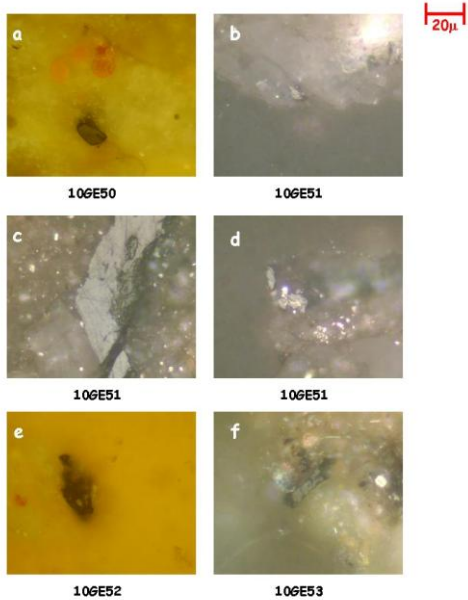


**Plate 6**

**Vitrinite reflectance plates for samples 10GE48-10GE53.**

**FIGURE 50**

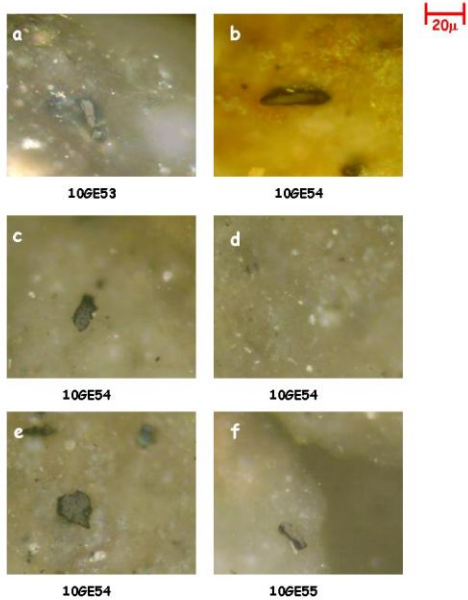


Plate 7

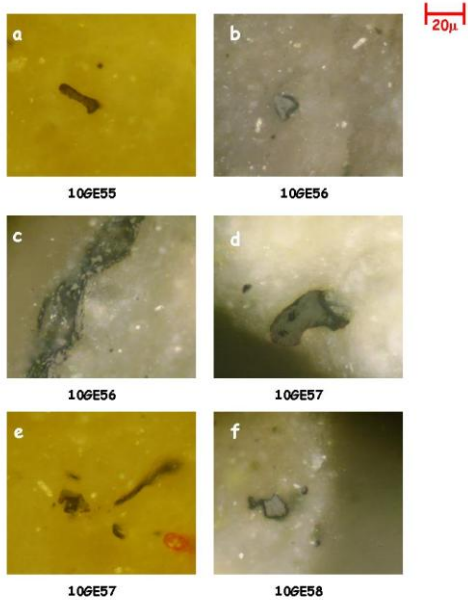
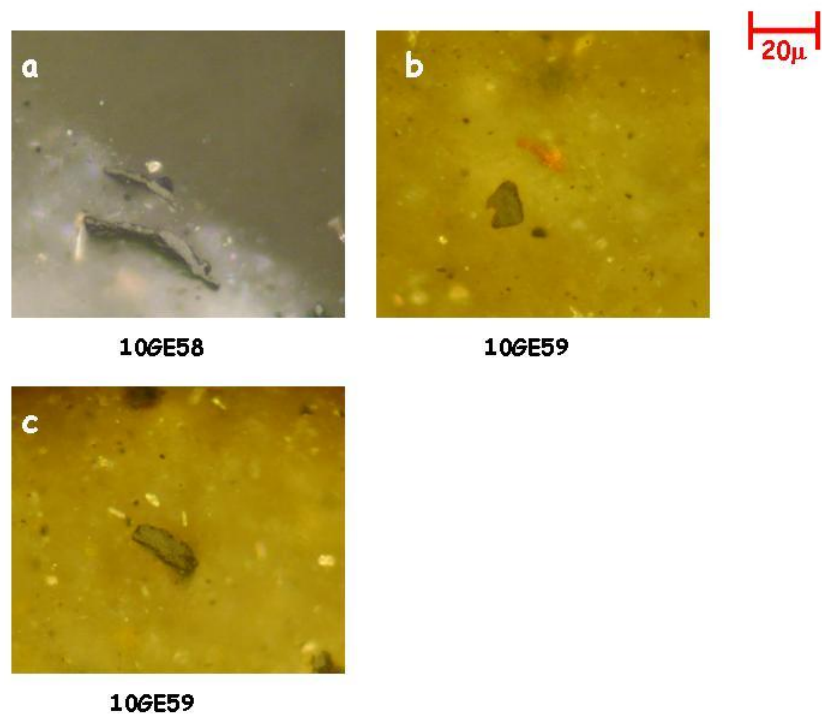


Plate 8

**Vitrinite reflectance plates for samples 10GE53-10GE58.**

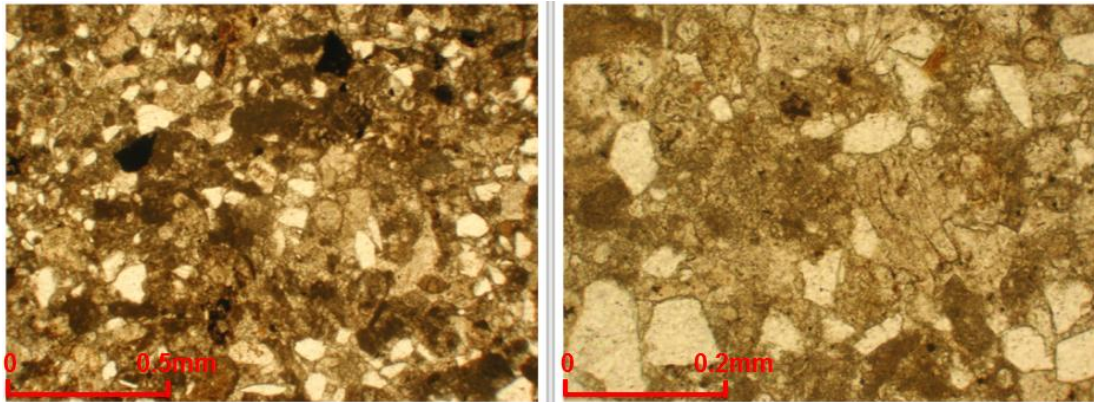


**FIGURE 51**



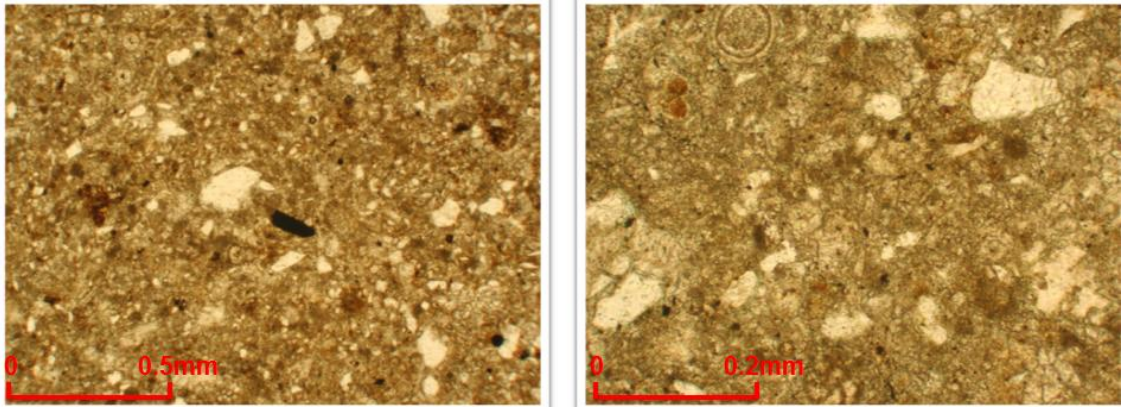
**Vitrinite reflectance plates for samples 10GE58-10GE59.**

**FIGURE 52**



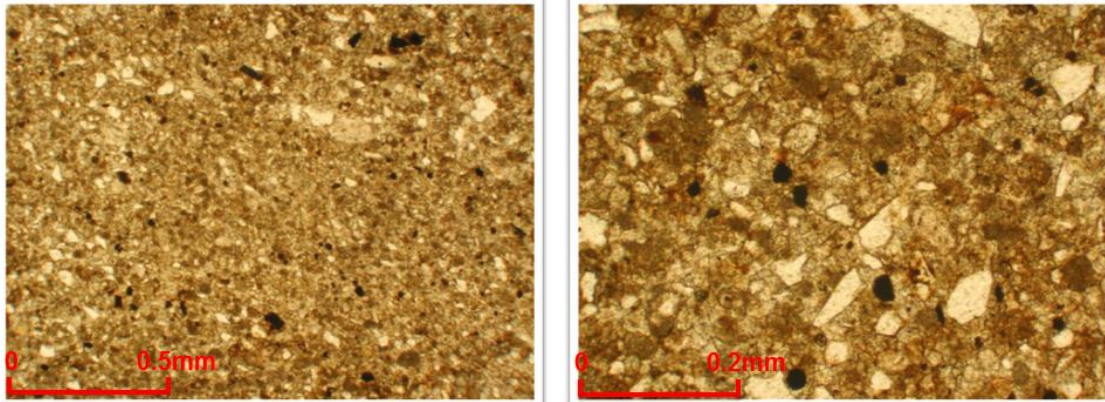
**Thin sections for sample 10RA1 from the Ribera Alta diapir. 40x on the left, 100x on the right, plain light.**

**Figure 53**



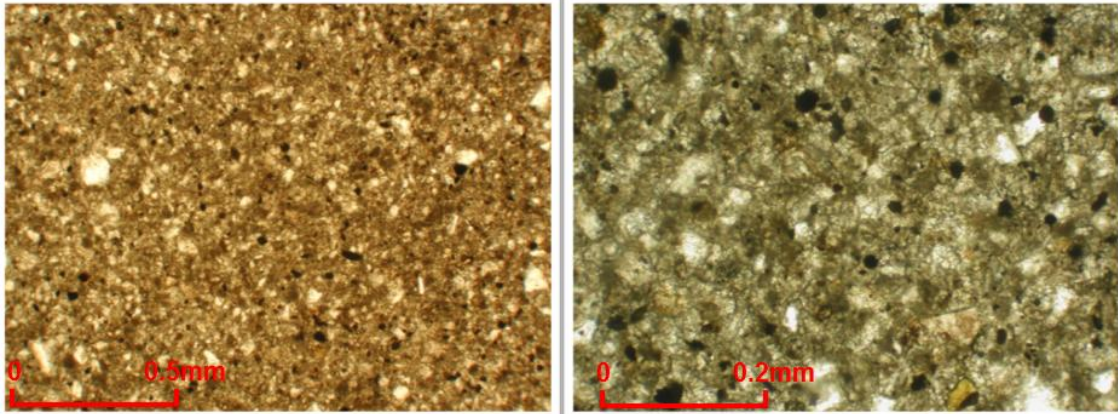
**Thin sections for sample 10RA2 from the Ribera Alta diapir. 40x on the left, 100x on the right, plain light.**

**Figure 54**



**Thin sections for sample 10RA3 from the Ribera Alta diapir. 40x on the left, 100x on the right, plain light.**

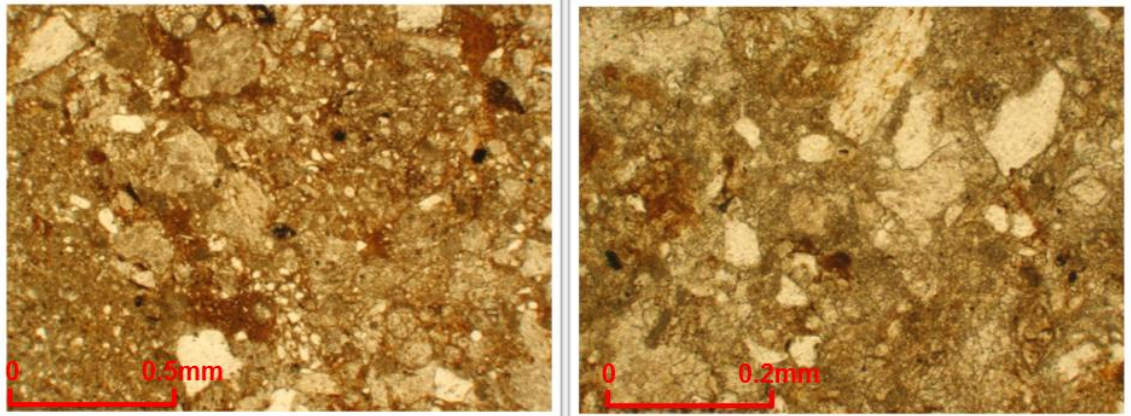
**Figure 55**



**Thin sections for sample 10RA4 from the Ribera Alta diapir. 40x on the left, 100x on the right, plain light.**

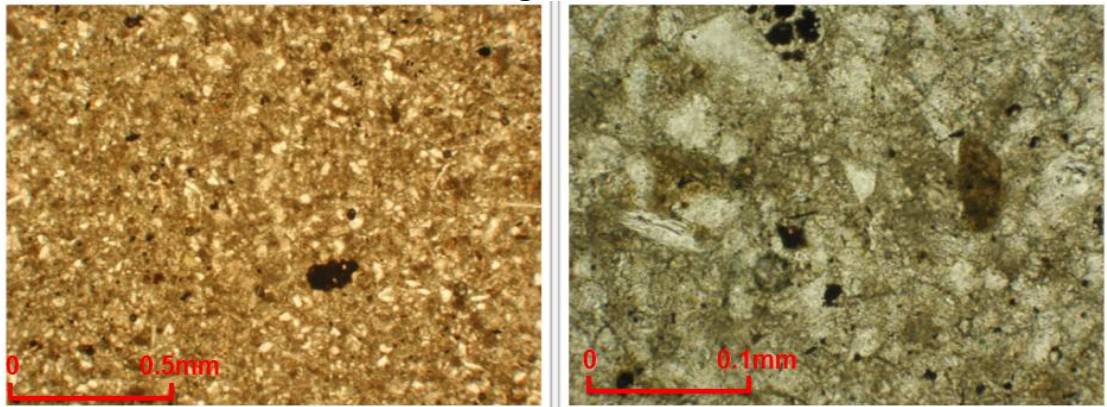


**Figure 56**



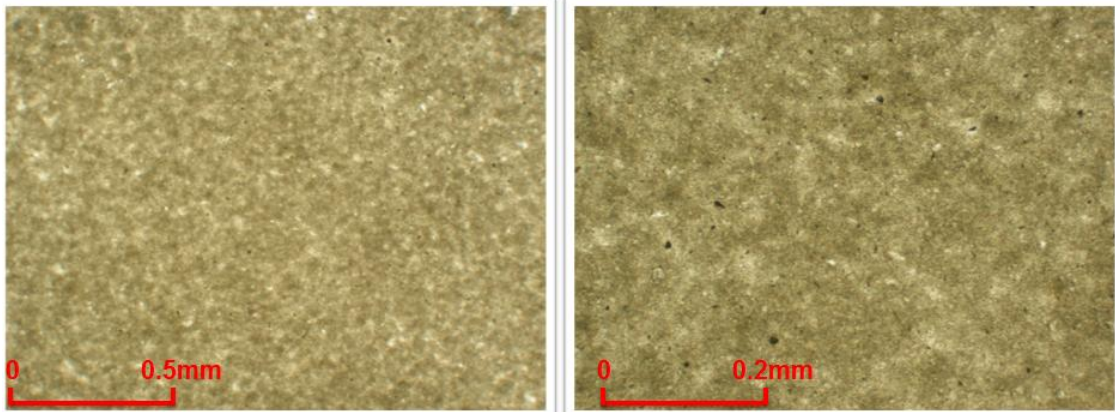
**Thin sections for sample 10RA5 from the Ribera Alta diapir. 40x on the left, 100x on the right, plain light.**

**Figure 57**



**Thin sections for sample 10RA6 from the Ribera Alta diapir. 40x on the left, 200x on the right, plain light.**

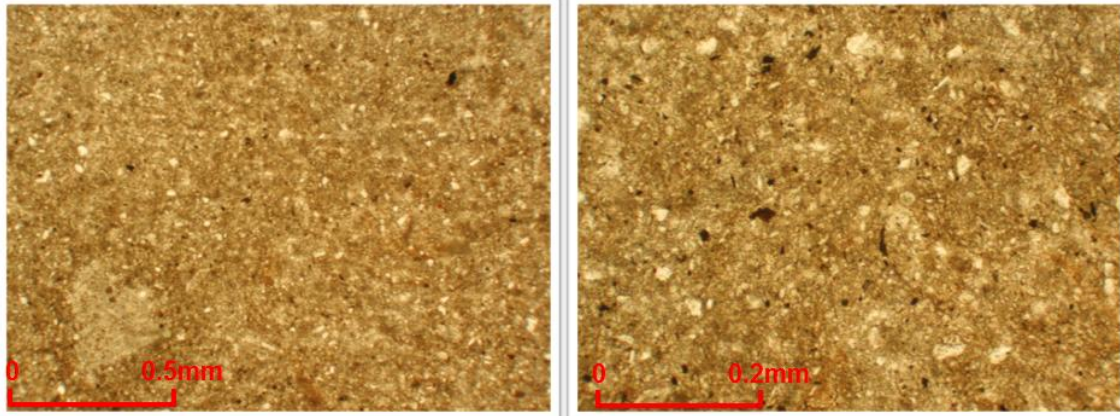
**Figure 58**



**Thin sections for sample 10RA7 from the Ribera Alta diapir. 40x on the left, 100x on the right, plain light.**

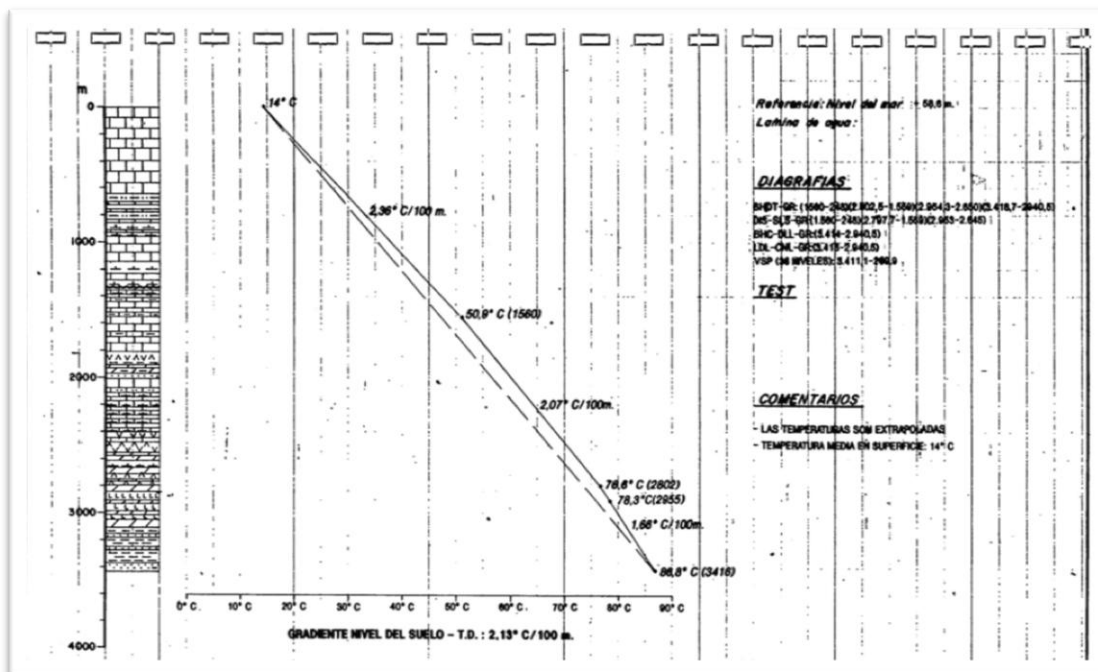


**Figure 59**



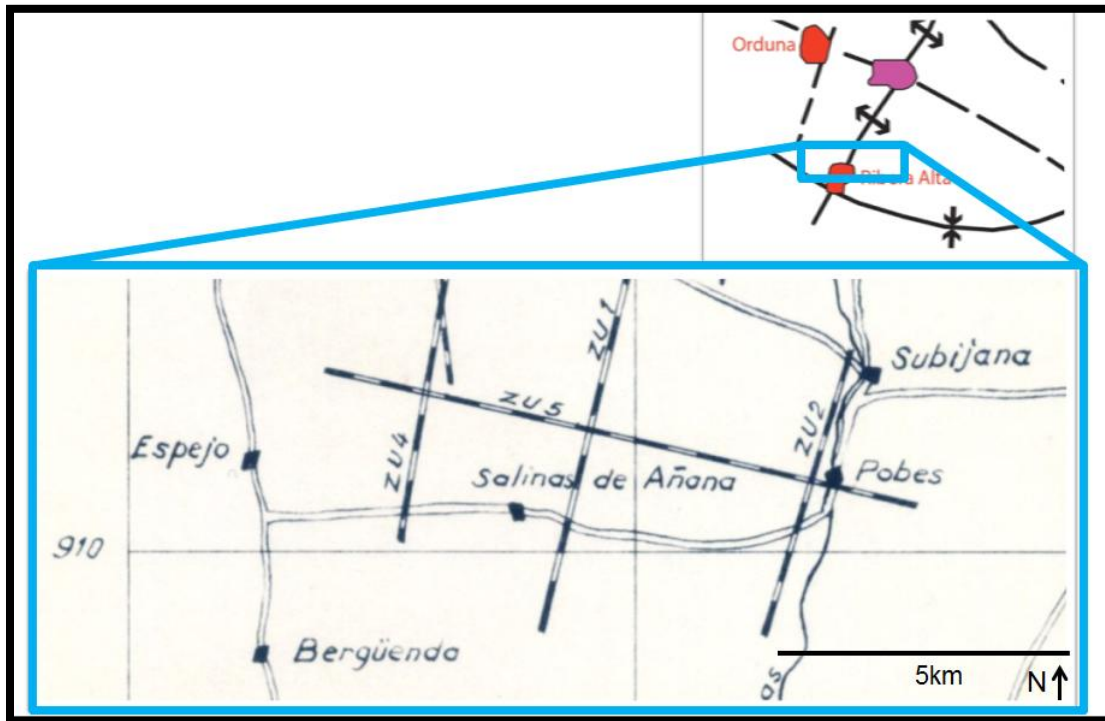
**Thin sections for sample 10RA8 from the Ribera Alta diapir. 40x on the left, 100x on the right, plain light.**

Figure 60



Geothermal gradient, Aulesti-1 well.

Figure 61



Overview of the 1\_71T seismic block, near the Ribera Alta diapir.

**Figure 62**



**Seismic line ZU1 running north-south onto the northern flank of the Ribera Alta diapir. Vertical axis in time.**

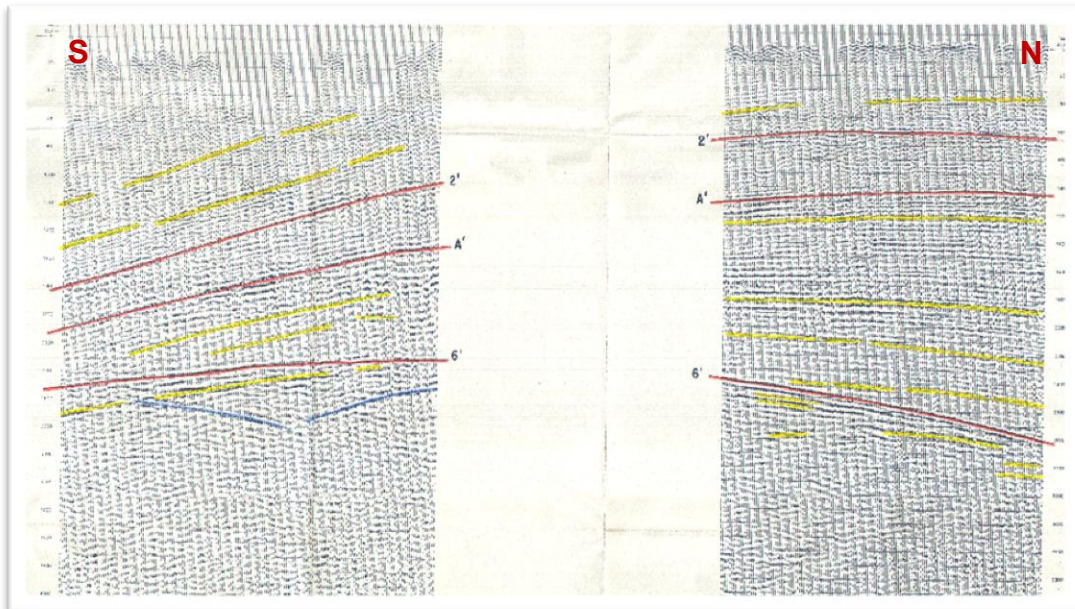
Figure 63



Seismic line ZU2 running north-south, located east of the Ribera Alta diapir. Vertical axis in time.

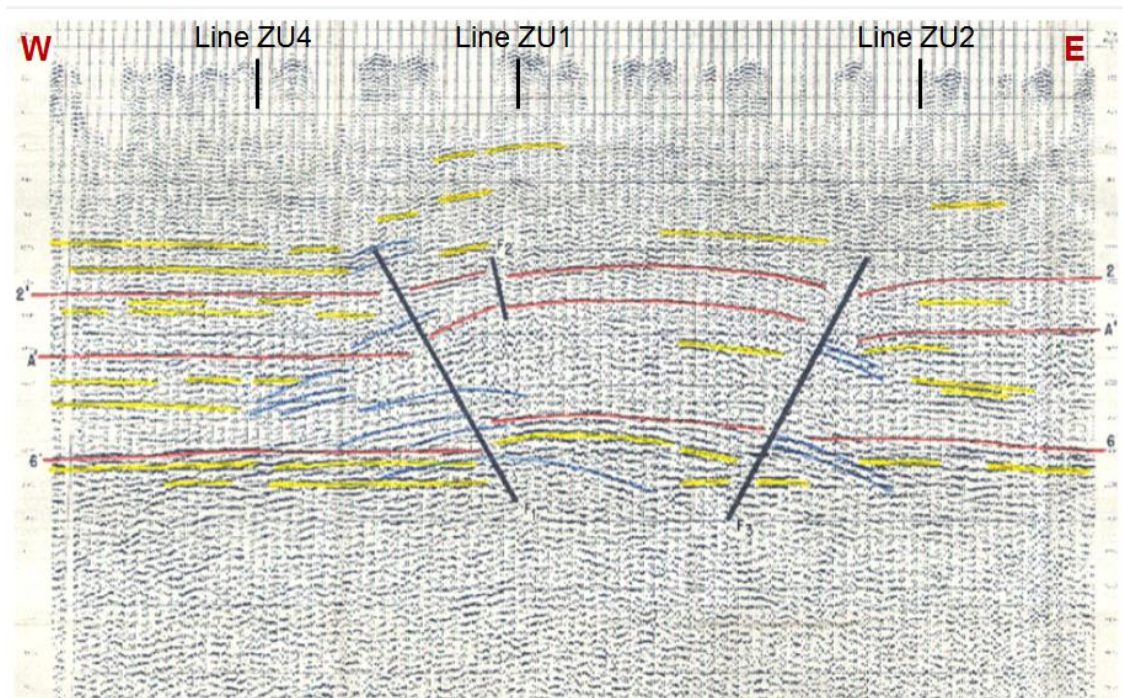


**Figure 64**



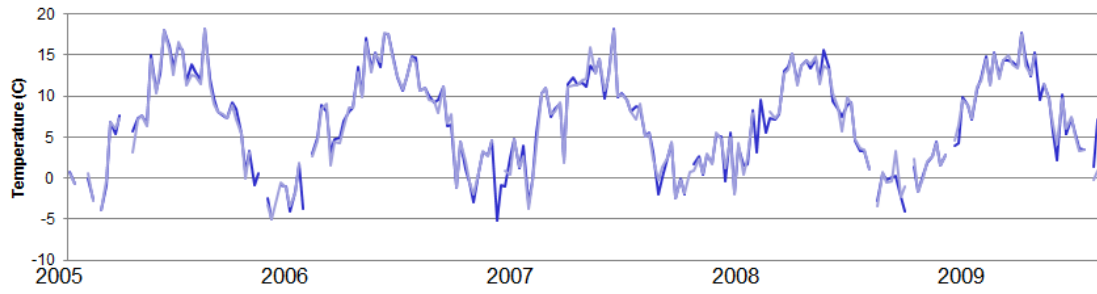
**Seismic line ZU4 running north-south, located west of the Ribera Alta diapir. Vertical axis in time.**

Figure 65

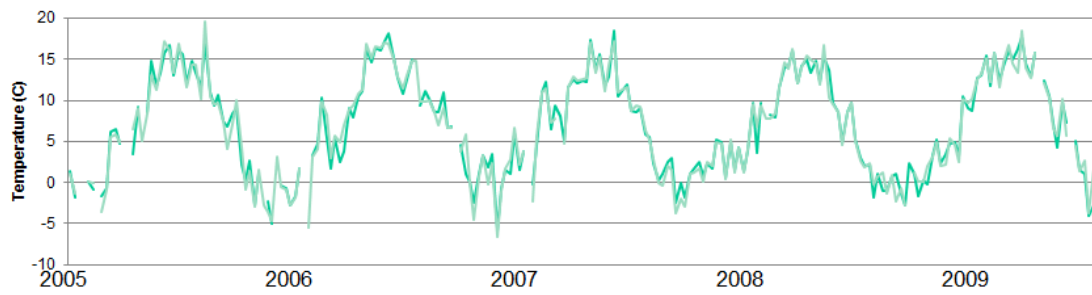


Seismic line ZU5 running east-west along the northern flank of the Ribera Alta diapir. Vertical axis in time.

**Figure 66**  
**Ribera Alta Diapir 1 and Diapir 2 Temps**



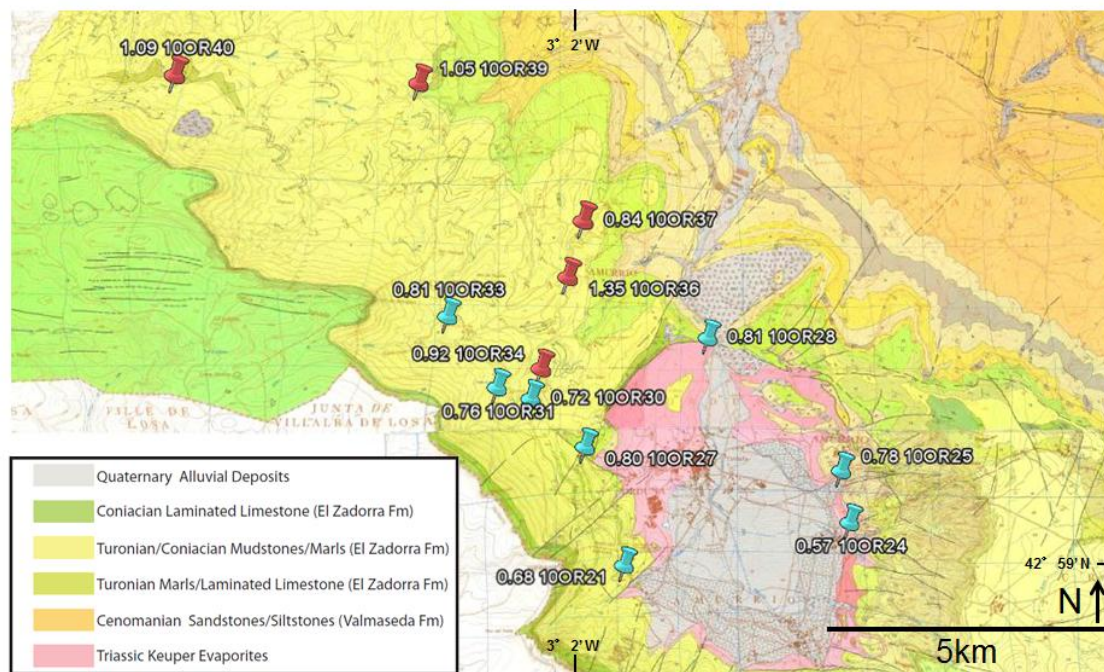
**Ribera Alta Nondiapir 1 and Nondiapir 2 Temps**



**Ribera Alta diapir and nondiapir remote sensing temperatures over 5 years.**

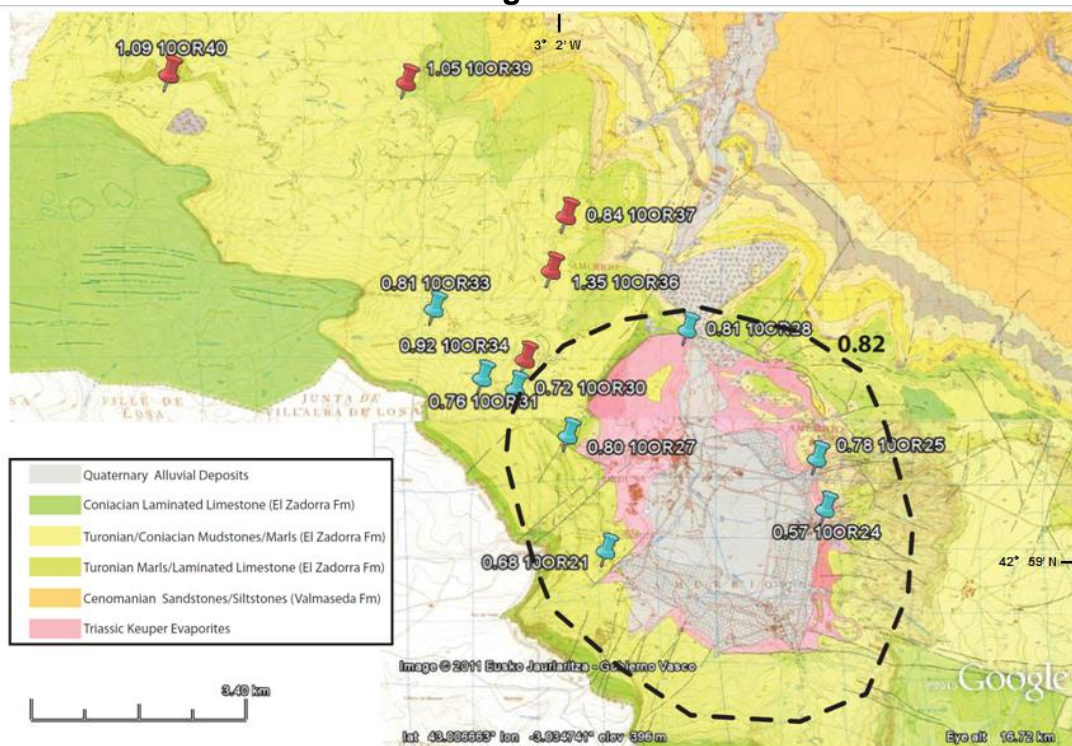


Figure 67



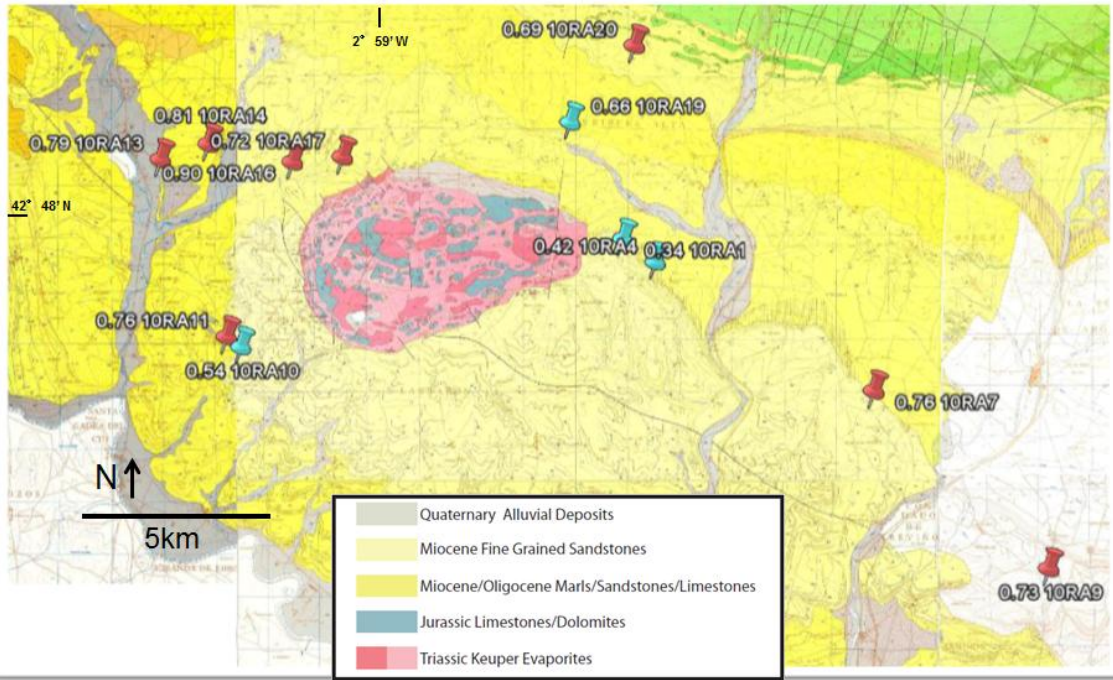
Vitrinite reflectance data for the Orduna diapir. Avg value = 0.82. (Ruiz and Jimenez, 1991).

Figure 68



Vitrinite reflectance data for the Orduna diapir. Avg value = 0.82 (Ruiz and Jimenez, 1991).

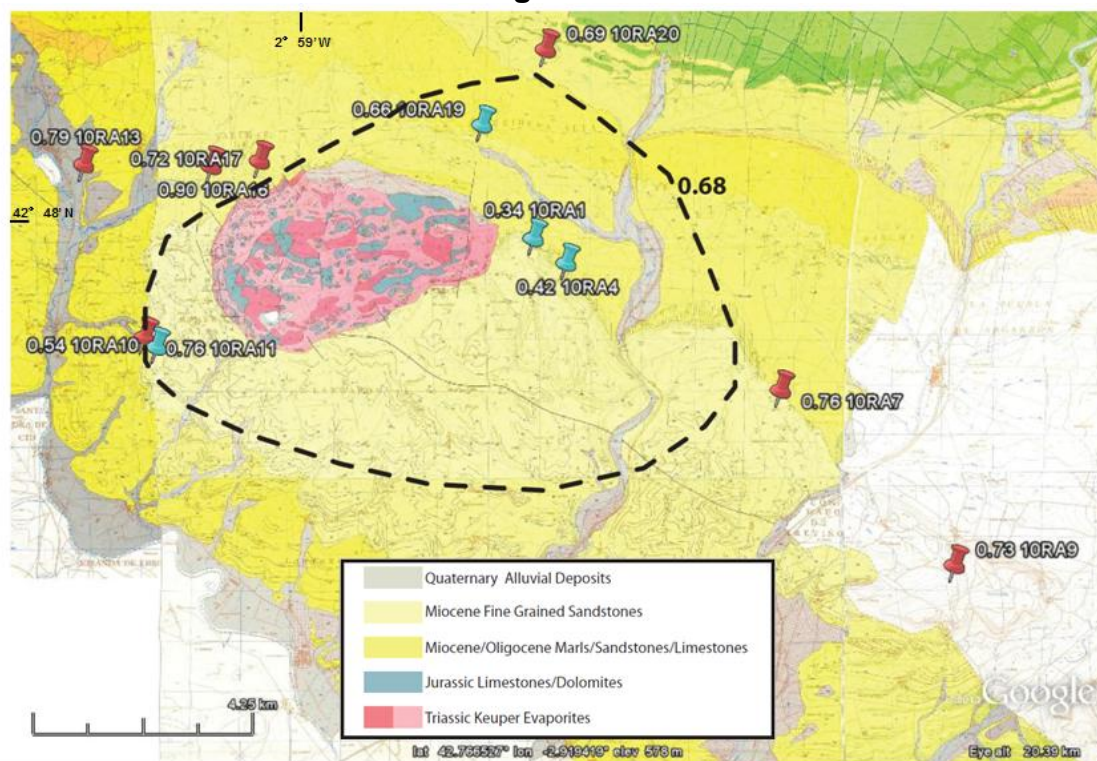
Figure 69



Vitrinite reflectance data for the Ribera Alta diapir. Avg value = 0.68. (Ruiz and Jimenez, 1991).

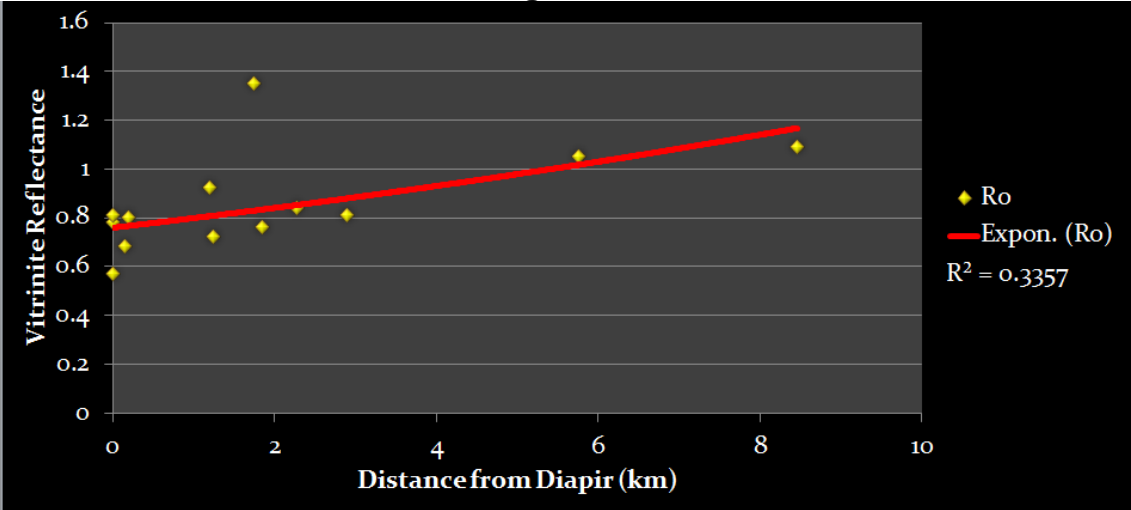


Figure 70



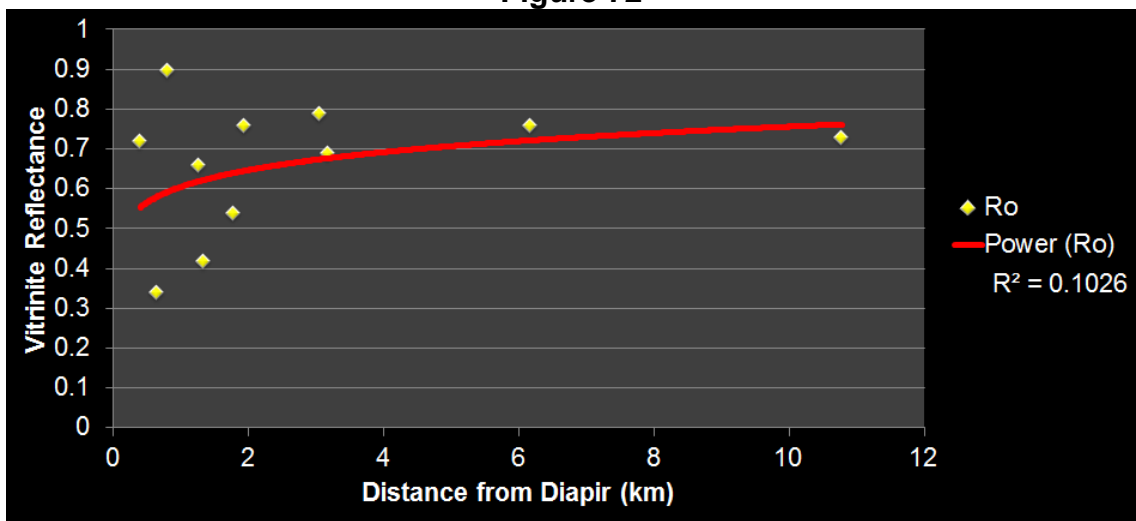
Vitrinite reflectance data for the Ribera Alta diapir. Avg value = 0.68

Figure 71



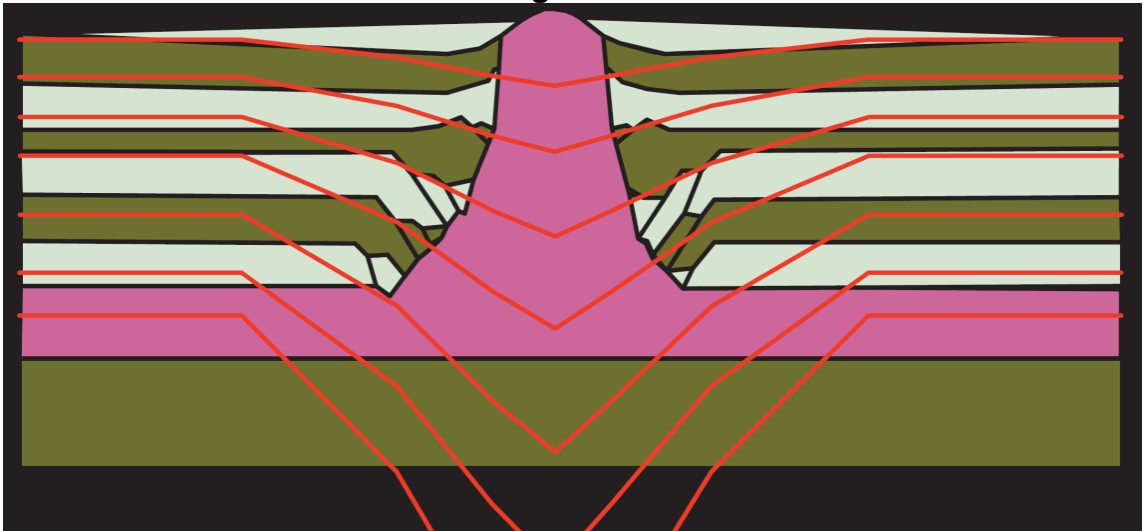
Vitrinite reflectance vs. distance for the Orduna diapir.

Figure 72



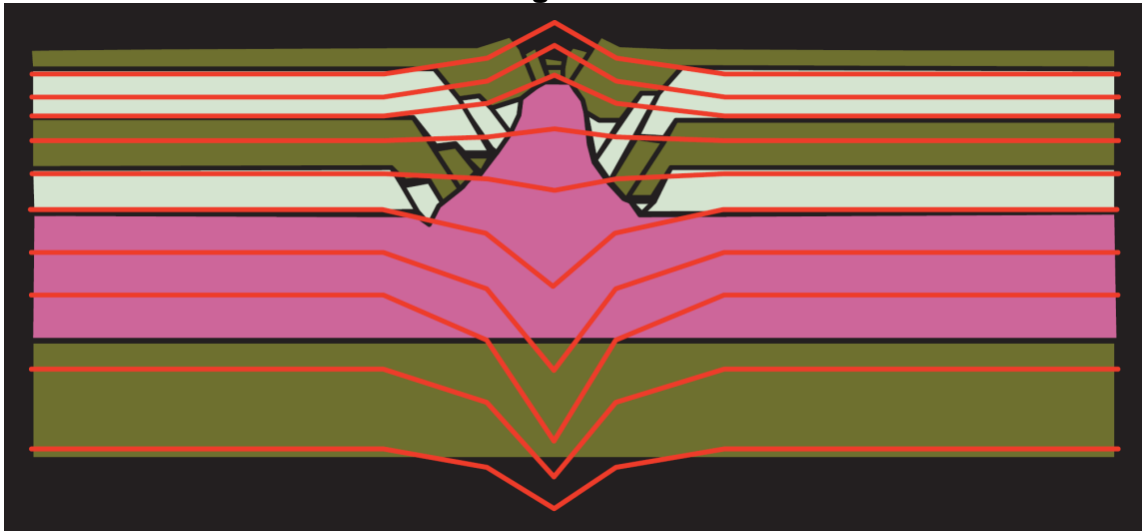
Vitrinite reflectance vs. distance for the Ribera Alta diapir.

**Figure 73**



**A diapir that breaches the surface has a monopolar temperature anomaly, with all heat lost to the atmosphere (derived from Mello et al. (1995)).**

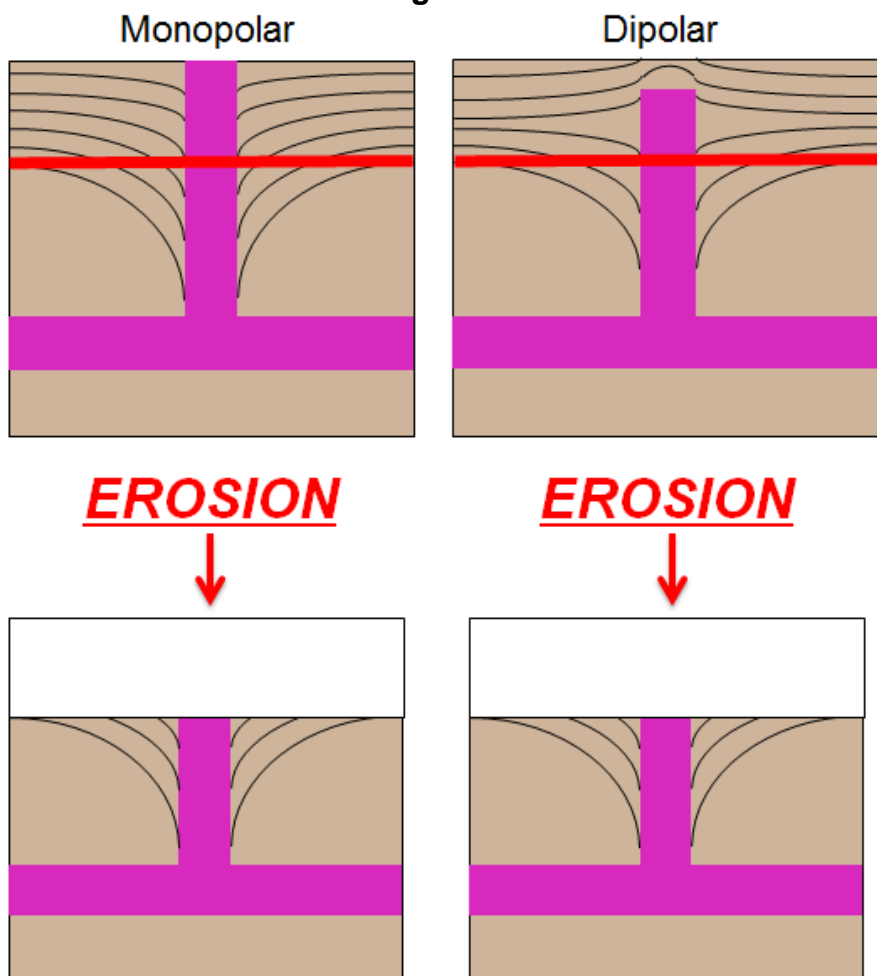
**Figure 74**



**A diapir with overburden has a dipolar anomaly (derived from Mello et al. (1995)).**

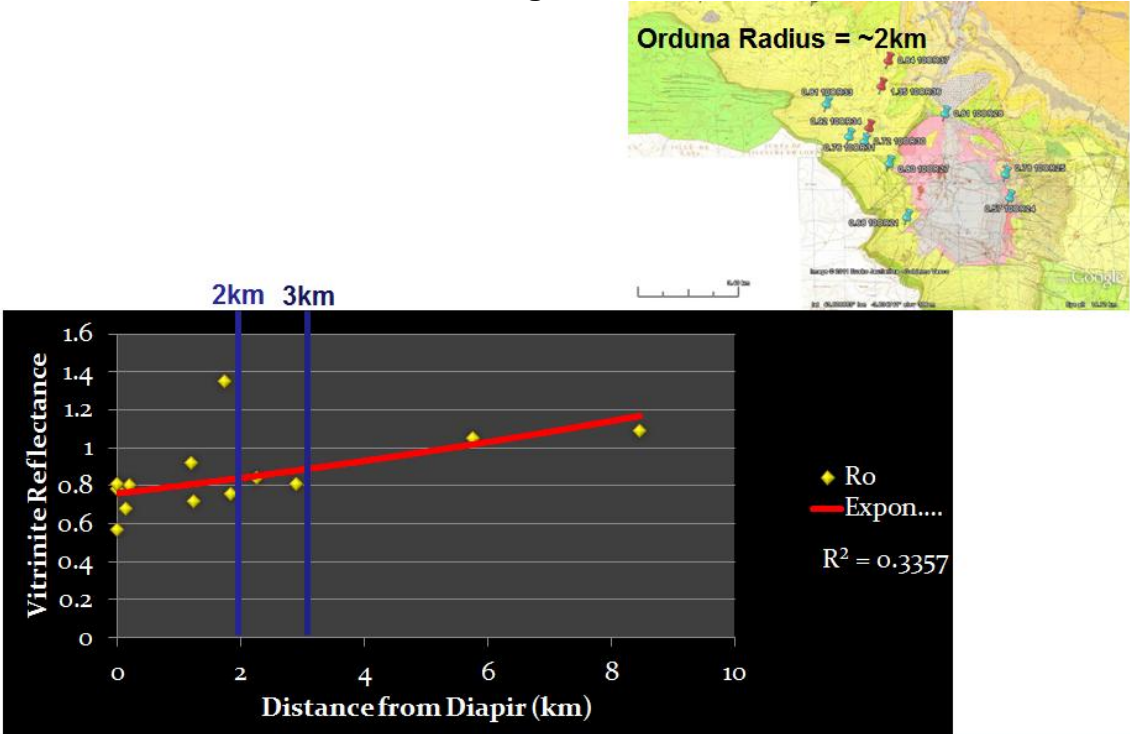


Figure 75



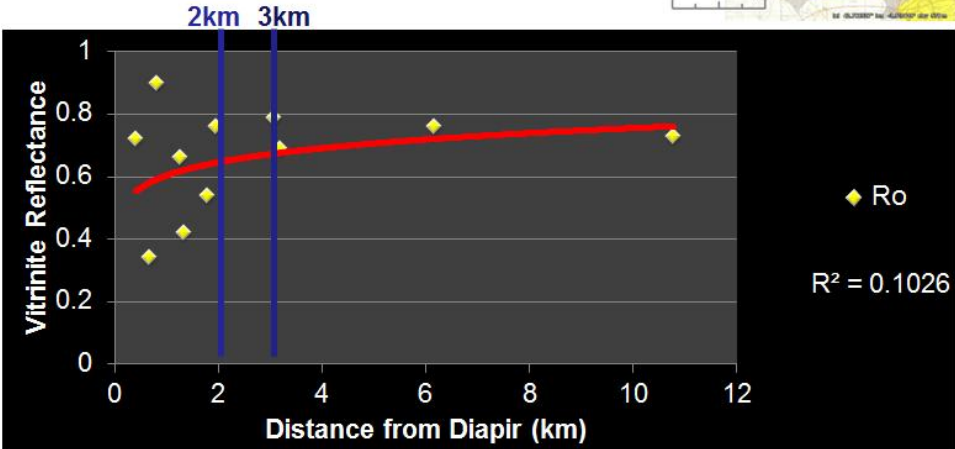
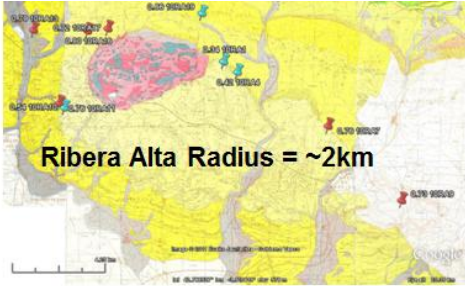
With sufficient erosion, an exposed (monopolar) and buried (dipolar) diapir will have similar remnant thermal expressions.

Figure 76



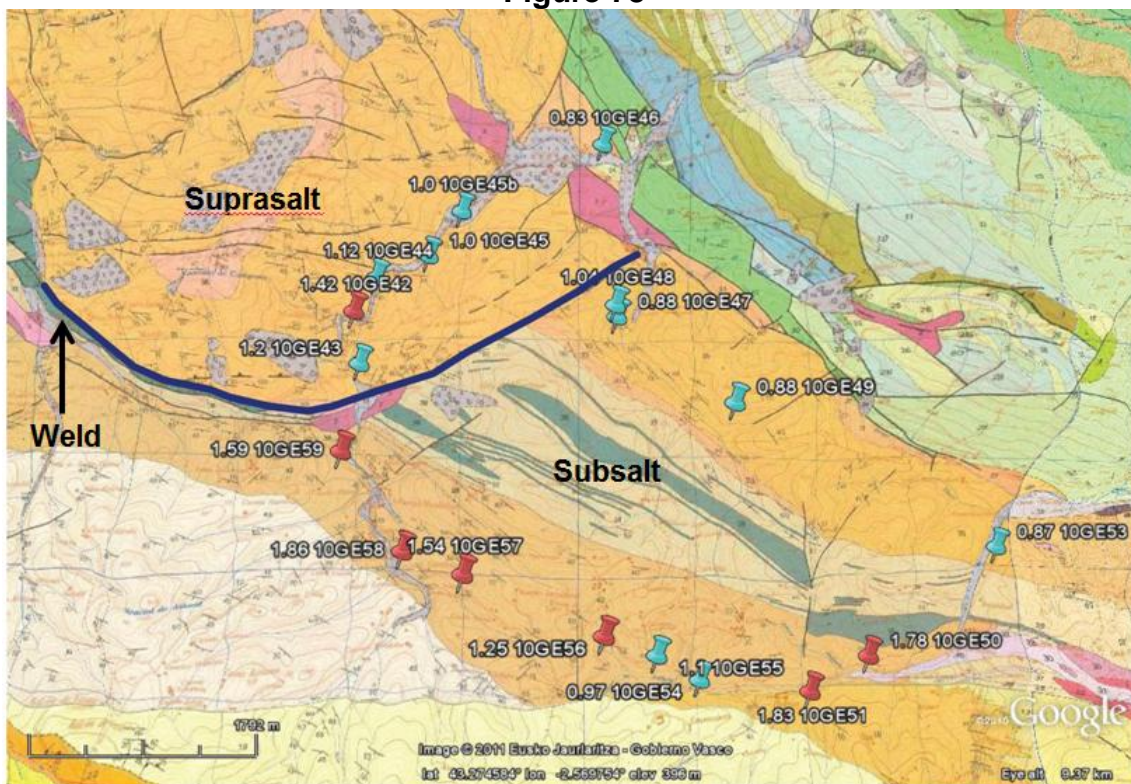
The thermal anomaly around the Orduna diapir appears to be confined to within 1.5x the 2km radius.

Figure 77



The thermal anomaly around the Ribera Alta diapir appears to be confined to within 1.5x the 2km radius.

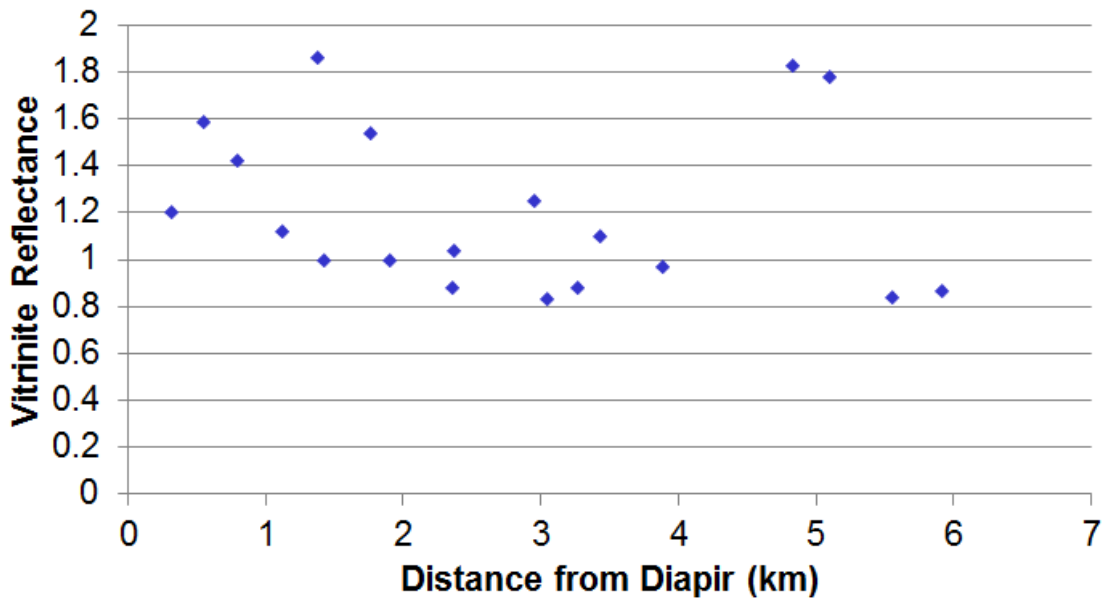
Figure 78



Vitrinite reflectance data for Gernika salt weld. Avg value = 1.21

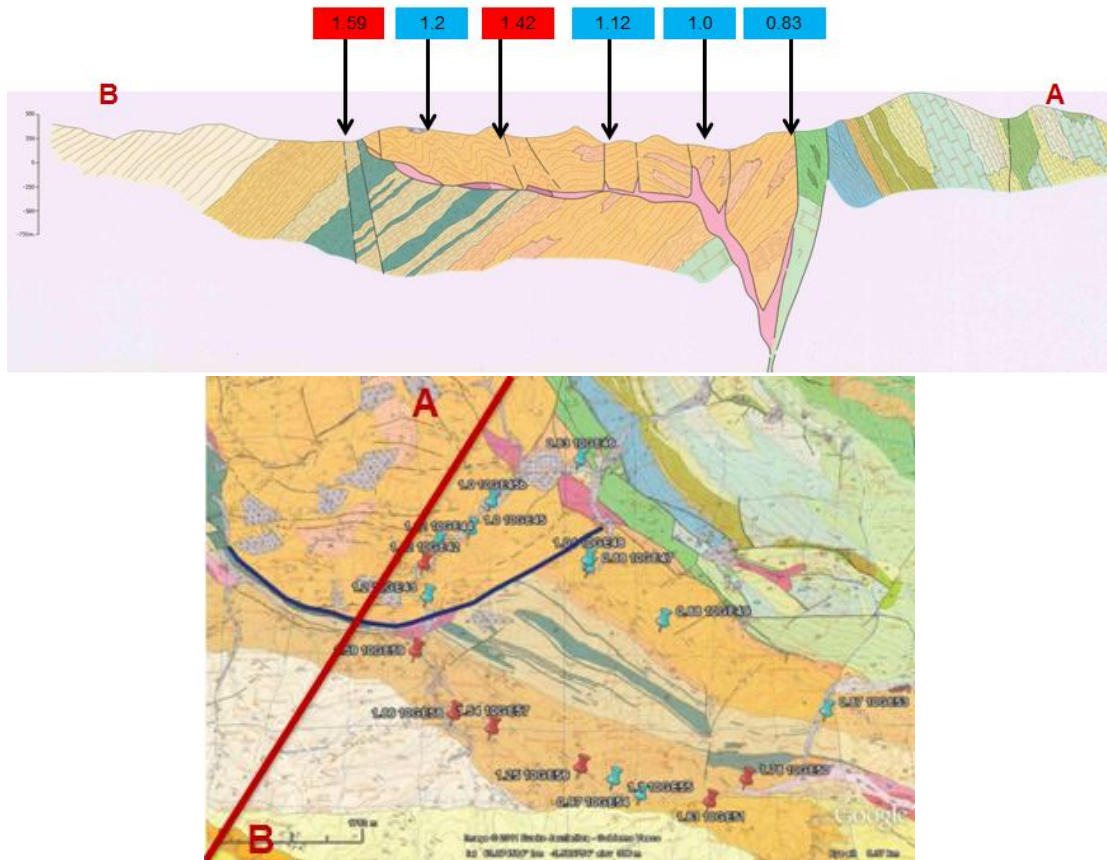
Figure 79

Gernika Ro vs. Distance from Weld Outcrop 1



Vitrinite reflectance vs. distance for the Gernika weld outcrop 1.

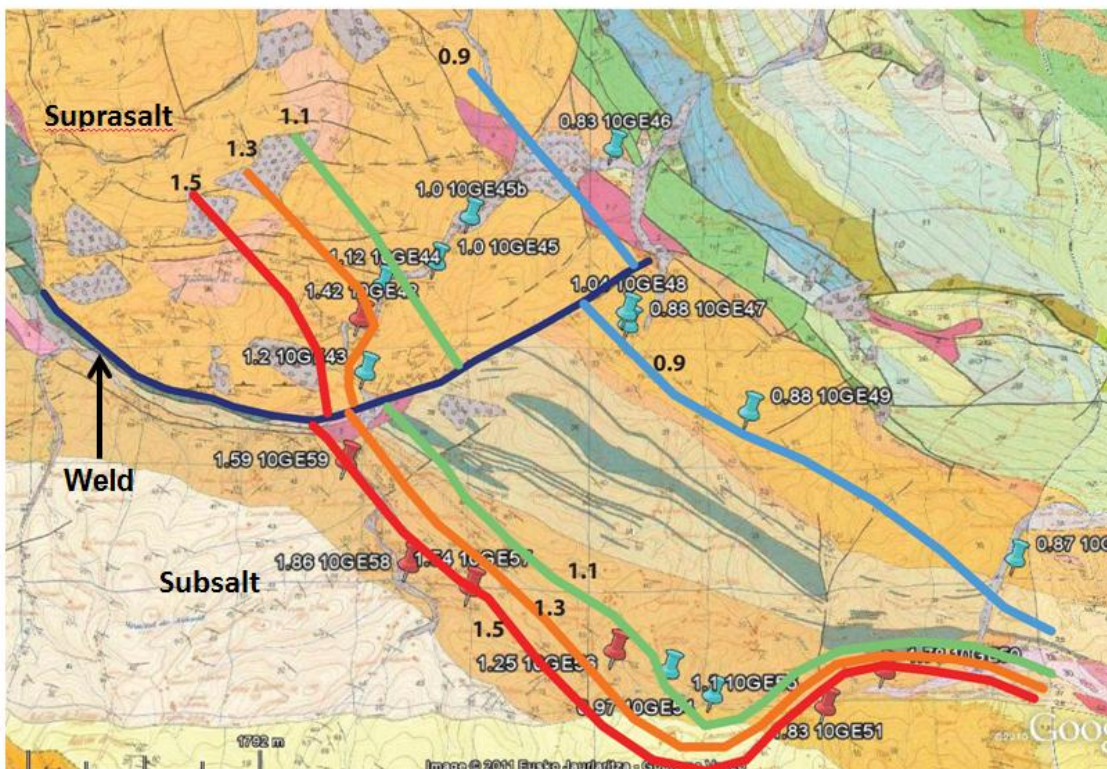
**Figure 80**



**Geological cross section of the Gernika salt weld with vitrinite reflectance values (Ruiz and Jimenez, 1991).**

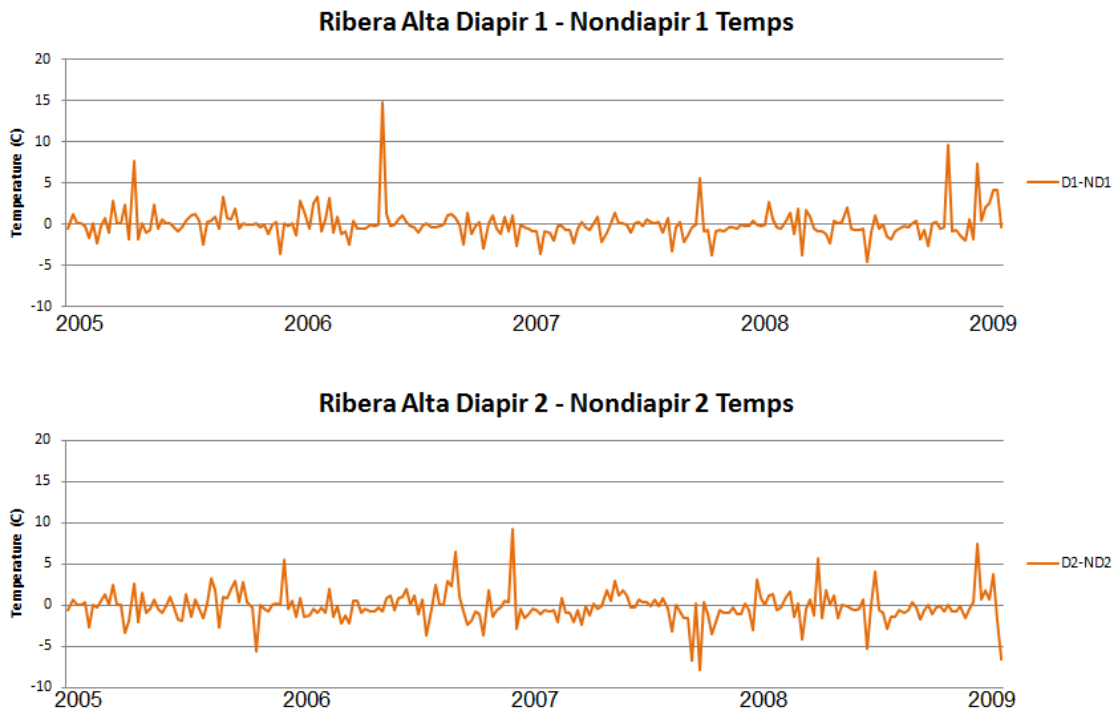


Figure 81



Suprasalt and subsalt maturity contours are offset, showing suprasalt samples to be more mature.

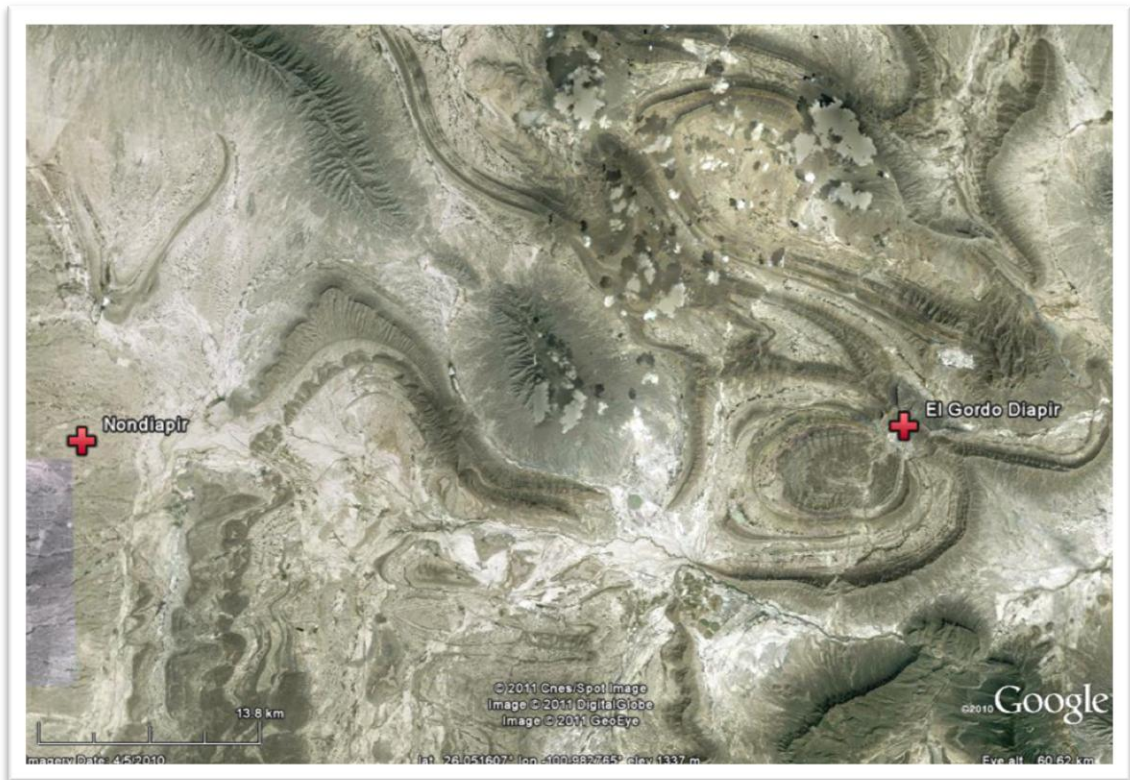
**Figure 82**



**Differences between diapir and nondiapir remote sensing temperatures for the Ribera Alta diapir.**



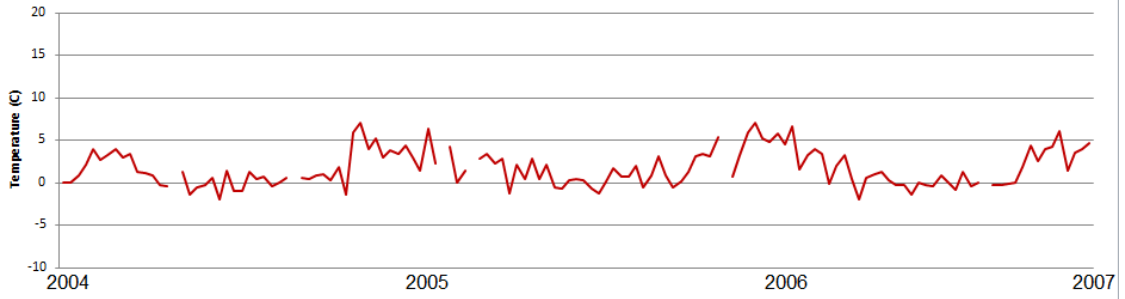
**Figure 83**



**El Gordo diapir and nondiapir remote sensing locations, La Popa basin, Mexico.**

**Figure 84**

**Temperature Difference (Diapir - Nondiapir)**



**Differences between diapir and nondiapir temperatures for El Gordo diapir, La Popa basin, Mexico.**

**Figure 85**

Hypothesis	Location	Conclusion
Maturity Increases as Distance Decreases	Ribera Alta Diapir & Orduna Diapir	<b>REJECTED</b> Maturity Decreased as Distance Decreased
Quartz Cementation Increases as Distance Decreases	Ribera Alta Diapir	<b>INCONCLUSIVE</b> Insufficient Quartz Cement
Dimensions of Thermal Anomalies are Scale Dependent	Ribera Alta Diapir & Orduna Diapir	<b>INCONCLUSIVE</b> Orduna and Ribera Alta Thermal Anomalies Both Extend to ~1.5x Their Radii
Sediments Above an Inclined Weld ( <u>Suprasalt</u> ) are More Mature Than Sediments Below an Inclined Weld (Subsalt)	<u>Gernika Salt WEld</u>	<b>CONFIRMED</b> <u>Suprasalt Sediments are More Mature Than Subsalt</u> <b>AND</b> <u>Maturites Decrease as Distance From the Weld Decreases</u>
Remote Sensing Instruments Can Measure Diapir-Related Thermal Anomalies	Ribera Alta Diapir & El Gordo Diapir (Mexico)	<b>CONFIRMED*</b> *In Areas of Low Vegetation

**Summary of hypotheses and conclusions.**